Dissertation ETH Zurich No. 22489

Idealized studies of summertime moist convection over topography

A dissertation submitted to attain the degree of
DOCTOR OF SCIENCES of ETH ZURICH

(Dr. Sc. ETH Zurich)

presented by

Hanieh Hassanzadeh

M.Sc., Sharif University of Technology, Tehran
born on 27.07.1982
citizen of Iran

accepted on the recommendation of

Prof. Dr. Christoph Schär, examiner
Dr. Jürg Schmidli, co-examiner
Prof. Dr. Georg Mayr, co-examiner

2015

Abstract

The climatology of mid-latitude mountainous regions is often characterized by orographic precipitation, which typically provides ample water resources but also makes the respective regions susceptible to hazards such as thunderstorms and floods. In particular in the warm seasons, deep convection may cause severe and sudden flash flood events. To reduce the potential damages, accurate forecasting of these events is vital. However, due to the multi-scale nature of the underlying dynamics, and due the significant number of physical processes involved, many aspects of mountain precipitation remain poorly understood. Particularly in the summer season, when weakly stratified atmospheric conditions prevail, there is an intricate coupling between the atmospheric dynamics, moist convection, as well as land surface, boundary layer and microphysical processes. The resulting flows involve a strong diurnal cycle of high complexity. In the recent decade, kilometer-scale convection-resolving models (CRMs) are increasingly used as new tools in atmospheric and climate sciences. They allow representing atmospheric convection explicitly, rather than using parameterization schemes as in large-scale models. This thesis uses the COSMO model in a CRM set-up. It aims at an improved understanding of mid-latitude summertime moist convection and precipitation mechanisms over and in the vicinity of isolated mountains. To this end, an idealized framework is used, which has been developed and tested in a previous study to investigate diurnal convection in absence of topography.

In chapter 2, we focus on the diurnal cycle of summertime precipitation over and in the vicinity of a Gaussian-shaped mountain with a height of 1000 m and half-width of 20 km. The simulations are forced by diurnal radiation and are conducted over an extended time period to ensure that the diurnal equilibrium is reached, where deep convection is triggered every day, but with considerable day-to-day variations. Significant spatial and temporal variability in precipitation is found over the 20 day long analysis period. The variations result from different physical mechanisms associated with the triggering of deep convection in different parts of the domain. Over the mountain lee, mass convergence from thermal upslope flow and the background wind triggers intensive precipitation in the morning. A second triggering mechanism is observed along the leading edge of the primary cold-pool, downstream of the mountain. This cold pool spreads over the near vicinity and leaves a dry area behind that gets very little precipitation. In the afternoon, some precipitation is seen over the flat part of the domain owing to the deep convection resulting from the boundary layer growth. In the evening, the collisions of outflows from previous precipitation events also cause deep convection and precipitation. We investigate the impact of the mountain height on the characteristic precipitation timing and the associated spatial patterns. It is found that for higher mountain, the precipitation onset is earlier and the hourly precipitation frequency is higher. The intensity increases with mountain height as long as the flow-over regime is dominant, and it decreases with the onset of the flow-around regime.

After understanding the main precipitation mechanisms involved, we investigate the influence of the mountain on producing extreme precipitation events in different environmental conditions. In chapter 3 we consider the role of different soil moisture conditions and different atmospheric stratifications. Extreme events are defined in terms of precipitation percentiles. Among the simulations with different soil moisture, drier cases lead to higher sensible heating, stronger diurnal mountain circulations and ultimately to stronger lee precipitation. In essence, dry soils emphasize the impact of the diurnal mountain circulations. For the cases with different atmospheric stratification, two opposing effects are seen. For weakly stratified cases, the boundary layer becomes drier, leading to more efficient evaporation of falling precipitation, and thereby to stronger cold-pools. Hence, extreme precipitation events associated with cold-pool formation are enhanced. On the other hand, strongly stratified conditions lead to moister and warmer atmospheric boundary layers, thereby enhancing precipitation due to the other triggering mechanisms, e.g. lee convergence and boundary layer growth.

To summarize, the modeling framework used here provides insight into the influence of mountains on the summertime precipitation. The focus on idealized simulations helps to identify and interpret the different precipitation mechanisms, and their sensitivities with respect to the mountain geometry and to environmental conditions.

Zusammenfassung

Das Klima in den Berggebieten der mittleren Breiten ist weitgehend durch orographischen Niederschlag geprägt, der diese Regionen mit wichtigen Wasserressourcen versorgt, aber auch das Risiko für schwere Gewitter und Überschwemmungen erhöht. Besonders in der warmen Jahreszeit können starke Konvektionsereignisse zu massiven, flutartigen Überschwemmungen führen. Um die potentiellen Schaden solcher Ereignisse zu begrenzen, sind exakte Vorhersagen notwendig. Allerdings sind viele Aspekte, die zu Niederschlag in Berggebieten führen nur schlecht verstanden, was vor allem an der Vielzahl der involvierten physikalischen Prozesse und der skalenübergreifenden Dynamik liegt. Besonders im Sommer wenn die atmosphärische Schichtung relativ instabil ist, sind die Wechselwirkungen zwischen atmosphärischer Dynamik, feuchter Konvektion, Landoberfläche, Grenzschicht und den mikrophysikalischen Prozessen sehr kompliziert. Die resultierende atmosphärische Strömung zeigt einen starken und sehr komplexen Tagesgang. Im letzten Jahrzehnt wurden verstärkt neue konvektionsauflösende Modelle in den Atmosphären- und Klimawissenschaften eingesetzt. Diese Modelle erlauben es Konvektion in der Atmosphäre explizit zu simulieren, anstatt sie durch Parametrisierungen approximieren. In dieser Dissertation wird das COSMO Modell in einer solchen konvektionsauflösenden Konfiguration angewandt. Ziel der Arbeit ist es, das Verständnis über feuchte Sommerkonvektion in den mittleren Breiten und die damit verbundene Niederschlagsprozesseüber in der Nähe von freistehenden Bergen zu verbessern. Zu diesem Zweck, führen wir idealisierte Simulationen von Tagesgang der Konvektion durch.

Im zweiten Kapitel dieser Arbeit fokussieren wir uns auf den Tagesgang von Sommerniederschlag in der Umgebung eines einzelnen idealisierten Berges mit einer Höhe von 1000 Metern und einer Breite von 20 Kilometern. Die Simulationen werden mit realen Strahlungsdaten angetrieben und für eine Simulationsdauer von 35 Tagen. Nach einigen Tagen stellt sich ein Gleichgewicht zwischen ein und der tägliche Verlauf ändert sich kaum mehr. Dieses Gleichgewicht zeichnet sich dadurch aus, dass jeden Tag hochreichende Konvektion ausgelöst wird, aber dennoch zufällige Unterschiede von Tag zu Tag ersichtlich sind. Das Niederschlagsfeld zeigt beträchtliche räumliche und zeitliche Variabilität, welche dadurch verursacht wird, dass an unterschiedlichen Orten in der Domäne verschiedene physikalische Prozesse hochreichende Konvektion auslösen. Über der Leeseite des Berges führen thermische Aufwinde und die Hintergrundströmung zu Massenkonvergenz, welche den Niederschlag am Morgen verstärkt. Ein anderes Mechanismus, kann über dem Rand des primären, vom Gewitter induzierten, Kaltluftstroms stromabwärts des Berges beobachtet werden. Ein Kaltluftsee breitet sich in der näheren Umgebung aus und lässt trockene Gebiete zurück, über denen wenig Niederschlag fällt. Am Nachmittag wächst die Grenzschicht und löst über dem flachen Teil des Gebiets hochreichende Konvektion aus, welche wiederum zu etwas Niederschlag führt. Am Abend führt die Kollision von Abwärts Strömungen, ausgelöst durch vorangegangene Niederschlagsereignisse, zu erneuter hochreichender Konvektion mit Niederschlag. Weiter untersuchen wir den Einfluss der Höhe des Berges auf den Zeitpunkt und die damit verbundene räumliche Verteilung des Niederschlags. Es zeigt sich, dass mit zunehmender Höhe des Berges der Niederschlag früher am Tag beginnt und die stündliche Niederschlagsfrequenz höher ist. Die Niederschlagsintensität nimmt mit der Höhe des Berges zu, solange die Strömung über den Berg führt. Wechselt das Regime und die Strömung fliesst um den Berg herum, nimmt der Niederschlag mit der Höhe des Berges ab.

Nachdem wir uns die generellen Mechanismen, welche zu Niederschlag führen, näher ausgeschaut haben, untersuchen wir in Kapitel 3 den Einfluss eines Berges auf extreme Niederschlagereignisse in Abhängigkeit von der Umgebung; ins besondere die Rolle der Bodenfeuchte und der Stabilität der Atmosphäre. Dabei werden Extreme Ereignisse anhand von Perzentilen definiert. In den Simulationen mit unterschiedlicher Bodenfeuchte führen trockene Böden zu einem grösseren sensiblen Wärmefluss, einem stärkeren Tagesgang der Zirkulation und letztendlich zu mehr Niederschlag im Lee des Berges. Im Wesentlichen verstärken trockene Böden die thermischen Zirkulationen. Für die Simulationen mit unterschiedlicher Stabilität der Atmosphäre konnten zwei gegensätzliche Effekte beobachtet werden. Im Falle einer geringen Statifizierung wird die Grenzschicht trockener, was zu einer effizienteren Verdunstung von fallendem Niederschlag und zu stärken Kaltluftseen führt. Extremer Niederschlag, welcher mit diesen Kaltluftseen verbunden ist, wird also verstärkt. Zum anderen führt eine starke Statifizierung zu einer wärmeren und feuchteren Grenzschicht, was wiederum Konvergenz im Lee sowie das Wachstum der Grenzschicht begünstigt und so auch wieder zu verstärktem Niederschlag führt.

Das verwendete Modell und experimentelle Design ermöglichen es den Einfluss von Orographie auf den Sommerniederschlag in Berggebieten zu studieren. Mit Hilfe der idealisierten Simulationen konnten unterschiedliche Mechanismen identifiziert und interpretiert werden sowie ihre Sensitivität in Bezug auf die Geometrie des Berges und der Umweltbedingungen untersucht werden.

Contents

Abstract **i**

Zusammenfassung **iii**

1 Introduction **1**

- 1.1 Atmospheric convection . . . 1
- 1.2 Topographic convection . . . 3
- 1.3 Summer precipitation over Alpine area . . . 4
- 1.4 Numerical modeling . . . 6
- 1.5 Objectives and outlines of the thesis . . . 7

2 Impact of topography on diurnal cycle of summertime moist convection in idealized simulations **11**

- 2.1 Introduction . . . 14
- 2.2 Experimental setup . . . 16
  - 2.2.1 Model description . . . 16
  - 2.2.2 Domain and topography . . . 16
  - 2.2.3 Atmospheric and soil profiles and relaxation method . . . 17
  - 2.2.4 Equilibrium state . . . 18
- 2.3 Results . . . 19
  - 2.3.1 Spatial diversity of precipitation and mean diurnal cycle . . . 19
  - 2.3.2 Mean diurnal flow evolution and day-to-day variabilities . . . 22
  - 2.3.3 Initiation mechanisms for deep convection . . . 24
  - 2.3.4 Generation of the DRY region . . . 26
  - 2.3.5 Sensitivity to topographic height . . . 28
- 2.4 Conclusions . . . 31

3 Impact of topography on summertime extreme precipitation events in different environmental conditions **35**

- 3.1 Introduction . . . 38
- 3.2 Experimental setup . . . 38
  - 3.2.1 Model . . . 38
  - 3.2.2 Domain setup . . . 39

3.2.3 Input profiles and equilibrium state 40
3.3 Results 41
3.3.1 Impact of soil moisture 42
3.3.2 Impact of atmospheric stratification 47
3.4 Conclusion 52

4 Conclusions and outlook **55**
4.1 Conclusions 57
4.2 Outlook 59

A Influence of the size of topography on the diurnal cycle of summertime precipitation over circular mountains **61**
A.1 Precipitation frequency and intensity 63
A.2 Extreme precipitation 66
A.3 Summary 68

B Influence of the wind direction on the evolution of convective storms and intense precipitation over an elliptical mountain **69**
B.1 Mean state 71
B.2 Evolution of the convective cells 73
B.3 Extreme precipitation 76
B.4 Summary 77

References **79**

Acknowledgments **87**

Curriculum Vitae **89**

Chapter 1

Introduction

Moist convection is part of the water cycle and one of the main processes that couples the near-surface heat and water fluxes to the troposphere. Although convection provides fresh water for life on the planet, the extreme events associated with precipitation, e.g. flooding, droughts and landslides, may cause severe damages. Mountainous regions are well known as favorable locations for intense thunderstorms and hailstorms as well as severe flash floods and lightning. Hence, the investigation of deep convection over mountains is essential for understanding the underlying processes of such severe events and thereby to improve forecasting of these events.

In this chapter, first, a brief overview of atmospheric convection is given. We then concentrate more specifically on deep convection over topography. Next, approaches to numerical modelling of convection are summarized. Finally, objectives and outlines of the thesis are presented.

1.1 Atmospheric convection

Dry convection can be described by dry parcel theory (Emanuel, 1994). Dry parcel theory assumes a parcel of dry air that it is neither affected by nor affects the surrounding atmosphere. In other words, the parcel moves adiabatically, meaning that no heat and mass is exchanged with the surrounding air. The behavior of the parcel, when it is displaced vertically, depends on the environmental potential temperature profile ($\theta(z)$) or the potential temperature laps rate ($\partial\theta/\partial z$), where z is the height. If the parcel is moved up from a resting point, its potential temperature (θ_P) will be conserved, while the difference with respect to the environment will change. If at the new level $\theta_P < \theta$, i.e. the parcel is heavier than the surrounding, a negative buoyancy force acts on the parcel. Hence, it will return downward and will oscillate around its original position with Brunt-Väisällä frequency

$$N^2 = (g/\theta)(\partial\theta/\partial z) \tag{1.1}$$

with g as the gravitational acceleration. This atmospheric condition is called stable ($\partial\theta/\partial z > 0$ and $N^2 > 0$). On the other hand, if $\theta_P > \theta$ (parcel is lighter than the surrounding air), the parcel is subjected to a positive buoyancy force and will rise further upward ($\partial\theta/\partial z < 0$ and $N^2 < 0$). This atmospheric condition is called unstable.

In a stable atmosphere, if a parcel contains moisture, it may reach its saturation point. The latent heat release from the further ascent is added to the parcel and warms it up. Some elevations after this level, the latent heat release makes the parcel lighter than the surrounding air and the parcel can maintain its ascent. In other words, in a layer of unsaturated air for which the temperature lapse rate is between moist and dry adiabatic lapse rate, stability depends upon when an ascending parcel gets saturated. This condition is often found in warm seasons over the mid-latitude continents and is called conditional instability (Emanuel, 1994).

If the moist parcel rises to a sufficiently high level, it reaches its lifting condensation level (LCL) and clouds form. The parcel may also reach its level of free convection (LFC), after which, due to the latent heat release (as discussed above), it sustains its buoyant rise to the level of neutral buoyancy (LNB). The potential energy needed to lift the parcel to its LFC is called convective inhibition (CIN) and the available energy between LFC and LNB is referred to as convective available potential energy (CAPE).

Depending on the atmospheric conditions, clouds may cap near the boundary layer top or extend higher. The corresponding convection is called shallow and deep convection, respectively. Deep convection events may occur in different conditions, but they share similar ingredients for the initiation (Doswell et al., 1996). First, lifting due to boundary layer, synoptic or orographic effects is required to overcome CIN and support upward motion of the air parcels. Second, the moisture must be sufficiently high to support cloud formation. Third, the atmospheric stratification (temperature lapse rate) should be such that facilitates the parcel to reach its LFC.

Deep convection then evolves over time. The generated cells may propagate from their origin (Levizzani et al., 2010), split into two or more cells (Wilhelmson and Klemp, 1978; Klemp and Wilhelmson, 1978), or merge with other cells. Most of the time, precipitation events make the deep convection organize into supercells, multicells or squall lines (Rotunno and Klemp, 1985; Rotunno et al., 1988). The precipitation partly evaporates before it reaches the surface and cools the dry subcloud air, which finally spreads as a cold pool over the ground. The dry and cold outflow acts as a gravity current (Cotton et al., 2011) and lifts surrounding warmer and moister air, and triggers new deep convection (e.g. Simpson, 1980). Cold pool development and its influence on cell regeneration is highly dependent on the background wind profile (Rotunno et al., 1988; Parker, 1996; Lin et al., 1998; Lin and Joyce, 2001). More specifically, the wind shear and direction are important factors in determining cold-pool evolution (Amber et al., 2014; Soderholm et al., 2014).

1.2 Topographic convection

Mountains act as barriers for impinging air and change the flow regime (Smith, 1979; Schär, 2001). The flow-regime effect may be seen in the form of mountain upstream stagnation, downstream separation (Schär and Durran, 1997; Bauer et al., 2000) and/or mountain waves (Durran, 1990). For dry flow over an elliptical mountain, the flow regime (flow around vs. flow over) depends on the mountain non-dimensional height, $\hat{h} = HN/U$ (H is the mountain height and U is the wind speed crossing the mountain) and the mountain profile (the ratio of the along-flow to cross-flow width). Dry flow-mountain interaction has been investigated comprehensively from many aspects (e.g. Bauer et al., 2000; Crook and Tucker, 2005). The background flow regime defines the timing and location of the convection triggering (Mass, 1981; Chien and Mass, 1997). For moist air, the atmospheric instability may change from stable to conditionally unstable if condensation occurs. In this situation, $\hat{h}$ should not be calculated by N as described above. Instead it is calculated by the moist Brunt-Väisällä frequency

$$N_m{}^2 = g\frac{1 + (Lq_s/RT)}{1 + (\varepsilon L^2 q_s/c_p RT^2)}\Big(\frac{\partial ln\theta}{\partial z} + L/c_p T\frac{\partial q_s}{\partial z}\Big) - g\frac{\partial q_w}{\partial z} \qquad (1.2)$$

where L is the latent heat vaporization, T the absolute temperature, q_s the saturation mixing ratio, q_w the total water mixing ratio, R the dry air gas constant, ε the rate between R and the gas constant for moist air and c_p the heat capacity of dry air (Durran and Klemp, 1982; Miglietta and Buzzi, 2001). Owing to this non-linear behavior, the interaction of the moist flow and topography become complicated and have not yet been fully investigated. The flow regime may change throughout the day, particularly in the warm season when the radiative forcing has a strong diurnal cycle. Net radiative energy derives the surface energy budget. Surface energy fluxes modify the boundary layer temperature and moisture profiles and affect the location and the timing of convection triggering. Another pattern seen in the warm season is thermal (upslope) flows (Banta, 1986). This mechanism may change the temperature and moisture profiles and provide a lifting force.

Ultimately, as the moist air is lifted to the LCL, clouds form. Houze (2012) summarizes the mechanisms by which mountains and hills influence clouds. In fair-weather conditions in the warm season, mountainous regions are favourable areas for deep convection (e.g. over the Alps, Levizzani et al. (2010) and over the Rockies, Carbone and Tuttle (2008)). During the warm season, the mountains play the role of a heat source and generate strong thermally-driven winds along the sunlit slopes. This is mostly due to the differential heating between slope surface and adjacent air, causing plain-mountain circulations and upslope flows (Egger, 1990; Vergeiner and Dreiseitl, 1987). The low-level convergence generated from slope circulations and background flow is one of the preferential mechanisms in triggering summertime convection over topography (Barthlott et al., 2011).

To understand the underlying processes in convection over topography, idealized simulations play a key role. Some mountain-flow interactions are explained by 2D-ridge simulations by Miglietta and Rotunno (2005, 2006, 2009, 2010, 2014). They performed simulations with different flow regimes and concluded that the simulations with the same $\hat{h}$, but different wind speed and mountain height may lead to different (precipitation) regimes. In addition, the location of the heavy precipitation may also depend on the LCL, the slope of the mountain and the time that convective cells travel to reach the mountain peak. Their studies show that the cold-pool propagation plays an important role in the evolution of the convective cells. They also investigated the cold-pool movement in the mountain vicinity with respect to the wind profile. Some idealized studies with 3D settings investigate the soil-moisture-precipitation feedback (e.g. Hohenegger et al., 2009), where simulations with various initial soil moisture values are compared. Some sensitivity studies are also done on the impact of the wind shear on the triggering and evolution of convective organizations (e.g. over land, Amber et al., 2014).

Apart from numerical studies, the convection over topography has also been investigated in several international field campaigns. A part of the Mesoscale Alpine Programme (MAP; Bougeault et al., 2003) focused on improving the prediction of moist processes over and in the vicinity of complex topography, including interactions with dynamical and land-surface processes, using data over the Alpine domain. This campaign improved our understanding of orographically influenced precipitation events and related flooding episodes, involving deep convection, frontal precipitation and runoff. The International H2O Program (IHOP; Weckwerth and Parsons, 2006), carried out over the U.S. southern Great Plains, led to an improved characterization of the 4D distribution of moisture. This was applied to enhance the understanding and prediction of convection initiation. During the summer of 2005, the Convective Storm Initiation Project (CSIP; Browning et al., 2007) took place over the southern UK. The project aimed at a better perception and prediction of convection initiation for heavy precipitation events. The Convective and Orographically-induced Precipitation Study, (COPS; Wulfmeyer et al., 2011) was the most recent campaign in this area and took place over the Black Forest and the Vosges mountains in southern Germany and eastern France in summer 2007. Its aim was to better understand convection initiation processes over low-mountain areas. All projects aimed at improving the observational and numerical representation of precipitation, covering different mountain regions and atmospheric conditions, and helped to produce a more general understanding of convection initiation and development processes.

1.3 Summer precipitation over Alpine area

The Alps cover a large part of Central Europe and play a substantial role in defining the weather over this regions. The Alps regulate the flow streams and moisture transportation. Over the central Europe, precipitation pattern in general and the summertime precipitation in particular are highly tied to the Alpine slope and elevation. Fig. 1.1 illustrates 20-year daily mean precipitation climatology for the four seasons (Frei and Schär, 1998). It shows that summer is the main rainy season in the Alps and the topography is very essential in producing warm-season precipitation in this region. Moreover, Bertram and Mayr (2004) found that the summer lightening activities and thunderstorm initiation is more pronounced over the northern Alpine. Considering the dominance of southerly and southwesterly winds in summertime, it can be concluded that downstream convective activity is more likely than upstream convection. Already Bouët (1972) described these characteristics of Alpine precipitation. The results showed that the northern Alps have a first precipitation peak in summer and a second peak in winter. However, the southern slopes of the southern Alps have precipitation peaks in autumn and spring, and a precipitation minimum in winter.

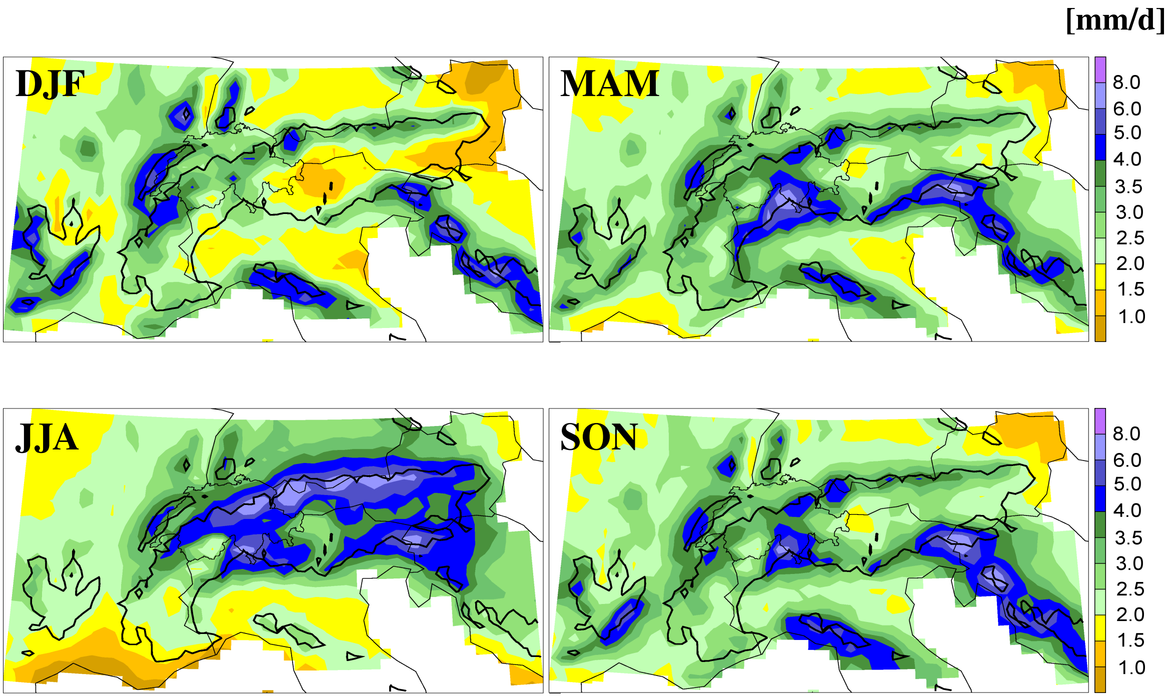

Figure 1.1: Mean seasonal precipitation for the period 1971-1990. DJF: winter; MAM: spring; JJA: summer, SON: autumn [Adapted from Frei and Schär (1998)].

Wastl and Zaengl (2007) studied the northern Alps precipitation, more specifically. In the first place, they found that in summer the highest percentage of the precipitation amount is due to the convective activity and it peaks with southerly and southwesterly flows (Fig. 1.2). Secondly, they compared the accumulated precipitation over the northern slopes of the Alps and the Bavarian Alpine foreland. As shown in Fig. 1.2, the (convective) precipitation amount for southerly and southwesterly flows is higher over the Alpine slopes than the foreland. They explain these observations with thunderstorms and showers, which are triggered over the Alps, are propagating towards northerly directions while further developing, and which may cause ample precipitation downstream of the mail Alpine ridge. Further downstream, the cells gradually decay but still leave some precipitation over Alpine foreland.

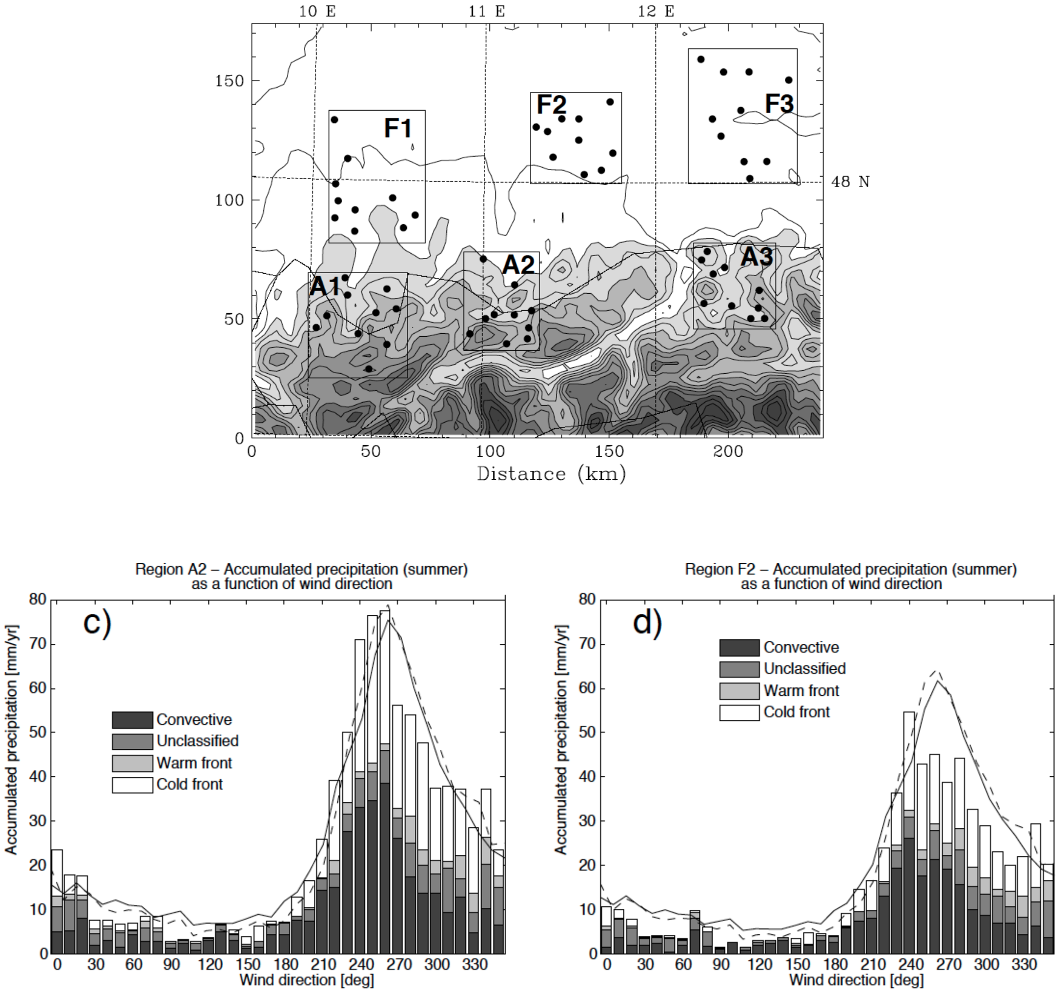

Figure 1.2: Upper panel) Location of the regions selected for investigation in Wastl and Zaengl (2007). Each region consists of 10 stations as indicated by the dots. Topography is contoured every 200 m with additional gray-scale steps every 400 m (white below 800 m). Lower panel) Accumulated summer (April to September) precipitation (mm/yr) as a function of wind direction and precipitation type for (c) region A2, (d) region F2. The normalized frequency distribution of 700-hPa wind directions is displayed with solid and dashed lines for all 6-h intervals and 6-h intervals with nonzero precipitation, respectively [Adapted from Wastl and Zaengl (2007)].

1.4 Numerical modeling

To simulate the atmosphere in weather or climate mode, numerical models are built which solve the discretized form of the conservation equations for mass, momentum and energy on a grid. Convective events are only explicitly resolved if they are at least as large as the grid size. Atmospheric convective events occur on spatial scales ranging from $\mathcal{O}(10\,\mathrm{m})$

to $\mathcal{O}(10\,\mathrm{km})$ (Orlanski, 1975), whereas the common grid spacing for general circulation models (GCM) is 100 km and for regional climate models (RCM) is 25 km. Therefore, parametrization schemes are required to represent the effect of the convection on the resolved scales.

When the first numerical climate models were developed, scientists became aware of the need for capturing the subgrid convective heating and moistening rates. Manabe and Stricker (1964) presented the first attempt to represent convection in GCMs. Later on, various parametrization schemes for moist convection were introduced (e.g. mass-flux schemes, Tiedtke (1989); adjustment schemes, Betts (1986); also see Stensrud (2007) and Arakawa (2004), for reviews). Since theses parametrization schemes cannot resolve the details of the flow, they suffer from some well-known deficiencies; e.g. a poor representation of the diurnal cycle of precipitation (Brockhaus et al., 2008) or of the soil-moisture-precipitation feedback (Hohenegger et al., 2009).

With the improved capability of modern computing systems, simulations with grid spacing of $\mathcal{O}(1\,\mathrm{km})$ are becoming possible. Hence, convection-resolving models (CRM) were introduced as an alternative to convection parameterizing models (CPM). CRMs typically use 1-3 km grid spacing and are thus able to explicitly capture deep convection with no need for parametrization (Hohenegger et al., 2008; Ban et al., 2014).

Even higher grid resolutions ($\mathcal{O}(10\text{-}100\,\mathrm{m})$) are possible now. This allows the explicit simulation of largest turbulent eddies in the atmosphere. Large eddy simulations (LES) have become very interesting over the last couple of years. However, LES models are still computationally very expensive and mostly limited to idealized simulations (e.g. Khairoutdinov et al., 2009; Heus and Seifert, 2013).

In the current research, we use CRMs to simulate summertime deep convection over topography. To this end, the Consortium for Small-scale Modeling (COSMO) model in climate mode (COSMO-CLM) is used with a grid spacing of 2 km. COSMO-CLM includes a full parameterization package consisting of a prognostic turbulent kinetic energy-based scheme (Raschendorfer, 2001), a radiation scheme (Ritter and Geleyn, 1992), a microphysics bulk scheme considering prognostic cloud water, cloud ice, precipitation, graupel and snow (Reinhardt and Seifert, 2006), and a surface layer scheme based on turbulent kinetic energy (Mironov and Raschendorfer, 2001). For this study, we do not use any parametrization for deep convection, but rather resolve convective motions as far as feasible with the employed resolution.

1.5 Objectives and outlines of the thesis

In the current PhD thesis, the effect of topography on the spatial distribution of moist convection, precipitation and the state of the boundary layer is studied. We investigate the mechanisms leading to convection initiation in different parts of the domain. The sensitivity of summertime intense precipitation to the environmental conditions and the mountain geometry is also investigated.

The outline of the thesis is as follows:

- **Chapter 2:** The impact of an isolated 3D mesoscale mountain on the diurnal cycle of moist convection and spatial distribution of precipitation is investigated. In this chapter, we tackled these questions:
  - How does the topography affect the spatial distribution of moist convection and PBL state on its vicinity?
  - Which precipitation mechanisms are dominant in different regions?
  - What mechanism causes a dry region over the mountain downstream?
  - How do the precipitation timing and pattern change for different mountain heights in terms of precipitation frequency and intensity?
- **Chapter 3:** The influence of a Gaussian-shaped mountain on producing summer extreme precipitation in different environmental conditions is studied. To this end, different atmospheric stratifications and soil moistures are used. In this chapter we investigated these issues:
  - How sensitive is the amount of accumulated precipitation during extreme precipitation events to different soil moisture contents?
  - How does the opposing effect of the different atmospheric stratification influences the accumulated precipitation during extreme precipitation events?
- **Appendix A:** As an extension of chapter 2, the role of a circular 3D mountain geometry is examined on producing warm-season extreme precipitation. Different mountain half-widths and heights are considered in the same atmospheric condition with an additional simulation over flat terrain. The objective of the appendix A is to understand:
  - How do different mountain sizes change the amount, pattern and timing of the mean and extreme precipitation?
- **Appendix B:** A cell tracking algorithm is used to track precipitating cells triggered over an elliptical 3D mountain. Five different simulations are performed. The initial atmospheric conditions are kept identical, but the angle (α) of the mountain long axis with respect to the zonal wind direction is increased from 0^o to 90^o with 22.5^o intervals. For five arbitrary days of each simulation, the cells were tracked over the mountain vicinity. The objective of this appendix is to investigate:
  - How do the longevity and distance of travel of the precipitating cells change with respect to the different αs.

  - What causes the sensitivity of the longevity and distance of travel of the cells to α?

Chapter 2

Impact of topography on diurnal cycle of summertime moist convection in idealized simulations

Impact of topography on diurnal cycle of summertime moist convection in idealized simulations*

Hanieh Hassanzadeh[1], Jürg Schmidli[1], Wolfgang Langhans[2],
Linda Schlemmer[1], Christoph Schär[1]

Abstract

The impact of an isolated mesoscale mountain on the diurnal cycle of moist convection and its spatial variation is investigated. Convection-resolving simulations of flow over 3D Gaussian-shaped mountains are performed for a conditionally unstable atmosphere under diurnal radiative forcing. The results show considerable spatial variability in terms of timing and amount of convective precipitation. This variability relates to different physical mechanisms responsible for convection initiation in different parts of the domain. During the late morning, the mass convergence from the radiatively driven diurnal upslope flow confronting the large-scale incident background flow triggers strong convective precipitation over the mountain lee slope. As a consequence, instabilities in the boundary layer are swept out by the emerging cold pool in the vicinity of the mountain, and some parts over the mountain near-field receive less rainfall than the far-field. Over the latter, an unperturbed boundary-layer growth allows for sporadic convective initiation. Still, secondary convection triggered over the leading edge of the cold pool spreads some precipitation over the downstream near-field. Detailed analysis of our control simulation provides further explanation of this frequently observed precipitation pattern over mountains and adjacent plains. Sensitivity experiments indicate a significant influence of the mountain height on the precipitation pattern over the domain.

---

[*] *Accepted for publication in Meteorologische Zeitschrift, 2015, doi:10.112/metz/2015/0653.*

[1] Institute for Atmospheric and Climate Science, ETH Zurich, Switzerland

[2] Earth Sciences Division, Lawrence Berkeley National Laboratory, Berkeley, USA

2.1 Introduction

Mountain ranges strongly influence the distribution of precipitation, both in space and time (Banta, 1990; Roe, 2005; Houze, 2012). This affects the distribution of water resources and may cause droughts or floods in the surrounding regions. Mountain-induced vertical lifting may lead to precipitation, either by adiabatic cooling and condensation, or by triggering moist convection. Hence, numerous studies have been done to understand the role of mountains in modifying the overlaying flow pattern (e.g. Queney, 1948; Smith, 1979; Durran, 1990).

Whether the flow goes over or around the mountain dramatically changes the atmospheric processes over the mountain's near field (Smith and Gronas, 1993; Schär, 2001). For dry flow past intermediate-scale elliptical mountains, the atmospheric flow regime depends mostly on two non-dimensional parameters: the non-dimensional mountain height ($\hat{h} = HN/U$; in which H is the mountain height, U is the background wind speed and N is the Brunt-Väisälä frequency) and a shape parameter $\beta = A_x/A_y$, the ratio of along-flow to perpendicular-to-flow characteristic width of the mountain. Thus, dry flows pose less complexity and have been investigated comprehensively from many points of view (e.g. Bauer et al., 2000; Crook and Tucker, 2005; Schär and Durran, 1997). However, for moist flows, the flow regime may change non-linearly from stable to conditionally unstable by reshaping the temperature profile through dynamical effects, thereby leading to condensational heating in clouds. The effect of conditional instability is represented by N_m, the moist Brunt-Väisälä frequency, and brings some complexity to the modeling of the moist flows (Miglietta and Buzzi, 2001; Kirshbaum and Smith, 2008). Due to this complexity the influence of humidity on the impinging flow over topography has yet to be investigated in full detail.

Some basic precipitation-formation processes over mountains have been studied using highly simplified and idealized 2D/3D frameworks (Schneidereit and Schär, 2000; Kirshbaum and Durran, 2004; Miglietta and Buzzi, 2004; Smith and Barstad, 2004; Fuhrer and Schär, 2005; Miglietta and Rotunno, 2009). These simplified frameworks reduce the degrees of freedom and allow a comparison to analytical models. Despite the relevance of such studies, some of the factors neglected in the simplifications are of importance, particularly at longer time-scales. For instance, some of the previous studies neglected surface and boundary layer processes as well as radiative forcing.

However, radiative forcing is the strongest driver of the diurnal cycle (DC). It regulates the amount of available energy within the planetary boundary layer (PBL) and affects the flow regime by redefining the vertical stratification. Considering radiative forcing, Mayr and Armi (2010) showed the significant influence of the diurnal heating on the Sierra Nevada downstream flow. Demko and Geerts (2010a,b) aimed at an improved understanding of the mountain circulation and its effect on orographic convective rainfall in the DC framework. While their simulations were designed to capture most of the involved physics for a specific event, their setup was used to study only a short (3 individual days) period in time.

It has also been shown that capturing convection initiation (CI) precisely is a key factor in forecasting the timing and amount of precipitation (Kottmeier et al., 2008). Thus, a series of studies was initiated within the Convective and Orographically-induced Precipitation Study (COPS) over southern Germany and eastern France (Wulfmeyer et al., 2011) to investigate the effect of the surface fluxes, soil moisture, wind profile, water vapor, and stratification on the timing, location, and amount of convection and precipitation over complex terrain (Barthlott and Kalthoff, 2011; Barthlott et al., 2011; Bennett et al., 2011; Eigenmann et al., 2011; Hagen et al., 2011; Hauck et al., 2011; Van Baelen et al., 2011).

In a recent study of the DC of warm-season precipitation, Bao and Zhang (2013) studied the initiation and development of convection over northern China. They found that in addition to the impact of the mountain-plain circulation, cold-pool dynamics play an important role in defining the precipitation pattern over the plain adjacent to the Yanshan-Taihangshan mountain ranges. The development of cold pools over a sea surface in the tropics has e.g. been studied by Addis et al. (1984), Young et al. (1995), and Tompkins (2001) and in the midlatitudes over continental areas by Weaver and Nelson (1982) and Schlemmer and Hohenegger (2014). Moreover, cold pools play an imporant role in the organization of multicell storms or squall-lines through the dynamical impact at their leading edge (Parker, 1996; Rotunno et al., 1988).

Most of the previous studies on CI over mountainous terrain have focused on single days, where the development of convection is to a large degree determined by the ambient conditions. In order to capture the feedbacks of convection onto the environment, Schlemmer et al. (2011) (hereafter S2011) established an idealized framework to examine the DC of midlatitude summertime moist convection over flat terrain and its evolution into an equilibrium state. They termed the emergent state “diurnal equilibrium”. With diurnal equilibrium an equilibrated DC of the land-atmosphere system is addressed, which is reflected in little day-to-day variability of the DC of surface precipitation (Betts, 2000), rather than in the equilibrium between the large-scale forcing and the small-scale convective response as in Arakawa and Schubert (1974). This diurnal equilibrium is not considered in short-term event-based case studies. Schlemmer et al. (2012) explored this equilibrium state and studied its sensitivity to soil moisture and atmospheric stability.

The current paper investigates the DC of the summertime precipitation and moist convection over 3D topography extending the framework of S2011. The simulations use a convection-resolving model with a grid spacing of 2 km. Previous studies have shown that this framework appropriately resolves the vertical fluxes of moisture, heat, and momentum associated with organized deep convection (Hohenegger et al., 2008; Schlemmer et al., 2011).

The main goal of the current study is to understand the spatial variability of the diurnal-equilibrium state of a conditionally unstable flow over an isolated mesoscale mountain in a setting resembling midlatitude summertime conditions. In order to understand the processes which govern the development and spatial diversity of convection, the evolution of the PBL and the processes in the free atmosphere are investigated in specific parts of the domain. An analysis of the mechanisms involved in the convection initiation and development in different regions of the mountainous domain is presented. In addition, the influence of the mountain height on the convection initiation and development over the near field is investigated from a temporal and spatial perspective.

The paper is organized as follows: Section 2.2 describes the experimental setup and the model used. Section 3.3 discusses the results. The conclusions are summarized in section 3.4.

2.2 Experimental setup

2.2.1 Model description

The simulations are carried out using version 4.28 of the Consortium for Small-scale Modeling (COSMO) model (Baldauf et al., 2011) which is the pre-release version of the unified model version COSMO-CLM (CCLM) version 5.0. The CCLM is a nonhydrostatic limited-area model that solves the fully compressible Navier-Stokes equations using the split-explicit approach (Wicker and Skamarock, 2002). The time integration is done using a third-order Runge-Kutta scheme (see Förstner and Doms, 2004) with a fifth-order advection scheme for horizontal and vertical velocities, temperature, and pressure and a second-order Bott scheme (Bott, 1989) for the advection of moist quantities. CCLM (Steppeler et al., 2003; Doms and Förstner, 2004) includes a full parametrization package consisting of a prognostic turbulent energy-based scheme of order 1.5 (Raschendorfer, 2001), a radiation scheme (Ritter and Geleyn, 1992), a one-moment microphysics bulk scheme considering prognostic cloud water, cloud ice, precipitation, graupel and snow (Reinhardt and Seifert, 2006), and a surface-layer scheme based on turbulent kinetic energy (Mironov and Raschendorfer, 2001). The 10-layer soil model TERRA_ML (Heise et al., 2003) is used to simulate the interactions between the land and the atmosphere. In contrast to S2011, soil moisture is prescribed throughout the simulation (section 2.2.3).

2.2.2 Domain and topography

The model domain covers $400 \times 200 \times 50$ atmospheric grid points with a horizontal grid-spacing of 2 km. The atmospheric vertical grid-spacing ranges between 20 m near the ground and about 1 km at the model top (at 22 km). The time step is set to 20 s. Doubly-periodic lateral boundary conditions are used and the Coriolis force is neglected. The surface elevation is set to 500 m above mean sea level (representative of the Alpine foreland)

and an isolated mountain is placed 250 km from the upstream boundary. The topography of the mountain is given by a circular Gaussian function:

$$h(x,y) = He^{-\frac{x^2+y^2}{A^2}} \tag{2.1}$$

where H is the mountain height and A is the mountain half-width. For the control simulation (referred to as H1000), we use A=20 km and H=1000 m. A simulation over flat terrain (FLAT) is run in addition with a setup identical to H1000, except for the absence of the topography.

2.2.3 Atmospheric and soil profiles and relaxation method

As in S2011, we use idealized profiles to drive our simulations. A single vertical sounding representative for summertime European climatological conditions taken from 48.25° N is applied to initialize, and the horizontal wind components (Fig. 2.1). The zonal wind is set to 2 $\mathrm{m\,s^{-1}}$ at the surface and increases to 10 $\mathrm{m\,s^{-1}}$ at the tropopause and decreases again to -5 $\mathrm{m\,s^{-1}}$ in the stratosphere, while the meridional wind speed is set to zero. To obtain a conditionally unstable stratification, a lapse rate of -7 $\mathrm{K\,km^{-1}}$ is considered for tropospheric temperature with a surface temperature of 291 K. The relative humidity profile is based on the climatology of Peixoto and Oort (1996) and similar to S2011, with values of 70 % close to the surface decreasing to 40 % in the upper troposphere. In the stratosphere values are set to 10 %. Incoming solar radiation is set to the conditsion at 48.25° N (latitude of Munich) on 12th July throughout the whole simulation.

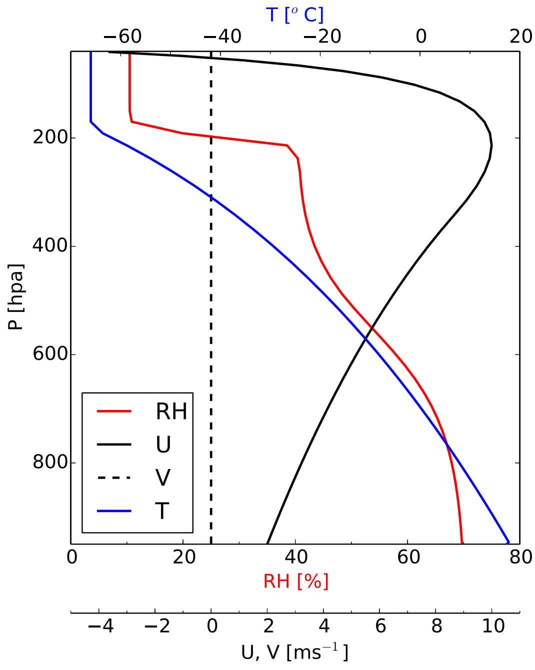

Figure 2.1: Initial profiles of the atmospheric temperature (blue), relative humidity (red) and horizontal wind components (black).

In contrast to S2011 the saturation of the soil layers is prescribed to a fixed value of 60 % for the uppermost layer, increasing to 100 % at a depth of 2.5 m. A fully interacting soil moisture was found to result in unrealistically high values of soil moisture over the mountain due to the high precipitation amounts and the neglect of lateral runoff in the land-surface model due to missing lateral water transport. The soil temperature fully interacts with the atmosphere.

White noise with an amplitude of ±1.0 K is added to the initial temperature of the first atmospheric layer to break the symmetry of the horizontally homogeneous conditions. A Rayleigh damping sponge layer is implemented above 12 km to prevent gravity wave reflection.

Large-scale forcing is prescribed as in S2011. Domain mean values of temperature, specific humidity and horizontal wind are relaxed toward the reference profiles throughout the simulation. The relaxation factor is height-dependent in a way that the upper atmospheric state is relaxed with a time scale of τ=1 day while the lower layers run without relaxation. This setup allows for an unconstrained interaction between surface buoyancy fluxes, the boundary layer, and convection with the advective and radiative forcing. The relaxation is not applied to the soil temperature profiles since the deep soil temperature remains approximately constant throughout the simulation.

2.2.4 Equilibrium state

The simulations are run for 35 days. A quasi-steady state is reached after about 15 days. This is illustrated in Fig. 2.2 for our control simulation, where the time series of the domain mean atmospheric temperature averaged over the 10 lowest layers (up to 750 m above the ground level (AGL)) as well as surface precipitation are shown. Hence, days 16-35 of the simulation are used to evaluate the diurnal equilibrium. The 20 days can be thought of an ensemble where each day is a realization of the same experiment with slightly different initial conditions.

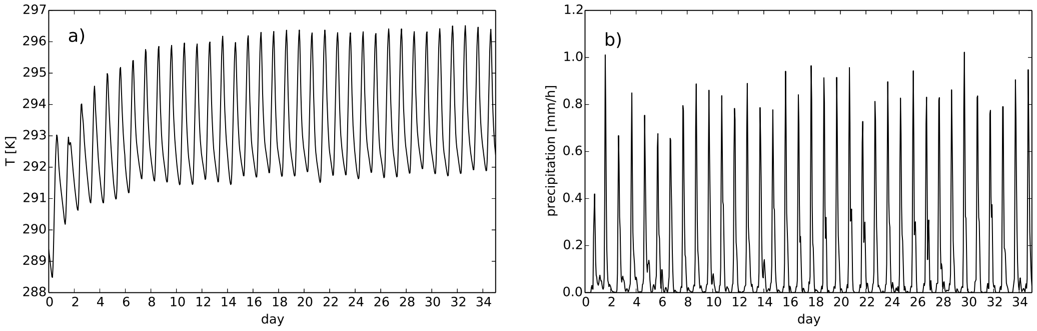

Figure 2.2: Time series of domain-mean (a) temperature for the 10 lowest atmospheric layers (up to 750 m) and (b) surface precipitation rate over 35 days of the control simulation.

In summary, our setup is similar to the CTRL simulation in S2011, except for prescribed soil moisture, weaker reference winds, a larger domain, and (of course) the mountain topography.

2.3 Results

2.3.1 Spatial diversity of precipitation and mean diurnal cycle

As shown in Fig. 2.3, the presence of an isolated mountain leads to large spatial differences in the mean daily precipitation, ranging from 22.3 mm d^{-1} in the region of the lee-side maximum, to only 0.8 mm d^{-1} in the dry regions flanking the lee-side maximum. Mean precipitation in the mountain far field amounts to 3.1 mm d^{-1}. To have an estimate of the precipitation variation in different parts of the domain, Fig. 2.4 presents along-flow variations of precipitation averaged in bands that represent the CENTER, FLANKS and DISTANT regions (see caption and Fig. 2.3 for details). This illustrates heavy precipitation over the lee for CENTER, low precipitation near the obstacle for FLANKS, and almost uniform precipitation away from the obstacle for DISTANT.

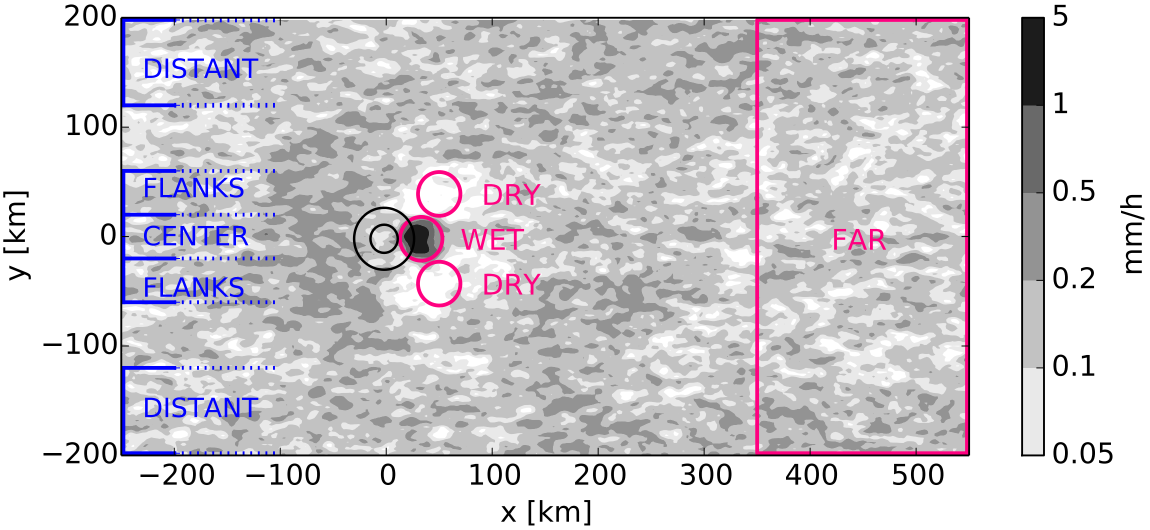

Figure 2.3: Mean surface precipitation rate (shading, 20-day mean) and mountain topography (black contours, at 250 and 750 m AGL). The blue brackets show the borders of the areas used for Fig. 2.4. The red box and circles denote the three regions used for further analysis; the three circles have the radius of the mountain half-width, A, and are centered on the precipitation maxima for WET and on the two precipitation minima for DRY. The area of the regions are 1260, 2520, and 80000 km^2 for WET, DRY, and FAR, respectively.

For further analysis, we define three additional regions (see the red circles and box in Fig. 2.3). The first region, WET, is centered around the precipitation maxima, the second region, DRY, is centered around the two precipitation minima, and the third region, FAR, is located several hundred kilometers downstream of the mountain.

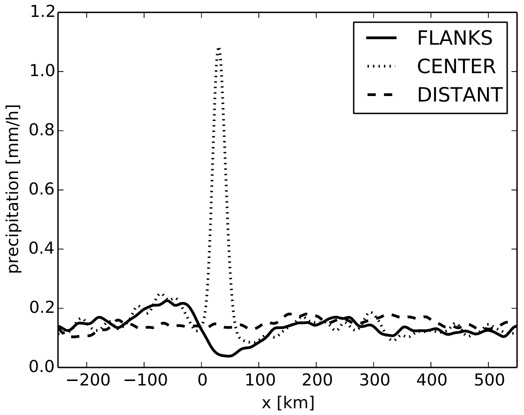

Figure 2.4: 20-day mean surface precipitation rate over the along-flow direction averaged in y-direction for the areas shown in Fig. 2.3 with blue colors.

In FLAT the evolution and spatial distribution of surface precipitation is more uniform. It resembles the convection evolution and precipitation pattern over FAR in H1000, where the effect of the topography is minimal (not shown). Further details on the DC of summertime moist convection over flat terrain are given in S2011 and Schlemmer et al. (2012) where also some sensitivity studies on the soil moisture, humidity, and atmospheric stratification over the flat terrain are presented.

The mean DC of clouds and precipitation for the three regions in H1000 and for the whole domain in FLAT is shown in Fig. 2.5. The timing of cloud formation and precipitation generation differs remarkably for the three regions. While precipitation forms around 10:00 local time (1000 LT) over WET (Fig. 2.5a), it triggers around 1500 LT over FAR (Fig. 2.5b). The cloud-free period is several hours longer over DRY than over WET or FAR. The region-mean liquid water and ice content are much higher for WET, in particular around noon (Fig. 2.5a). Furthermore, the mean daily precipitation amount is seven times higher over WET than over FAR. In contrast, DRY gets almost no precipitation (to be explained later). The highest liquid water and ice contents for the three regions are observed at 1200 LT over WET, at 1600 LT over FAR, and at 1300-1400 LT over DRY. In all regions, the precipitation peaks one hour after the clouds. The DC of clouds and precipitation over FLAT resembles the one over FAR (Fig. 2.5b,d) which both are very similar to the DC obtained by S2011. In the morning boundary layer growth in response to surface heating triggers first convective cells. Throughout the afternoon, the collision of cold pools emerging from precipitating cells over the whole domain results in deep convection and precipitation (cf. Schlemmer et al., 2012; Schlemmer and Hohenegger, 2014).

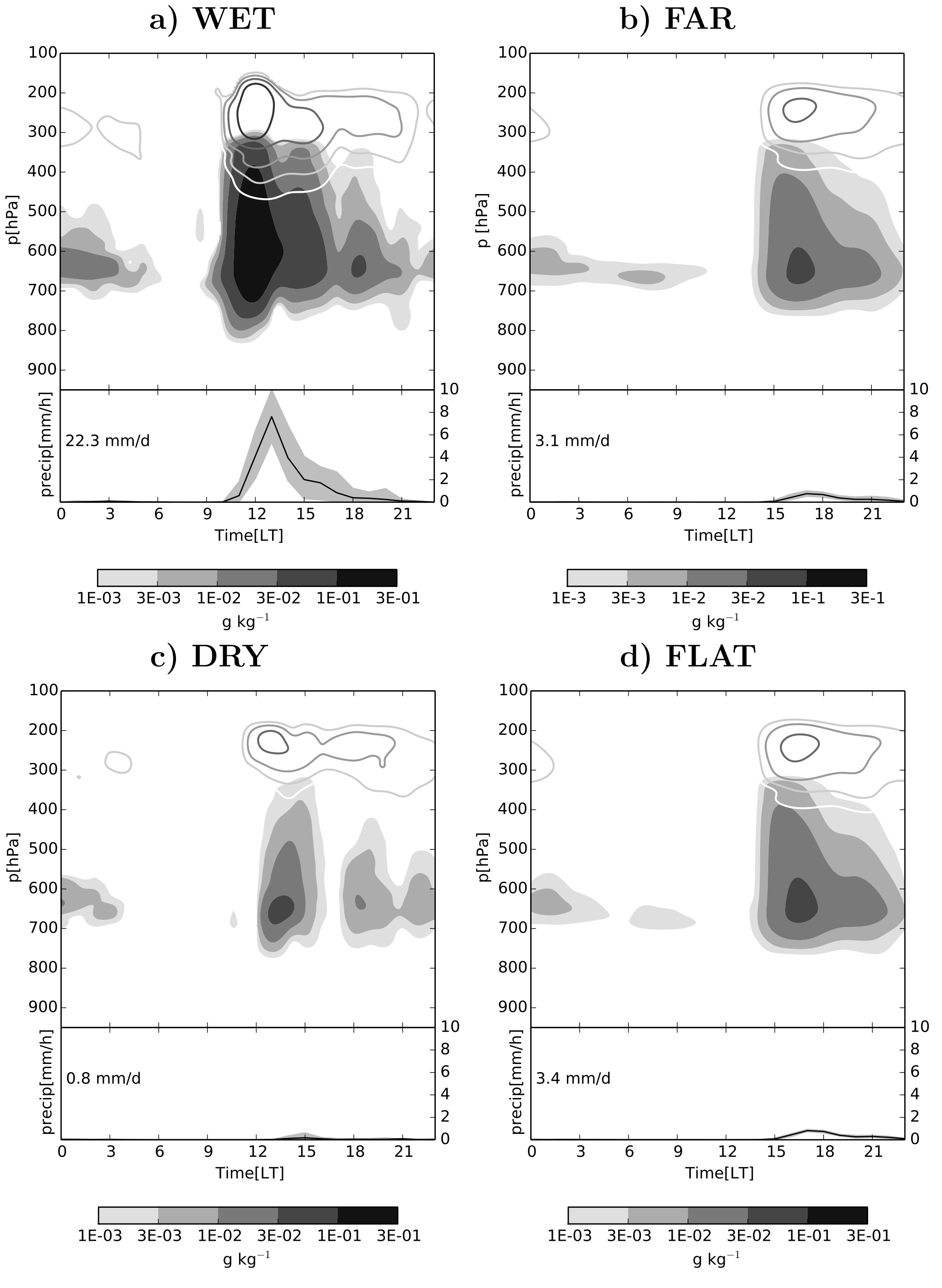

Figure 2.5: Mean diurnal cycle of clouds and precipitation over the three regions in H1000 (a-c) and the experiment without mountain (d). The upper part of the panels shows specific cloud liquid water content (g kg^{-1}, shading) and specific ice content (g kg^{-1}, contours, same intervals as shading). The lower part of the panels shows the mean diurnal cycle of the surface precipitation rate (solid line); the gray shading is the precipitation variability between the 10th and 90th percentile over the last 20 days of the simulation and the number in the lower panel is the daily mean precipitation amount.

2.3.2 Mean diurnal flow evolution and day-to-day variabilities

Fig. 2.6 shows horizontal and vertical (at $y = 0$ km) distributionsof thermodynamic and dynamic quantities at certain local times (between 0800 to 1800 LT) and averaged over the 20 days to get a sense of the mean diurnal cycle.

At 0800 LT, upstream blocking and flow-around-the-mountain is observed (Fig. 2.6a). This flow pattern as well as the vertically-propagating mountain-waves seen from the wind field in the upper panel results from the stable stratification. By 1000 LT (Fig. 2.6b), a low-level moist convergence line emerges over the lee from the combination of the thermal (upslope) circulation and orographically-forced (background) flow (see, e.g. Banta, 1990). Thus, the resulting updraft triggers deep convective clouds. The strong spatial correlation between the location of the first cloud cells and the convergence line indicates that the mass convergence is a key parameter in the triggering of the convection over the lee. This CI mechanism is similar to what has been reported by Barthlott et al. (2011) for the lee of the southern Black Forest peak, although, our case shows lower convective inhibition (CIN) in the primary-cell initiation point than they have reported (not shown). The heating of the near-surface air moreover increases the depth of the mixed layer and decreases the atmospheric stratification. Hence, no blocking effect is seen in Fig. 2.6b; instead, the portion of the flow-over-the-mountain increases.

With increasing radiative forcing, the anabatic upslope, the background flow, and – in turn – the convergence lines intensify. Consequently, the convection deepens and precipitation forms (Fig. 2.6c). The precipitation is accompanied by a cold outflow caused by evaporative cooling. The resulting cold pool is visible in the equivalent potential temperature (θ_e) contours. The cold and dry outflow lifts surrounding warm and moist air and generates secondary deep convection (Fig. 2.6d). At first the primary cold pool propagates in all directions, but then it is stopped upstream by the mountain. Therefore, two groups of cloud clusters are observed two hours after precipitation onset which get separated by a downdraft core. The first one is attached to the mountain and the other one moves away from it (Fig. 2.6e). The separation of the two updraft branches by a downdraft has also been observed for warm-season precipitation over the lee of northern Chinese mountains (Bao and Zhang, 2013). Thus, cold-pool dynamics play an important role in determining the precipitation pattern over the adjacent plain, besides the impact of mountain thermal circulations. Over the region swept by the cold pool, no further convection is triggered during the day (cf. section 2.3.4). Shortly before 1500 LT, scattered convection caused by undisturbed PBL-growth is observed over FAR. This mechanism spreads a considerable amount of precipitation over the flat part of the domain (Fig. 2.6e). In the evening (Fig. 2.6e,f), when the surface energy fluxes diminish, convection decays likewise.

Although the typical flow features are similar for all days, significant day-to-day variability in the timing and location of the convection is seen. Fig. 2.7 compares the diurnal equilibrium flow evolution with the evolution of an arbitrary day in terms of Liquid Water Path (LWP), accumulated precipitation, and near surface flow pattern. LWP is calculated

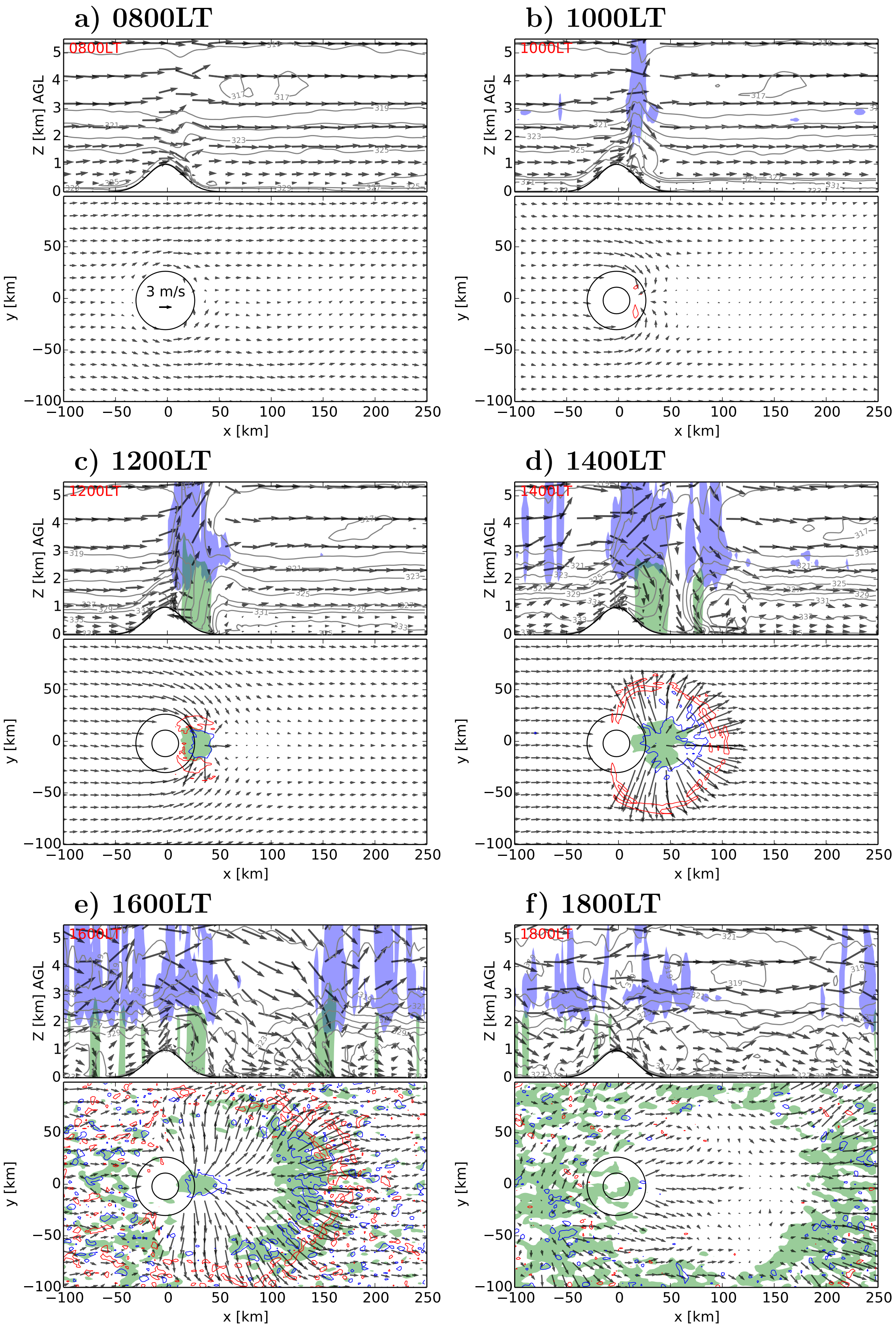

a) 0800LT

b) 1000LT

c) 1200LT

d) 1400LT

e) 1600LT

f) 1800LT

Figure 2.6: To be continued at the bottom of the next page.

as $\int_0^{p_s} \frac{q_c}{g}\, dp$, where p and p_s are the atmospheric and surface air pressure, q_c is the specific liquid water content and g is the acceleration of gravity.

The flow pattern on a specific day is much more irregular and less symmetric than the 20-day mean, in particular during the early morning and evening. This is due to the random outflow collisions all over the domain. The collision lines are visible through flow convergence and the consequent precipitation tracks. The spread between individual days is smaller during the period of strong thermal forcing in the morning and early afternoon.

We find that the flow evolution on individual days may deviate considerably from the mean flow. The flow is less symmetric around $y = 0$ mostly because cold pools propagate randomly throughout the domain. Nevertheless, the basic evolution such as lee-side triggering of deep convection, propagating cold pools, and convection suppression in the DRY region is repeated every day. In the next section we investigate the mechanisms responsible for the generation of the large differences between the three regions.

2.3.3 Initiation mechanisms for deep convection

Deep convection initiation requires three ingredients: first, a favorable environmental lapse rate, i.e. a conditionally unstable stratification; second, sufficient boundary-layer and mid-tropospheric moisture; and third, a triggering (e.g. lifting by convergence line, gravity current, PBL-growth, or topography) (Doswell et al., 1996). In other words, there should be sufficient convective available potential energy (CAPE) and some mechanisms to overcome CIN.

As mentioned in previous sections, the timing of the precipitation is different in different parts of the domain and so is the responsible mechanism for the convection triggering and deepening. The first convective activity after sunrise arises over the lee of the mountain (Fig. 2.7d). Immediately before the first cell triggers, CIN decreases dramatically over the initiation point. This CI mechanism, which triggers along the convergence line generated by the up-slope flow confronting the background wind, is called "lee-convergence" (Banta, 1984, 1986). Subsequently, the cold-air outflow suppresses any further convective updrafts

---

Figure 2.6: Summary of mean flow evolution in diurnal equilibrium (days 15-35) for the inner part of the domain; upper panels: vertical cross section of across mountain peak wind vectors, cloud liquid water (blue shading, threshold of 0.01 $\mathrm{g\,kg^{-1}}$), precipitating water (green shading, threshold of 0.1 $\mathrm{g\,kg^{-1}}$), equivalent potential temperature (gray lines, contour intervals of 2 K), and topography (black line). Lower panels: horizontal cross section of wind vectors at 250 m AGL, topography (black contours in 250 and 750 m AGL), accumulated surface precipitation of the last hour (green shading, threshold of 1 $\mathrm{mm\,h^{-1}}$) and vertical wind at 750m AGL (upward motion in red and downward motion in blue contours with the amounts of 0.2 and -0.2 $\mathrm{m\,s^{-1}}$).

in this region. Instead, new cells trigger over the leading edge of the gust front (mountain-induced cold pool mechanism). Since the cold pool moving upstream cannot pass the mountain peak, it stays stationary, confronting the background flow. Therefore, clouds form two clusters; one which is attached to the mountain, and one arc-shaped propagating away from the mountain along with the front. This gust front leaves a cloud-free region behind (Fig. 2.6e,f).

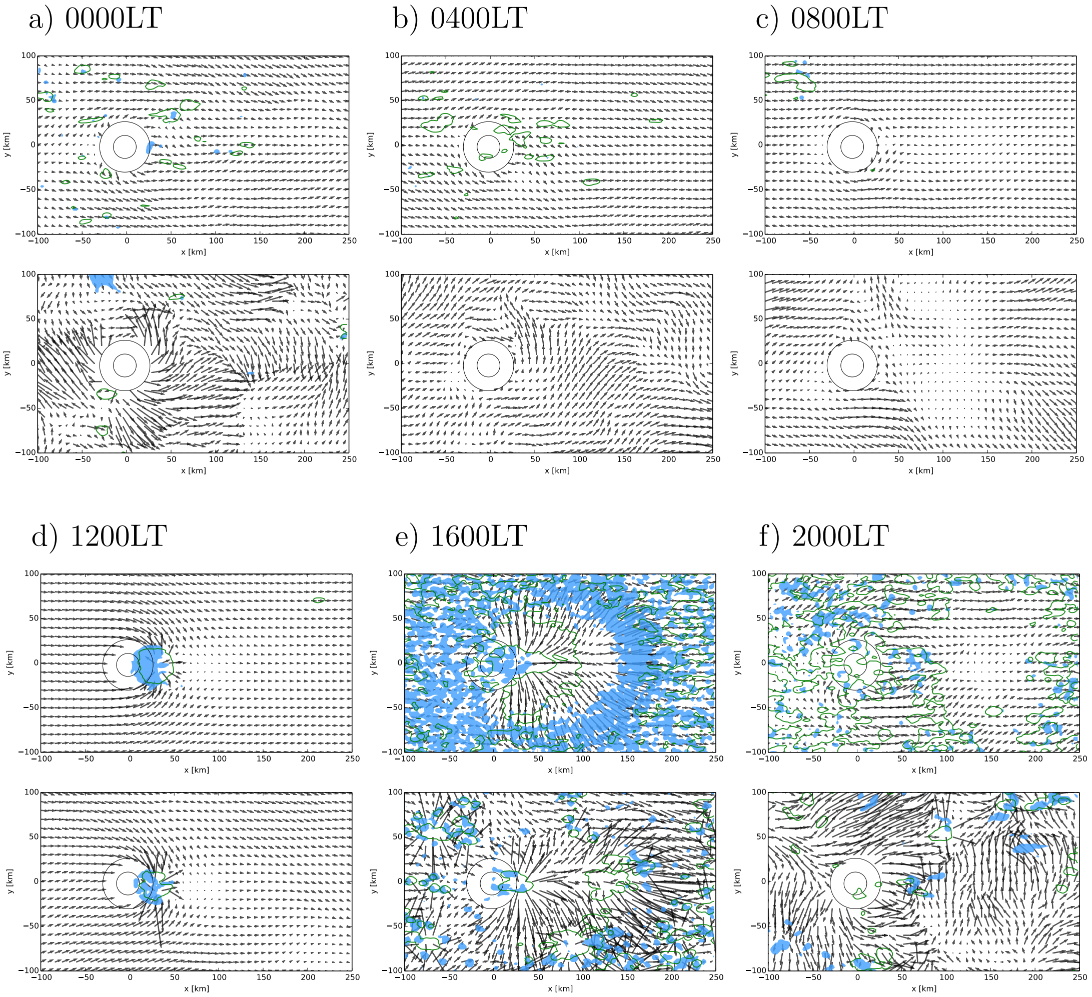

Figure 2.7: Comparison of mean flow evolution in the diurnal equilibrium phase (upper panels) against the specific flow at an arbitrary day (lower panels); panels show horizontal view of the Liquid Water Path (LWP; blue shading, threshold of 60 g m^{-2}) every 4 hours, wind vectors at 250 m AGL, accumulated surface precipitation over the last hour (green contours, threshold of 0.1 mm/h), and topography (black contours in 250 and 750 m AGL). In each frame, the upper panel is the 20-day mean and the lower panel is for one arbitrary day (day 19).

Apart from the locally triggered clouds over the near field, some random deep convection associated with surface-flux driven PBL-growth starts far enough from the mountain and is responsible for the late-afternoon precipitation over FAR (Fig. 2.6e) starting around 1500 LT. Before the random deep convection triggers, CAPE reaches its highest value (1200-1500 J kg^{-1}) and CIN its lowest (3-15 J kg^{-1}) and the surface temperature approaches its convective temperature, T_c, over this region (more details in the next section). The randomly triggered convective cells over FAR in turn give rise to precipitation and cold pools which trigger some new cells throughout the evening (1700-2100 LT) in a similar fashion as explained in Schlemmer and Hohenegger (2014). Since the location where the clouds develop and cold pools collide varies largely from one day to another, the updrafts are not clearly visible in the mean horizontal views, but for the individual days (Fig. 2.7e,f). All the processes described above are repeated each day, with considerable day to day variability.

To summarize, lee-side convergence leads to an early onset of deep convection and precipitation (from 1000 LT) over WET, whereas the outflow-induced stabilization and drying of the PBL suppresses deep convection over DRY. Over FAR both undisturbed PBL-growth and evening cold-pool mechanisms are active. A key question still remains; why do the DRY regions remain cloud-free after the gust front passage? In other words, why is the undisturbed PBL-growth not initiated in this region after 1500 LT, similar as in FAR (see Fig. 2.3-2.5)? In the next section we tackle this question by systematically analyzing the atmospheric profiles of DRY and FAR.

2.3.4 Generation of the DRY region

Fig. 2.8a presents the DC of the mean values of potential temperature (θ) and specific humidity (q_v) within the lower boundary layer (lowest 50 hPa) over DRY and FAR. The differences in both quantities are substantial from 1200 LT to 1700 LT. From Fig. 2.5 recall that the precipitation onset over FAR coincides with diminishing convective activities over DRY. The timing suggests that the deficit in θ and q_v over DRY is caused by the passage of the cold pool.

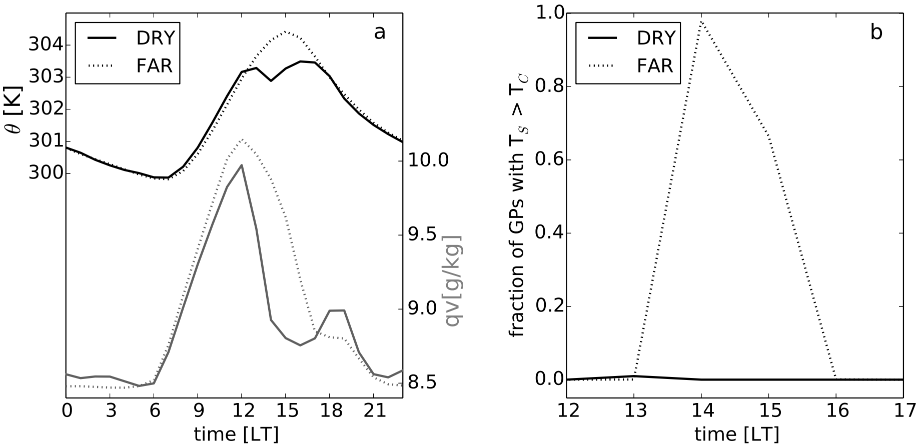

Figure 2.8: Mean diurnal cycle of (a) domain mean θ and q_v, within the lowest 50 hPa, and (b) the fraction of grid-points reaching their convective temperature T_c, in DRY and FAR.

Fig. 2.9 shows the hourly q_v budget over DRY for the time slice of interest. Before 1300 LT turbulence transports vapor from the surface and low levels upward closer to the top of the PBL. The presence of the cold-pool circulation is clearly visible at 1300 LT. At lower levels the horizontal advection of drier air leads to a drying of the lower PBL, while vertical advection of moist boundary-layer air associated with the updrafts over the leading edge of the cold pool leads to a moistening of a layer centered around 1.5-2 km. The cold-air advection also leads to a stable stratification of the lower PBL (not shown). At 1400 LT surface-driven turbulence has started to remoisten the boundary layer. Yet the horizontal advection of dry air is still stronger leading to an overall negative tendency preventing a recovery of the PBL. Only after 1600 LT, the near-surface moisture content increases again (Fig. 2.8a).

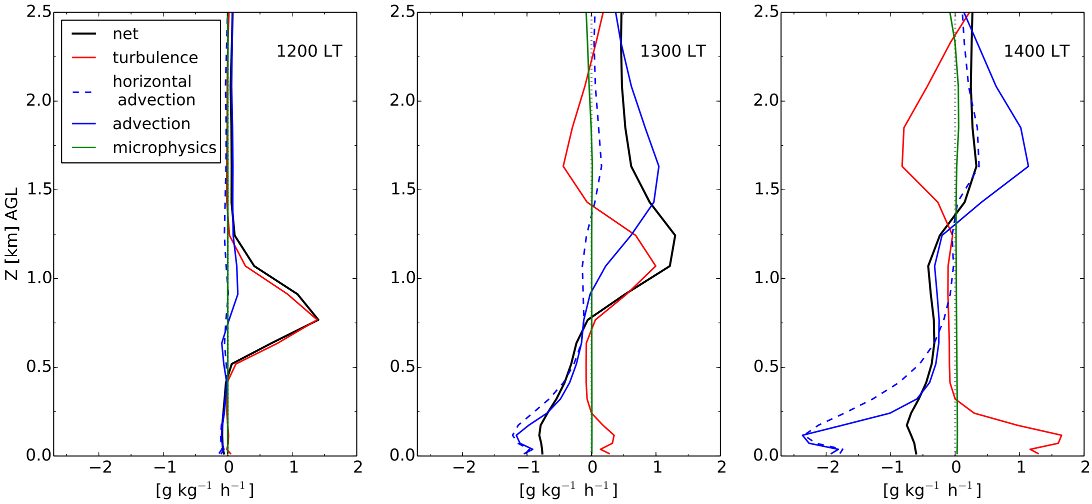

Figure 2.9: Domain mean q_v-tendency for the lowest 2.5 km AGL over DRY averaged over the 20 days in equilibrium.

Fig. 2.8b presents the fraction of the grid points in DRY and FAR that reach their convective temperature, T_c. The convective temperature in each grid-column is defined as the temperature an air parcel would have if it descended dry-adiabatically from the convective condensation level (CCL) to the surface. The CCL is defined as the lowest height at which the saturation mixing ratio equals the average mixing ratio of a 50-hPa deep near-surface layer. Apparently, the surface temperature is above T_c for 2-3 hours over FAR which causes the undisturbed PBL-growth mechanism to be active. However over DRY, hardly any grid point reaches its T_c over the same time period due to the presence of the cold pool. Consequently, when the rest of the flat part of the domain gets the late-afternoon-precipitation, DRY remains almost cloud free and receives no precipitation.

2.3.5 Sensitivity to topographic height

Varying mountain heights

The previous analysis has shown that the topography significantly modifies the DC over different parts of the domain. So far, we have considered a mountain height of 1000 m. In this section, four additional experiments with different mountain heights (H=125, 250, 500, and 2000 m) are conducted to investigate the influence of the mountain height on the timing and location of the convective precipitation. The simulations are called H125, H250, H500, and H2000, respectively. Different heights can change the flow pattern and thereby affect the generation and evolution of deep convection.

In our setup, precipitation starts first over the mountain lee for all of the experiments, but the precipitation pattern, frequency, and intensity vary significantly. Fig. A.1 shows the mean frequency and intensity of the wet hours (defined as hours where the rain amounts exceeds 0.05 mm). The left panel presents the average number of wet hours per day over the last 20 days of the simulation and the right panel presents the corresponding precipitation intensity. The shape of the intensity cores changes from a single-peak core in H125 to a V-shaped core in H2000. This change of the shape of the precipitation pattern coincides with a change of the flow around the mountain in H125 to a flow over the mountain in H2000. In H1000 the portions of the air mass flowing over and around the mountain are comparable and the shape of the core remains arc-like. This is because of the number of the primary cells usually generated over the lee which is one for H125, H250, and H500 and is three and two for H1000 and H2000, respectively.

Fig. 2.11 presents the dependency of the precipitation frequency and intensity maxima as well as the area of the most frequent and intense precipitation events of Fig. A.1 on the mountain height. For higher mountains, the frequency increases, indicating that the precipitation occurs over a longer time of the day. Also, the area having more than 5 wet hours per day is larger. The intensity on the other hand increases with height up to H500. From H1000 on, the splitting of the convective cores does not allow more precipitation accumulation over the lee. Hence, as soon as the primary convective cells split, the intensity maxima start to decrease. Nonetheless, the cores are so close to each other in H1000 that the area of the intense precipitation is still large. This area shrinks for H2000.

Fig. 2.11b shows moreover that maximum precipitation intensity occurs for comparatively small mountains (500-1000 m) as seen in the area with high intensity shown in Fig. 2.11d. This is consistent with the occurrence of vertical motion in the mountain airflow bifurcation (Schär and Durran, 1997) and also qualitatively consistent with observations of precipitation over the Hawaiian Islands (Smith et al., 2012).

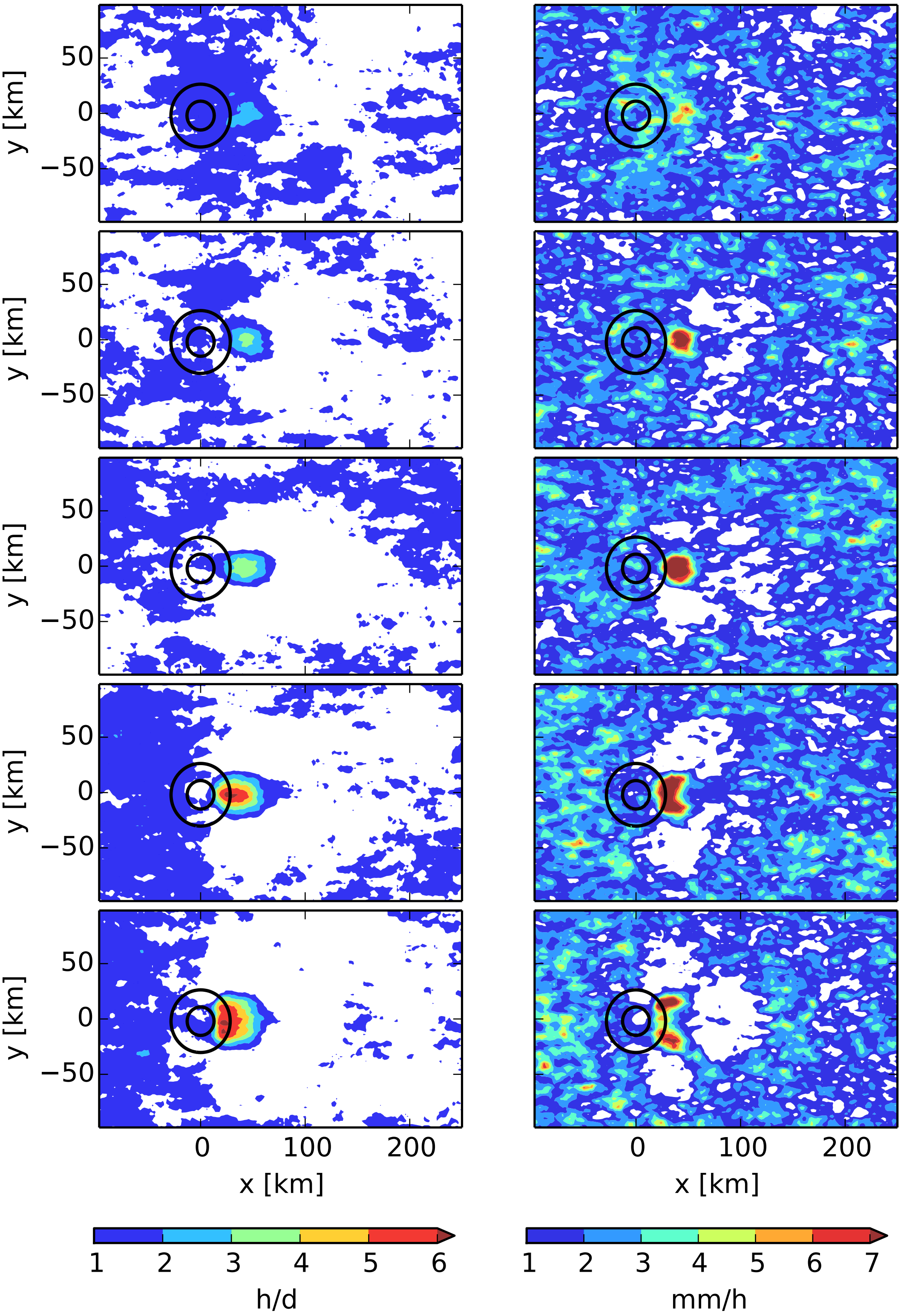

Figure 2.10: Mean surface precipitation frequency (left panel) and intensity (right panel) for experiments with different mountain heights (top to bottom, H = 125, 250, 500, 1000, and 2000 m). Frequency is defined as the number of wet hours (precipitation > 0.05 mm) per day, and intensity is the mean precipitation during wet hours.

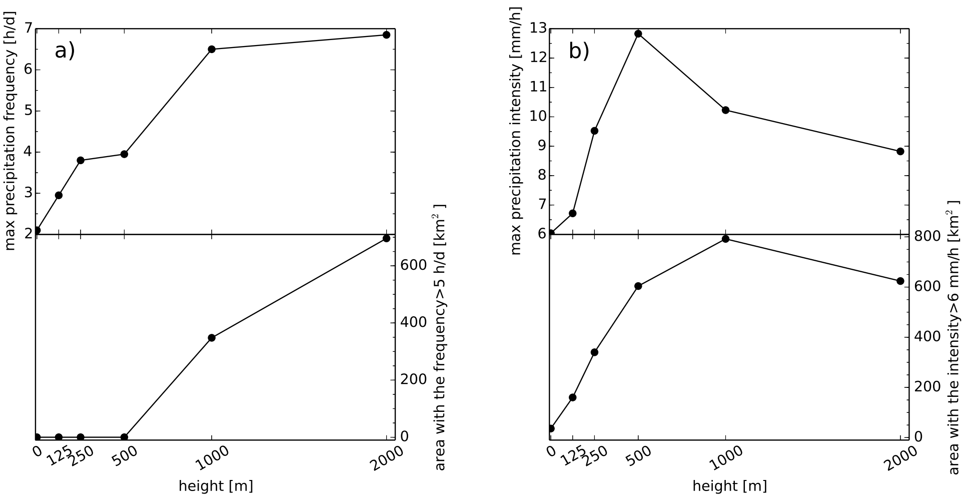

Figure 2.11: Variation of maximum precipitation frequency (top left) and maximum precipitation intensity (top right) with mountain height. Lower panels show the variation of the area with frequent ($> 5\,h\,d^{-1}$) and intensive ($> 6\,mm/h^{-1}$) precipitation with mountain height. The figure is based on the data shown in Fig. A.1.

Diurnal cycle of the flow regime and timing of precipitation onset

As discussed in the previous section the flow regime affects the amount and distribution of precipitation by regulating the portion of the flow directed over or around the mountain. The flow regime changes not only from case to case, but also over the course of the day for each case, through the diurnal forcing. Nevertheless, the determining atmospheric regime for the precipitation pattern is the regime established when the first convective cell triggers.

Generally, the atmosphere is in a stable state during the night. After sunrise, the boundary layer grows through sensible heating and the stability decreases. The more unstable the atmosphere gets, the larger the fraction of air that makes it over the mountain. Fig. 2.12 shows the mean DC of the Brunt-Väisälä Frequency (N) and the non-dimensional mountain height ($\hat{h}$), which are the criteria used to define the flow regime. The values are integrated from the lowest atmospheric layer to the respective mountain height. This is done over FAR, where the flow is less disturbed by the mountain. For $\hat{h} \gg 1$, the atmospheric stratification is strong and the around-the-mountain flow dominates. For $\hat{h} \leq 1$, the stratification is weak or neutral and the over-the-mountain flow is dominant. With this definition, the atmosphere up to the mountain top is already unstable at 0800, 0900, 1000, and 1200 LT in H125, H250, H500, and H1000, respectively. But, it always stays stable for H2000. The stability increases again in the late afternoon in all of the cases redirecting the flow around the mountain. Fig. 2.13 presents the DC of the precipitation maximum, defined as the average over the 10 grid points with the highest precipitation amount in the domain. Apparently, the daytime maxima are associated with lee precipitation. The timing of the triggering of the first cells is affected by the topographic lifting and up-slope

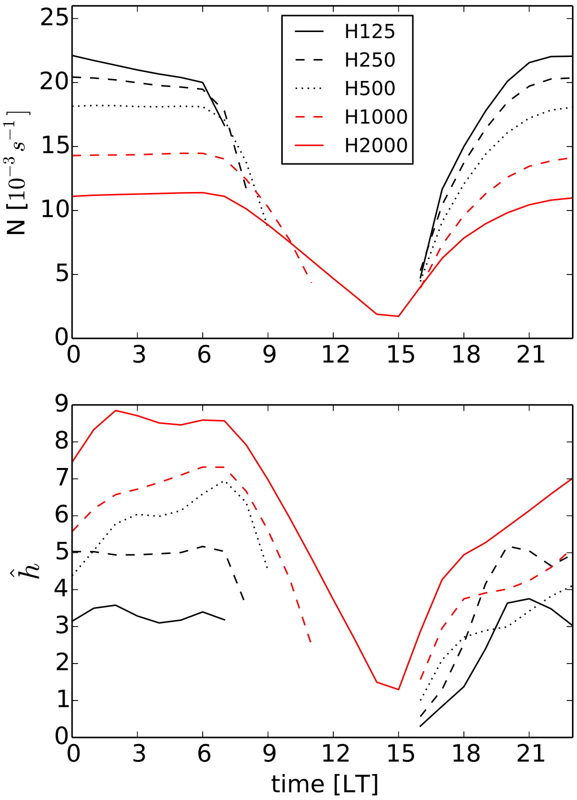

Figure 2.12: Mean diurnal cycle of domain mean static stability (N) and non-dimensional mountain height ($\hat{h} = N\,H/U$), where N and U are averaged between the lowest atmospheric layer and the mountain height over FAR. Values are suppressed for time periods with $N^2 < 0$.

flow through the strengthened lee convergence. Both increase for higher topographies (Vergeiner and Dreiseitl, 1987). Thus, the precipitation onset is earlier over the higher mountains. The second reason for the earlier precipitation is that PBL development starts earlier over the higher topographies and the PBL height exceeds the LCL and LFC earlier, allowing for earlier deep convection. This is in line with the findings of Barthlott and Kirshbaum (2013). The value of the precipitation maxima is also a function of the flow regime. That is, they increase with H in over-the-mountain regimes and decrease again for the cases with the primary-cell-split. This explains the results in Fig. 2.11b. Apart from that, evening precipitation maxima diminish almost at the same rate for all the cases. Hence, earlier precipitation onset for higher topographies and almost the same termination time explain the increased precipitation frequency seen in Fig. 2.11a.

2.4 Conclusions

The impact of an isolated mountain with a half-width of 20 km on summertime moist convection is investigated. The simulations are run for 35 days and after about 15 days a state of diurnal equilibrium is reached. This diurnal equilibrium state is characterized by

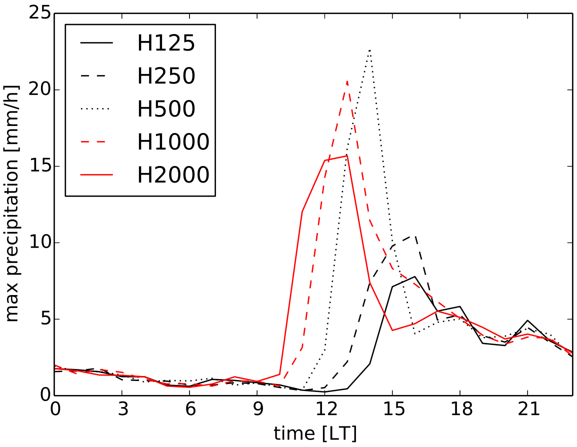

Figure 2.13: Diurnal cycle of the hourly mean surface maximum precipitation (averaged over the 10 grid points with the highest values).

repeating diurnal cycles and can be considered as an ensemble of single-day simulations with slightly different initial conditions.

Results show large spatial differences in the mean surface precipitation amount. While there is ample precipitation over the mountain lee slope (7.5 times the domain mean value), some adjacent regions only 40 km away get very little rain (0.25 times the domain mean value). Only far away from the mountain, the precipitation amounts approach the characteristics of the situation without topography.

It is shown that these spatial variations are generated by different convection initiation mechanisms over different parts of the domain. Over the lee, convection is triggered in the morning from the convergence of the anabatic mountain circulation and the background flow (lee-convergence). Convection triggered through this mechanism initiates a cold pool that propagates through the domain. In the direction facing the mountain, the cold pool remains stationary, while in the downstream direction, it propagates and numerous secondary convective cells are triggered along the leading edge. Some ten kilometers away from the lee-side precipitation maxima, no convection can be triggered because the cold pool dries and thus stabilizes the boundary layer. Over the flat part of the domain convective clouds form on top of a turbulent boundary layer. These cells deepen and organize into larger patterns due to cold-pool dynamics over the diurnal cycle.

The precipitation and convection show a very strong sensitivity with respect to the mountain height. The mountain height affects the precipitation onset by regulating the lee-convergence strength and the precipitation pattern by changing the flow regime. For higher mountains, the hourly precipitation frequency is increased due to the earlier triggering. However, the precipitation intensity is more dependent on the prevailing flow regime. Precipitation intensity increases with mountain height as long as the flow-over regime is dominant. Once the mountain height becomes sufficiently large to enforce a flow-around regime, precipitation intensity decreases due to the resulting splitting of the primary convective cell.

The current study aims at investigating the processes responsible for the summertime convection and precipitation over mid-latitude topography. Although the model and setup used are well suited for the current study, the role of additional factors such as interactive soil moisture, more complex environmental profiles, land-sea contrasts or more sophisticated mountain circulation effects are of interest. The current study will be continued spanning a larger parameter-space to better understand the role of the key factors that determine summertime convection over complex topography.

Acknowledgements: This research was supported by Swiss National Science Foundation (SNSF) grant 200021_132614. Special thanks are given to Steven Böing and the two anonymous reviewers for their insightful comments, which improved the quality of the paper. Authors are also grateful for technical support by Anne Roches and Daniel Lüthi. The numerical simulations have been performed on the Cray XC30 at the Swiss National Supercomputing Centre (CSCS) using the Consortium for Small-scale Modeling in climate mode (COSMO-CLM).

Chapter 3

Impact of topography on summertime extreme precipitation events in different environmental conditions

Impact of topography on summertime extreme precipitation events in different environmental conditions*

Hanieh Hassanzadeh[1], Jürg Schmidli[1],
Linda Schlemmer[1], Christoph Schär[1]

Abstract

The influence of a circular Gaussian-shaped mountain on producing summertime extreme precipitation is studied in an idealized framework for different environmental conditions. The different conditions are created by varying soil moisture and atmospheric stratification. The results indicate that the dry soil (if the moisture requirement for cloud formation is met) highlights the role of the mountain in producing extreme precipitation events. That is, for dry soil precipitation may just occur over the mountain near field, whereas over the flat terrain very rare precipitation event could be seen. The strongly stratified simulations also show larger accumulated-precipitation amounts. However, since this happens both over the mountain, in the near field and in the far field, it is considered a thermodynamical effect of the atmosphere, rather than the effect of the mountain itself. More interestingly, for varying stratifications, two opposing effects are seen on influencing extreme events. Weakly stratified cases produce stronger precipitation due to stronger cold-pools, whereas, strongly stratified cases have stronger precipitation owing to the other mechanisms, e.g. lee-convergence and boundary layer growth.

---

* *Paper in preperation.*

[1] Institute for Atmospheric and Climate Science, ETH Zurich, Switzerland

3.1 Introduction

Extreme precipitation events have attracted the attention of the meteorologists in the recent decades. The frequency of the extreme events has increased, likely as a result of current climate change (e.g. Easterling et al., 2000; Frich et al., 2002). Detailed studies (e.g. Christensen and Christensen, 2003) show that the trend changes, either for frequency or intensity of the extreme rainfall, are strongly tied to the warming aspect of the climate change. Although the outcome of these studies are very valuable in decision making for the climate change mitigation and adaptation, other influencing factors are ignored to some extent. Fully understanding the extreme precipitation events (as a complex problem), however, needs considering different aspects of the issue. We should break down the problem to small pieces and investigate the impact of the other atmospheric and soil features (e.g. stratification, soil moisture) on the processes involved in the event initiation.

Atmospheric moisture content and moisture-holding capacity are among the defining requirements for triggering of the extreme events (Trenberth et al., 2003). These two factors are related to the available moisture and the temperature profiles. In addition, the underlying topography and the ensuing mountain circulations affect extreme precipitation events by introducing new precipitation mechanisms (Prudhomme and Reed, 1998; Viviroli et al., 2007). In this study, we investigate the impact of the mountains on extreme precipitation characteristics (intensity and duration) in different environmental conditions. By “extreme”, we do not mean the very extreme precipitation events which we could pick for instance from a 10-year (or longer) climatology data. Instead, we look at the higher precipitation percentiles in a month-long period. We use idealized simulations to investigate the influence of a single mountain in producing intense precipitation for different environments as characterized by atmospheric instability and soil moisture. These two parameters are found to have a crucial impact on the mean diurnal cycle of precipitation over land (Schlemmer et al., 2011). Here, we investigate whether the same changes are seen over the mountains. Also, we are interested to know whether the topography or the environmental conditions play the most important role on the extreme precipitation events (for the simulation setup used here).

The paper is structured as follows. In section 3.2, the model and setup used for the experiments are explained. We discuss the results in section 3.3 and finally, the conclusion are drawn in section 3.4.

3.2 Experimental setup

3.2.1 Model

Version 4.28 of the Consortium for Small-scale Modeling in climate mode (COSMO-CLM) is used to run the numerical simulations. COSMO is a non-hydrostatic limited-area model and is used here in a convection-resolving setup. Therefore, the whole set of parametrization is used except for convection which is explicitly resolved. For more details on the employed parametrizations, as well as the model dynamic equations, the reader is referred to Hassanzadeh et al. (2015).

3.2.2 Domain setup

The domain and setup are similar to the control simulation in Hassanzadeh et al. (2015). Here we highlight the most important points. The simulations are performed over a domain of 400×200×50 grid points (GPs). The vertical grid spacing is varied from 20 m near the surface to 1 km in a 50 vertical levels mesh with the highest level at 22 km above the ground level. The horizontal grid spacing of 2 km is applied to explicitly capture deep convection. A large time step of 20 s is set to fulfill the numerical convergence criteria. The surface elevation is 500 m above mean sea level as representative for the Alpine foreland, with an isolated mountain defined as

$$h(x,y) = He^{-\frac{x^2+y^2}{A^2}} \tag{3.1}$$

where H and A are the mountain height and half-width, respectively. The mountain is centered at 250 km from the upstream boundary (Fig. 3.1). For all of the simulations, we use A=20 km and H=1000 m. The lateral boundaries are periodic and the Coriolis force is turned off.

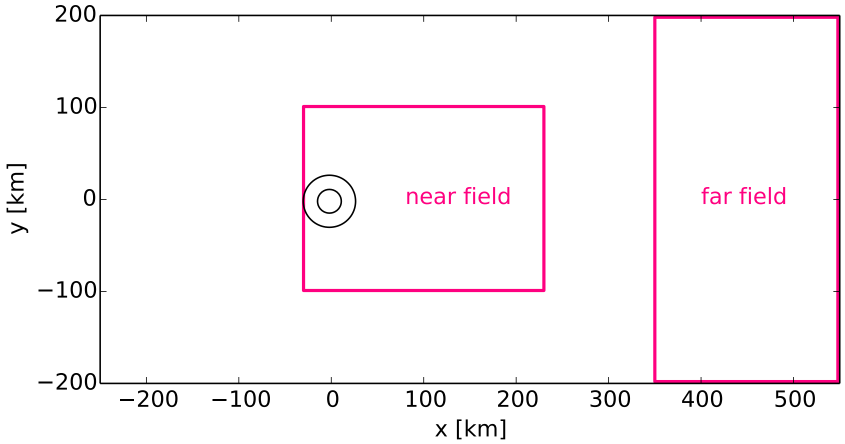

Figure 3.1: Horizontal view of the whole domain; indicating the position of the mountain near field and far field. Black circles are the mountain contours at 250 and 750 m above the ground level, where the mountain height is 1000 m.

3.2.3 Input profiles and equilibrium state

We set the initial and reference conditions as vertical 1D soundings. The zonal wind (see Fig. 3.2) has a sheared profile, increasing from $2\,\mathrm{m\,s^{-1}}$ at the surface to $10\,\mathrm{m\,s^{-1}}$ at the tropopause and decreases to $-5\,\mathrm{m\,s^{-1}}$ at the highest level (similar to summertime European climatological conditions at 48.25^o N corresponding to the latitude of Munich). The meridional wind is set to zero. The relative humidity is decreasing from 70% near the surface to 40% at the mid-troposphere with a constant value of 4% for the stratosphere. These profiles are based on the climatology of Peixoto and Oort (1996). The surface temperature is set to 291 K and the soil temperature fully interacts with the atmosphere. Similar to Hassanzadeh et al. (2015), the soil saturation is prescribed from some fixed values (see bellow) in the uppermost layer, increasing to 100% at a depth of 2.5 m. The soil type is set to loam. The diurnal cycle of the incoming solar radiation is also prescribed as it is at 48.25^o N on 12th July throughout the whole simulation.

To investigate the impact of the soil moisture and atmospheric stability, we perform two sets of simulations. In the SM set, the soil moisture of the upper layer is changed from 30 to 80% with 10% intervals; namely, SM30, SM40, SM50, SM60, SM70 and SM80. In this set, the temperature lapse rate (-dT/dz) is fixed to 7 K/km. In the LR set, the temperature lapse rate is varied with the values of 4, 5, 6, 7 and 8 K/km, ranging from stronger to weaker stratification. The simulations are called, LR4, LR5, LR6, LR7 and LR8. The soil moisture of the upper layer is set to 60%. Note that LR7 and SM60 are the same simulations and identical to the control simulation in chapter 2.

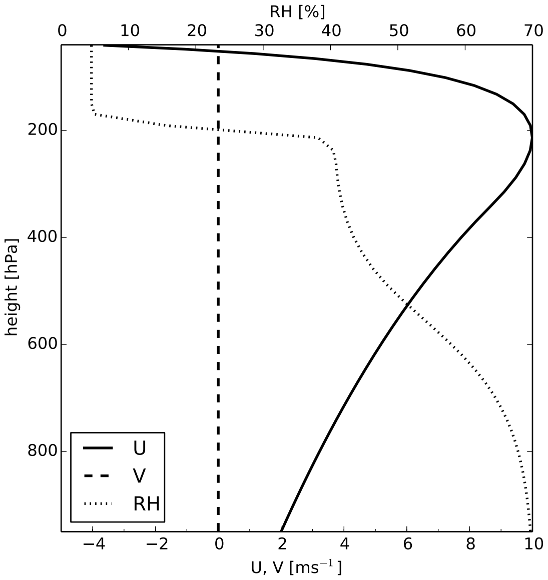

Figure 3.2: Initial profiles of the relative humidity and horizontal wind components.

As in Hassanzadeh et al. (2015), the large-scale forcing is represented by relaxing the vertical profiles of temperature, relative humidity and horizontal wind towards the reference profiles throughout the simulations. The relaxation factor is height-dependent, allowing the lower layers to run without relaxation and forcing stratosphere properties to relax with a time scale of τ=1 day. This setup allows the boundary layer and convection to develop freely through the atmosphere and soil interaction (in response to the radiative forcing).

The simulations are run for 35 days and reach their equilibrium state after 15 days (see Hassanzadeh et al., 2015). The equilibrated days (16-35) can be thought of as an ensemble where each day is a realization of the same experiment with slightly different initial conditions. The model data output frequency is half an hour. The output for the surface precipitation is also the amount accumulated for the last half an hour of the simulation. Therefore, whenever we talk about the hourly precipitation, the precipitation output is multiplied by two.

3.3 Results

The aim of this study is to understand the influence of an isolated mountain on the occurrence of extreme precipitation in different environmental conditions with a focus on soil moisture and atmospheric stability impacts, both of which can strongly affect the boundary layer vertical moisture and temperature profiles.

For flash floods, a high amount of the accumulated precipitation in a short time period is essential as there is not enough time for infiltration, efficient runoff or evaporation. Hence, not only the instant precipitation intensity, but also the duration of the event is critical for estimating the flash flood potential. We also discuss the precipitation mechanisms responsible for the occurrence and timing of intense precipitation. The mechanisms seen here, are the same as in chapter 2. Here, we summarize them shortly: after sunrise, convective precipitation occurs over the mountain lee due to convergence of the thermal flow with the impinging flow. Later, precipitation occurs along the leading-edge of the primary cold-pool, which was generated by the mountain convection. In the afternoon, boundary layer (BL) growth may trigger deep convection and lead to precipitation. Finally in the evening, the cold outflows generated from the afternoon precipitation collide and produce more convective clouds and precipitation. However, owing to the different surface fluxes and atmospheric profiles, the timing and importance of the four mechanisms varies from simulation to simulation.

To differentiate the mountain impact from the thermodynamical effects, we distinguish two parts of the domain from each other; the near field and the far field (Fig. 3.1). The near field is confined in x = [-30, 230] km and y = [-100, 100] km and is strongly influenced by the mountain. The far field is defined by x = [350, 550] km and y = [-200, 200] km. In this region, precipitation changes result mostly from changes in the thermodynamic conditions. All four mechanisms described above are potentially subjected to occur on the near field. But, only the latter two are seen over the far field.

3.3.1 Impact of soil moisture

The mean state

Variations in soil moisture directly affect the partitioning of the surface fluxes according to the water available for evaporation. The surface latent heat flux increases and sensible heat flux decreases with increasing SM, in the current study (Table 3.1). Therefore, the BL is deeper, warmer and drier for lower SM values. This can be seen in Fig. 3.3, which shows the atmospheric mean temperature and relative humidity in the diurnal equilibrium for the far field. The far field state is of interest, since due to the periodic boundary condition, it also represents the upstream conditions.

The mean diurnal cycle of the area-averaged precipitation is shown in Fig. 3.4a,b. The first precipitation maximum over the far field results from the afternoon BL growth mechanism, and the second (if any) is triggered by the late afternoon collisions of cold-pools. However, over the near field, there is an early onset of precipitation due to lee convergence. In the afternoon, the primary cold-pool precipitation coincides with the BL growth precipitation over the near field. Hence, to recognize which mechanism is dominant, we compare the precipitation values of near and far field at each time. If the value over the near field is higher, the cold-pool mechanism is prevailing. Otherwise, it is the BL growth which dominates or the both are equally influential. It can be seen that both the timing and the amount of the mean precipitation over the near and far field differ from each other.

Table 3.1: Mean surface heat fluxes (net radiation, latent heat and sensible heat) and mean daily surface precipitation over the far field, for the SM set. The units of the heat fluxes are in [W/m^2] and the unit of the surface precipitation is in [mm/d].

Surface heat fluxes	SM30	SM40	SM50	SM60	SM70	SM80
Net radiation	152.6	164.2	170.9	174.1	172.2	173.4
Latent heat	76.4	107.2	122.7	134.8	144.2	145.7
Sensible heat	66.8	52.1	43.8	35.6	25.3	24.8
Mean precipitation	1.21	1.89	2.84	3.16	3.27	2.95

Fig. 3.4c shows the mean daily evaporated and precipitated water from/over the surface. First of all, it shows that the evaporation is higher than the precipitation over both the near and far fields. Secondly, it indicates that the mountain near-field receives more mean daily precipitation than the far field. The highest mean daily precipitation over the near field

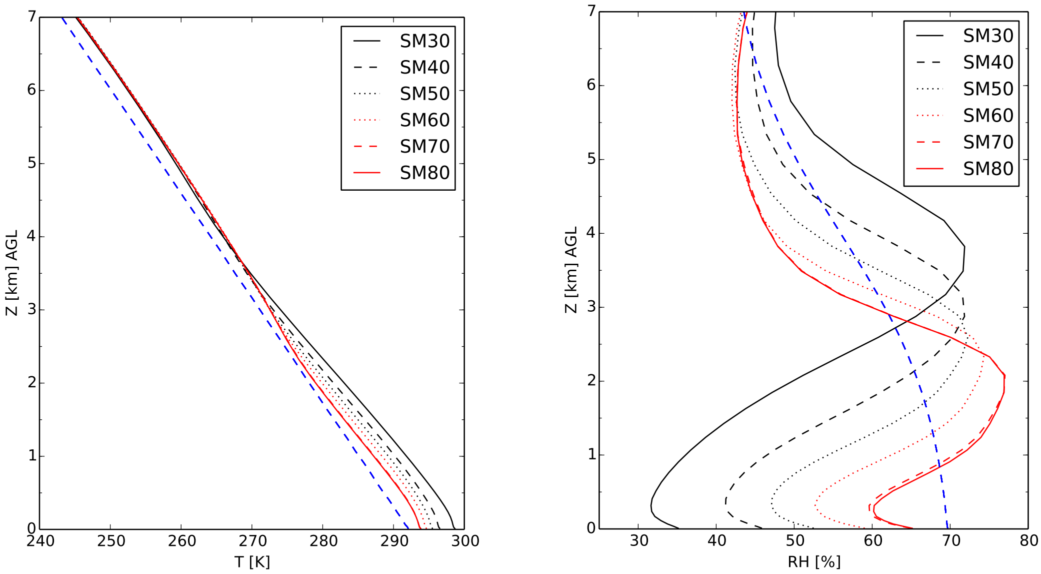

Figure 3.3: Initial (blue dashed line) and equilibriated 20-day mean profiles of the atmospheric temperature (left) and relative humidity (right) for the lowest 7 km, over the far field for the SM set.

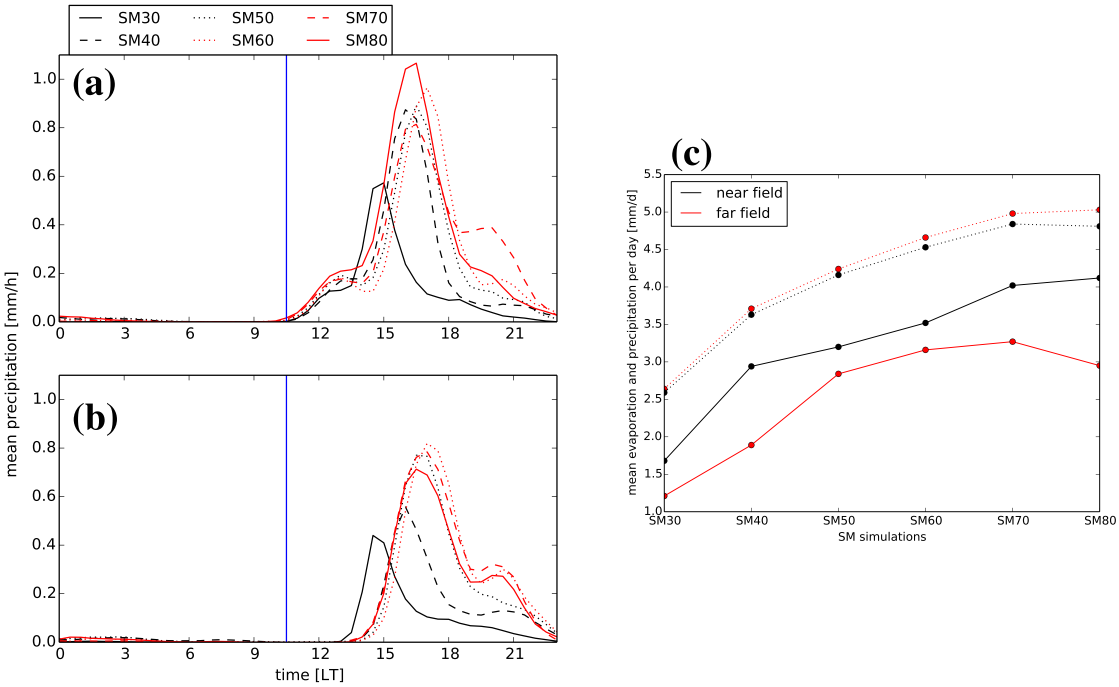

Figure 3.4: Mean diurnal cycle of area-mean precipitation for the SM set, averaged over the 20 equilibrium days for (a) near and (b) far field. The blue vertical line indicates 1030LT (for easier comparison of different plots). (c) mean daily surface evaporation ($^{LH}/_{L_v\,\rho_w}$; dotted lines) and precipitation (solid lines) for the SM set. LH, L_v and ρ_w are the latent heat flux, latent heat of evaporation for water and density of water, respectively.

occurs for SM80, whereas, over the far field, SM70 has the highest amount. However, the evaporation difference between the two fields is insignificant.

Fig. 3.5a shows the spatial variation of the mean precipitation over the near field. It illustrates the effect of the mountain in producing higher precipitation amounts over its vicinity (as shown in Fig. 3.4c). The role of the mountain in producing the precipitation is highlighted for lower soil moisture contents, where rarely any precipitation is seen over the flat part of the domain (for instance, see SM30 in Fig. 3.5a).

Extreme precipitation characteristics

Next, we focus on extreme precipitation events during the diurnal equilibrium period. Fig. 3.5b illustrates the horizontal distribution of the GPs with the intense precipitation over the near field. We take the 99th percentile of the GP precipitation for each half an hour output over the 20 days as a representative of the intense precipitation over any GP (considering the absolute maximum precipitation of each GP leads to noisy plots). The shapes of the highly precipitated area in Fig. 3.5 indicate that the mountain-flow regime (Fig. 3.6) varies for different simulations, at the time of lee convection triggering (around 10:30). The flow goes over the mountain for lower soil moisture contents due to a weakly-stratified atmosphere in the morning. The stratification is weakened mostly owing to a higher sensible heating and a quicker (and deeper) convective BL development. However, for higher soil moisture contents the sensible heating is lower. Therefore, the BL develops slower and shallower leading to strongly-stratified flows, where the around-mountain flow is predominant.

During the diurnal cycle, the extreme precipitation intensity varies remarkably. We measure the intensity by the 99.9th percentile of GP precipitation (Q99.9). To define Q99.9 for each time during the diurnal cycle, we take the 99.9th percentile of all precipitation amounts at that specific time of the day, for all 20 days and over the all GPs of the region of interest (hereafter, P-sample-set).

Fig. 3.7a,b show the diurnal cycle of Q99.9 over the near and far field for the the SM set. Over the far field, the most intense precipitation is triggered by BL growth in the afternoon. As the soil moisture increases, the evening peak of extreme precipitation increases due to the presence of more moisture for cloud formation and precipitation onset. However above SM60, a limitation behavior is seen for extreme precipitation, meaning that the further increases in SM do not make much difference. Over the near field, for the driest case (SM30), the highest precipitation amounts occur at noon owing to the deep convection generated by strong mountain circulations. However, for the moister simulations, the afternoon cold-pool mechanism produces the most intense precipitation.

The diurnal cycle of mean accumulated precipitation over the GPs with the precipitation higher than Q99.9 is shown in Fig. 3.8. The accumulation over each GP in P-sample-set is calculated as the sum of the precipitated water, during the current precipitation event.

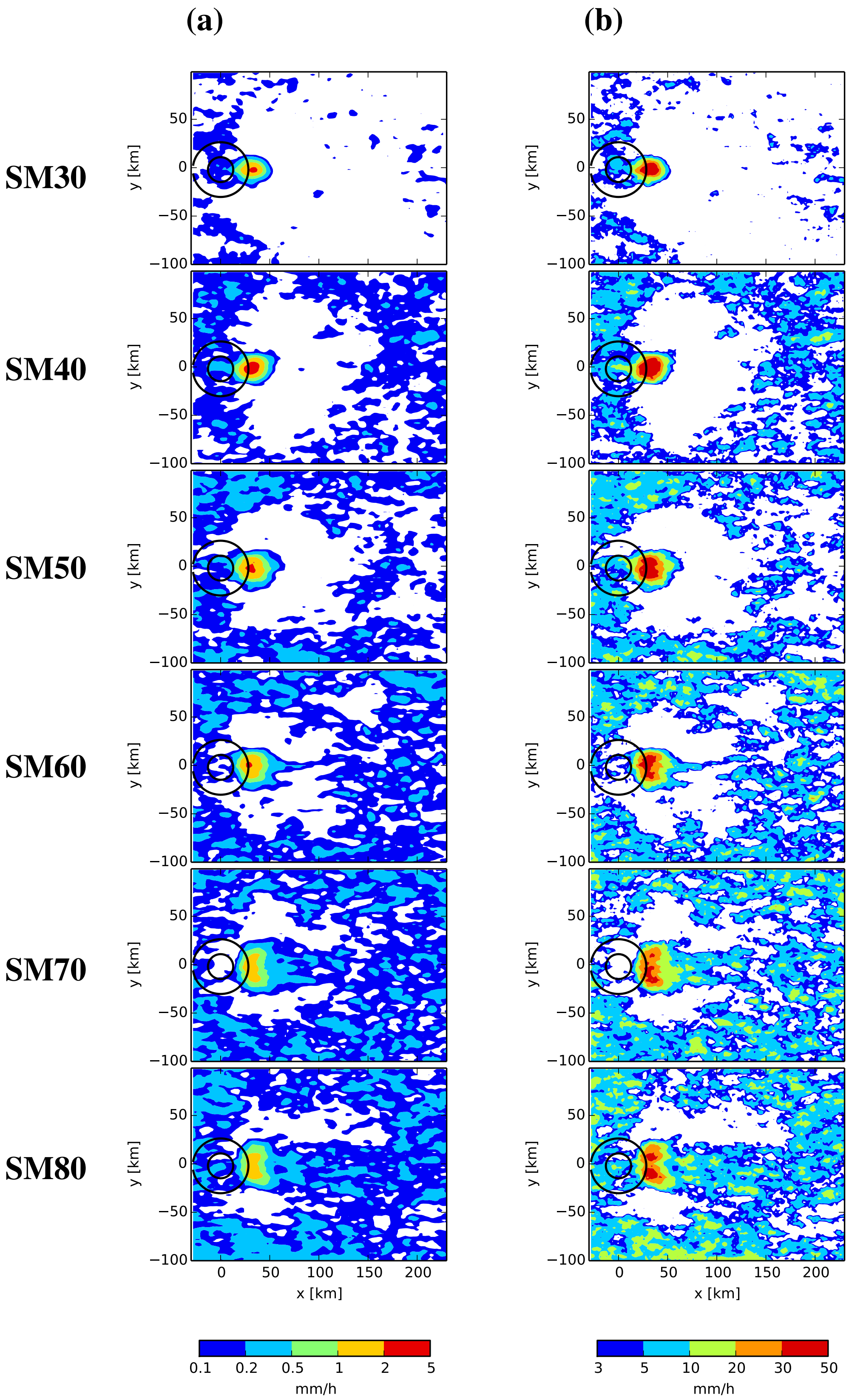

Figure 3.5: Horizontal view of the intensity of (a) the mean precipitation and (b) the 99th percentile. The 99th percentile is determined by taking into account 20 days and 48 output time-steps (accumulated precipitation every 30 minutes) for each day; top to bottom, SM30, SM40, SM50, SM60, SM70 and SM80. Black circles are the mountain contours at 250 and 750 m above the ground level.

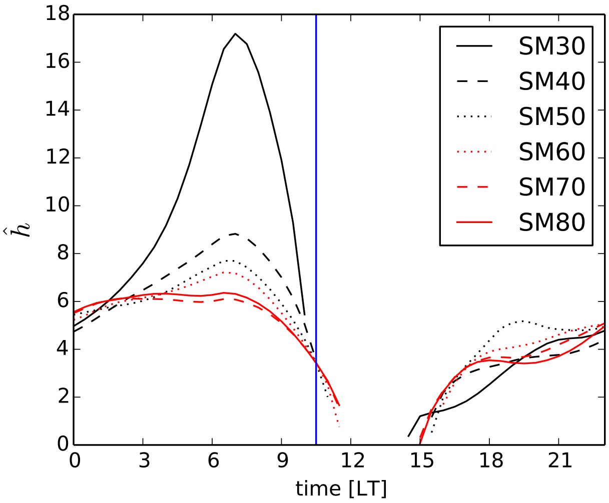

Figure 3.6: Mean area-averaged diurnal cycle of non-dimensional mountain height ($\hat{h} = NH/U$), where N and U are averaged between the lowest atmospheric layer and the mountain height, over FAR. For $\hat{h}$ <1, over-mountain flow is predominant and for $\hat{h}$ >1, around-mountain flow is mostly dominant. Values are suppressed for time periods with $N^2 < 0$.

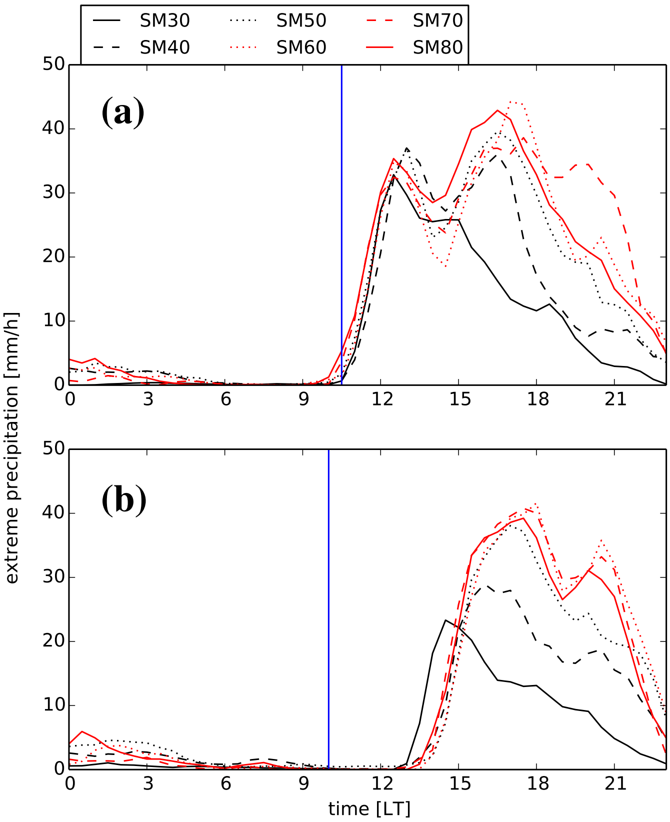

Figure 3.7: Diurnal cycle of the precipitation 99.9th percentile (Q99.9) over the 20 days and the region of interest, for (a) near field and (b) far field. The plots are for the SM set.

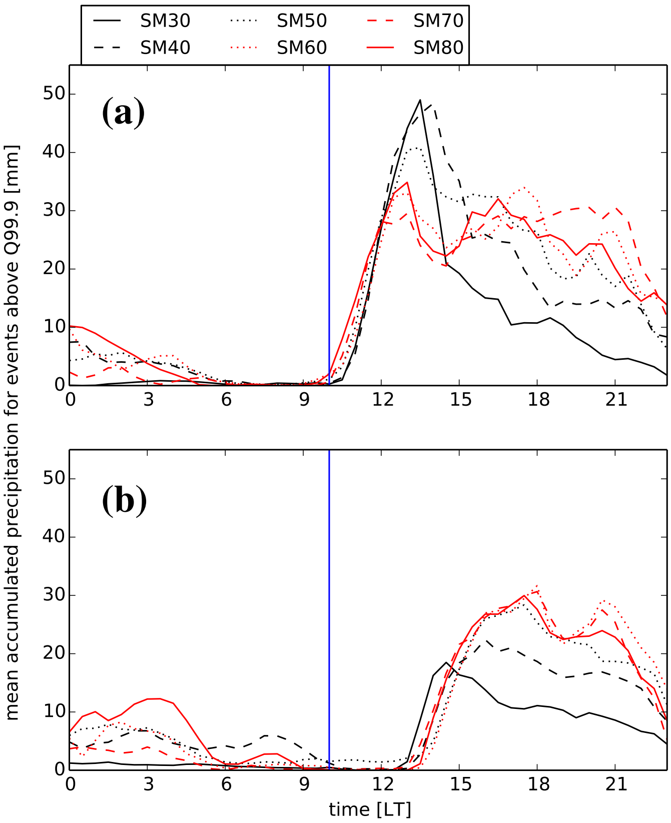

Figure 3.8: Diurnal cycle of the mean accumulated precipitation over GPs with precipitation > Q99.9 at that specific time of the diurnal cycle, over (a) near and (b) far field, for the SM set.

The duration of each event is computed with tracing back the event till the precipitation amount is smaller than 0.1 mm h^{-1}. Then we take the mean of all events. Although over the far field, the highest accumulation appears for moister cases very late afternoon, over the near field, the accumulated amount is larger for drier simulations in early afternoon.

As an estimation of the spatial extension and distribution of the intense precipitation, Fig. 3.9 presents the percentage of GPs in each field of interest with precipitation of more than 1, 10, 20 and 30 mm h^{-1}. As in the previous figures, for each time in the diurnal cycle, all the GPs at that time of the 20 days are considered. In terms of intensely-precipitated area, the late afternoon precipitation plays the role on moister simulations (Fig. 3.9c and d).

3.3.2 Impact of atmospheric stratification

The mean state

In the LR set, the BL profiles readjust themselves according to the equilibrium state conditions. For the lower lapse rates (e.g. LR4), the atmosphere is strongly stratified.

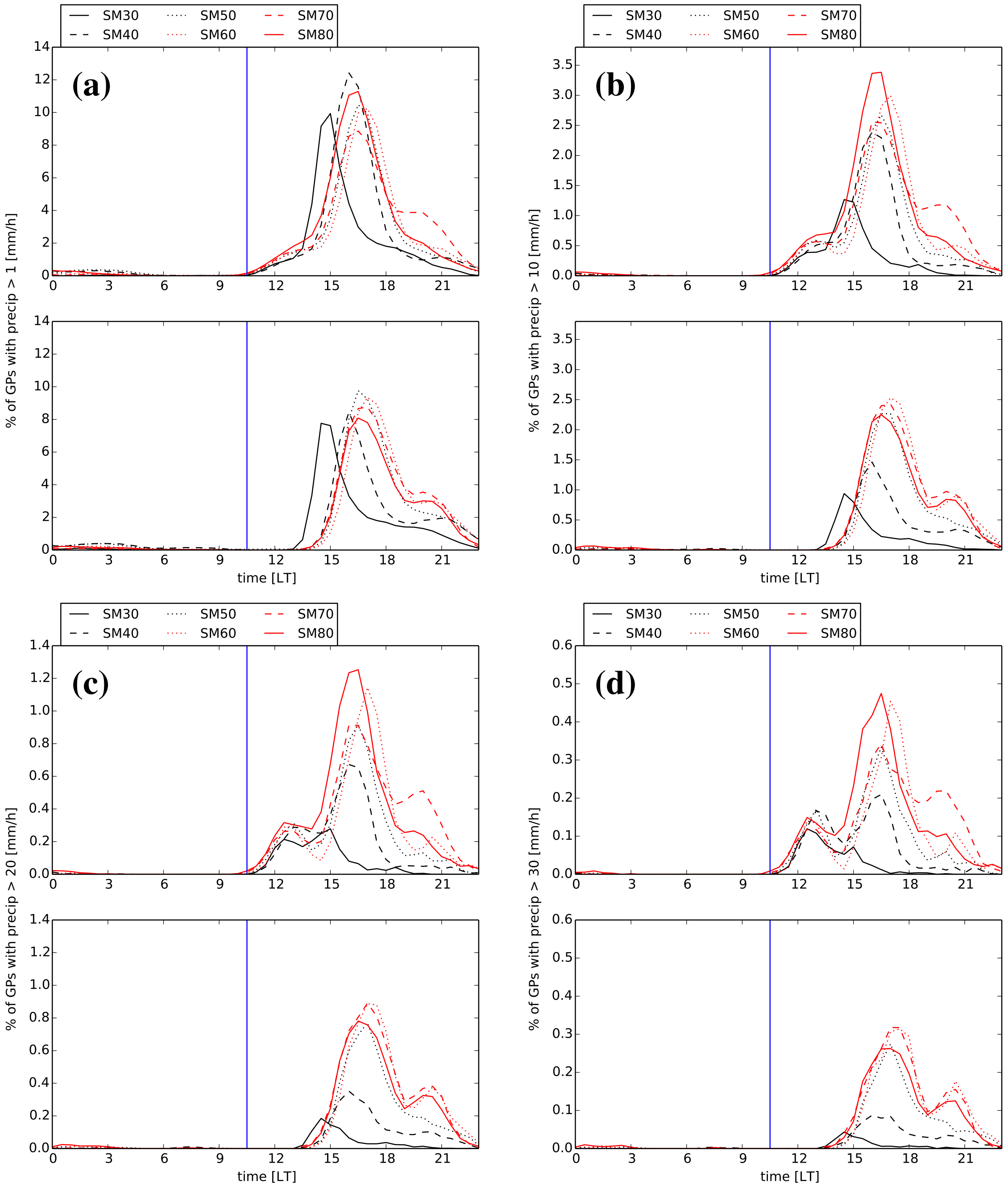

Figure 3.9: Diurnal cycle of the percentage of the GPs that receive a precipitation amount larger than (a) 1, (b) 10, (c) 20 and (d) 30 mm h^{-1} for each time in the diurnal cycle. In each frame, the upper panel is over the near field and the lower panel is over the far field for the SM set.

Therefore, the convective triggering is mostly suppressed and the vertical moisture transport is inefficient. Whereas, for the higher lapse rates the moisture is transported from lower BL to upper atmosphere through more active convection dynamics. For this reason, in the equilibrium state the BL is moister for lower LRs (Fig. 3.10). This is consistent with the findings of Schlemmer et al. (2011). Furthermore, the higher atmospheric moisture content decreases the outgoing longwave radiation and drives a warmer atmosphere in lower LRs (Schlemmer et al., 2011).

The diurnal cycle of area-mean precipitation over the 20 days is shown in Fig. 3.11a,b for near and far field. Over both fields, LR6 has the highest mean precipitation at 1500LT. The influence of the mountain is seen from the triggering of the primary precipitation over the near field. Moreover, the afternoon maximum over the far field is lower for unstable cases (LR7 and LR8).

The highest mean daily precipitation occurs for LR7 over near and far fields (Fig. 3.11c). However, the mean evaporation amount does not change remarkably, due to an almost constant latent heating for the LR set (Table 3.2).

Table 3.2: As Table 3.1, but for the LR set.

Surface heat fluxes	LR4	LR5	LR6	LR7	LR8
Net radiation	165.9	166.6	169.3	174.12	170.0
Latent heat	130.4	130.5	131.9	134.8	129.9
Sensible heat	25.6	28.4	32.1	35.6	38.5
Mean precipitation	2.16	2.50	3.04	3.16	3.03

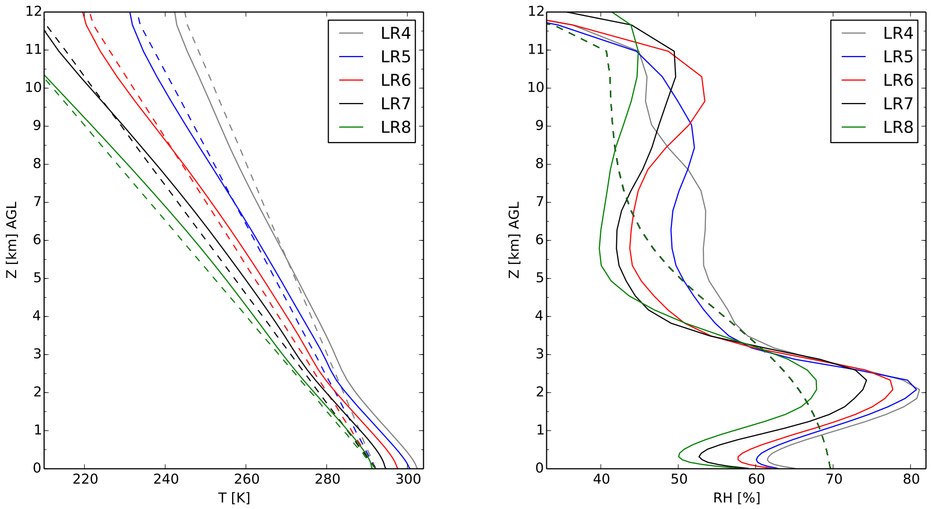

Figure 3.10: Initial (dashed lines) and equilibriated 20-day mean (solid lines) profiles of the atmospheric temperature (left) and relative humidity (right) within the troposphere over the far field for the LR set.

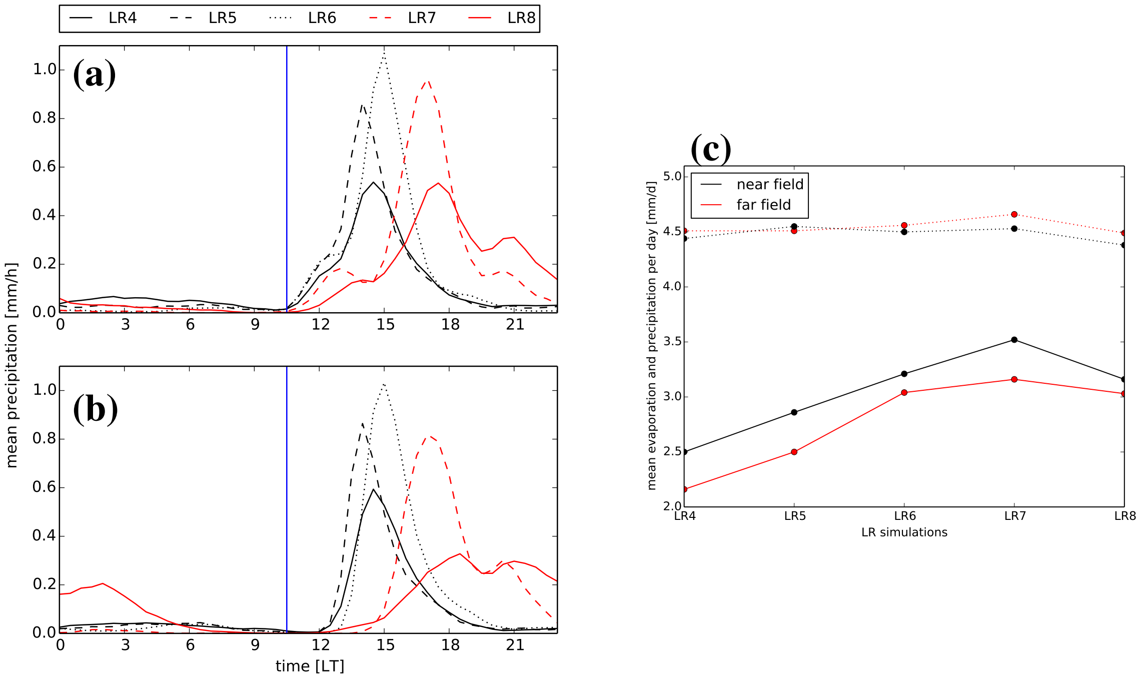

Figure 3.11: As Fig.3.4, but for the LR set.

The mean horizontal precipitation over the near field is seen in Fig. 3.12a. Over the flat part of the domain the precipitation patches are smaller for strongly stratified cases and larger for for weakly stratified cases which is in line with Schlemmer et al. (2012). Over the mountain vicinity the primary cold-pool effect is more evident for larger LRs, as will be discussed later.

Extreme precipitation characteristics

As discussed before, the atmosphere is drier for weakly-stratified cases. Therefore, the rain evaporates more efficiently and leads to stronger cold pools. In strongly-stratified cases, the atmosphere is moister and warmer and leads to extreme precipitation due to the lee convergence and BL growth. The results of these processes are seen in Fig. 3.12b. It shows the reduction of the lee precipitation intensity and the gradual emersion of the primary cold-pool effect over the near field going from LR4 to LR8. No systematic changes are found for the flow regime for this set of simulation.

The diurnal cycle of the extreme precipitation (Q99.9) over both the near and far field is shown in Fig. 3.13a and b. The foot print of the mountain is seen from the early precipitation over the near field, for all cases. Mountain precipitation amount is higher for strongly stratified simulations. Moreover, since relative humidity is high, falling precipitating evaporates inefficiently in more stratified cases, so that the cold-pool-related mechanisms are weaker. Oppositely, for the most unstable and dry case (LR8), the highest intense precipitation occurs from colliding cold-pool outflows in the evening.

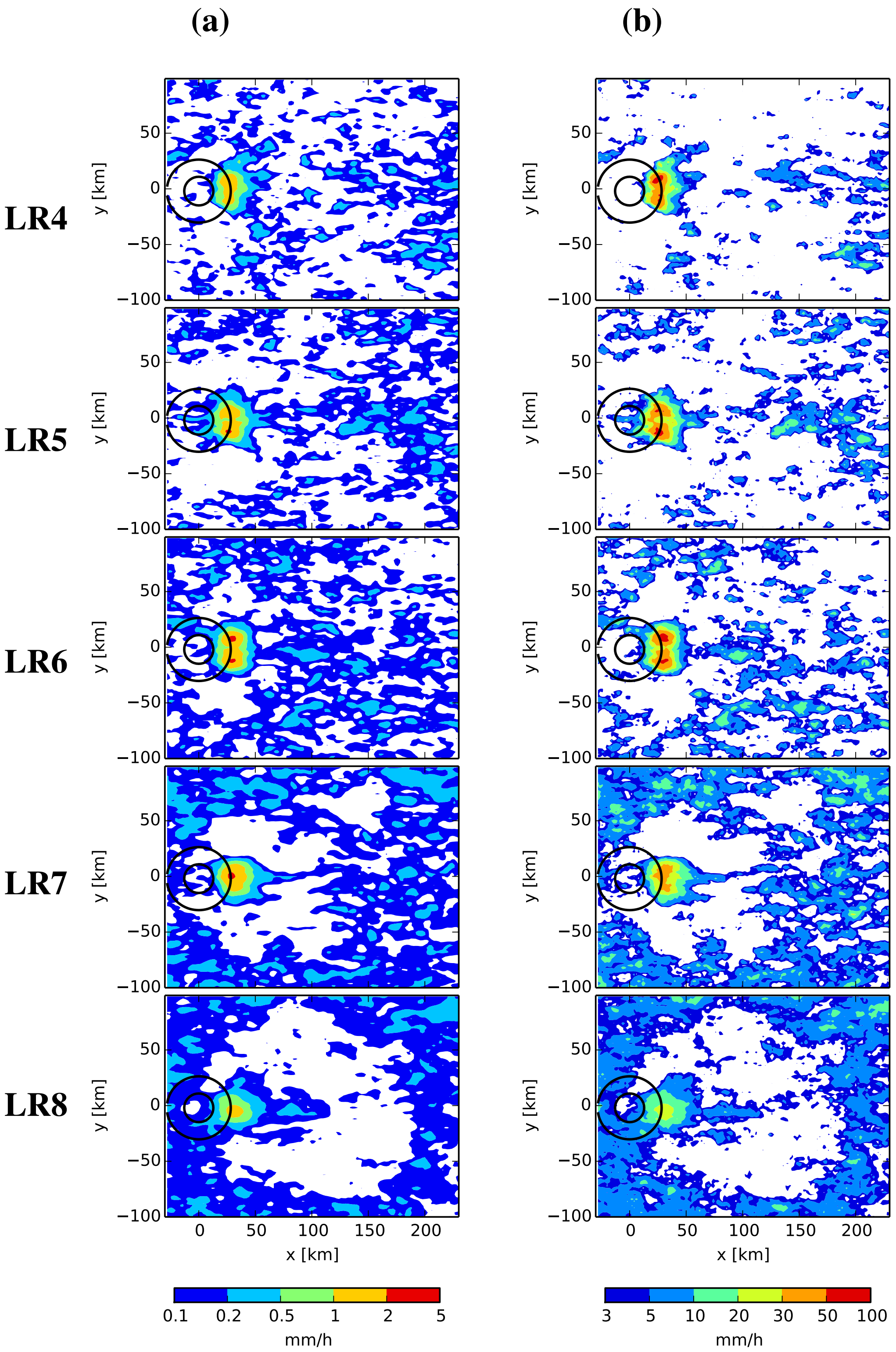

Figure 3.12: As Fig.3.5, but for the LR set (top to bottom, LR4, LR5, LR6, LR7 and LR8).

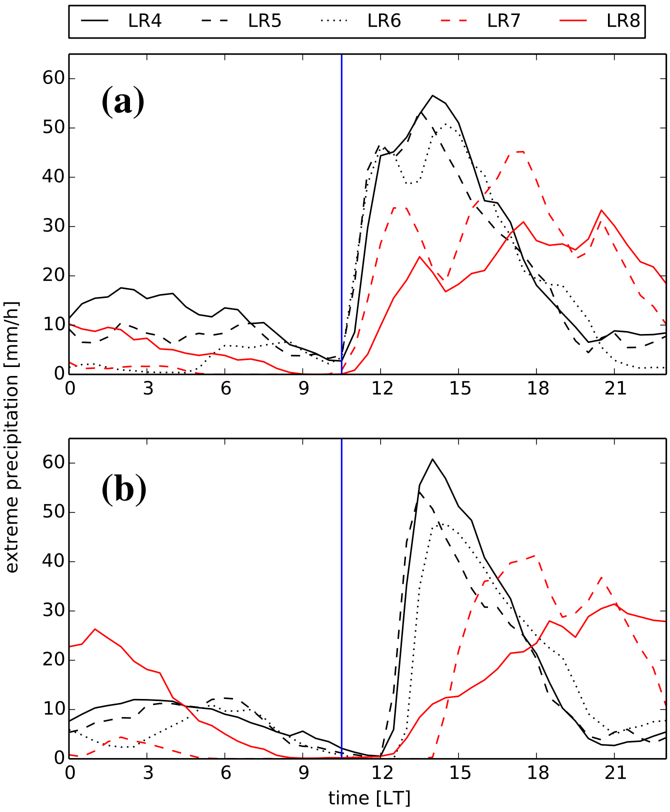

Figure 3.13: As Fig. 3.7, for the LR set.

Fig. 3.14 presents the diurnal cycle of the mean accumulated precipitation. A similar trend of increase is seen over the two fields. However, the mountain influence is clearly visible in the morning and at noon over the near field. In general, in the strongly-stratified simulations higher precipitation amounts can be accumulated over both fields. In terms of the area covered by the intense precipitation, near and far field show very little differences for morning and early afternoon precipitation events (Fig. 3.15).

To summarize, variations in lapse rate introduce two opposing effects on the precipitation intensity and accumulated amounts. For weakly-stratified cases (larger LRs), the atmosphere is drier that leads to stronger cold pools. Hence, the mechanisms related to the cold pools produce the most intense and highly accumulated precipitation during the diurnal cycle. On the other hand, for strongly-stratified cases (smaller LRs), due to the moister and warmer atmosphere, the cold pools are weaker and the most highly-accumulated precipitation is produced by the other mechanisms, i.e., the lee-convergence and the BL growth.

3.4 Conclusion

The influence of an isolated mountain on extreme precipitation is investigated for different environmental conditions, using simulations with different soil moisture contents and varied atmospheric stratifications. We evaluate the extreme events in terms of the extreme-precipitation accumulation.

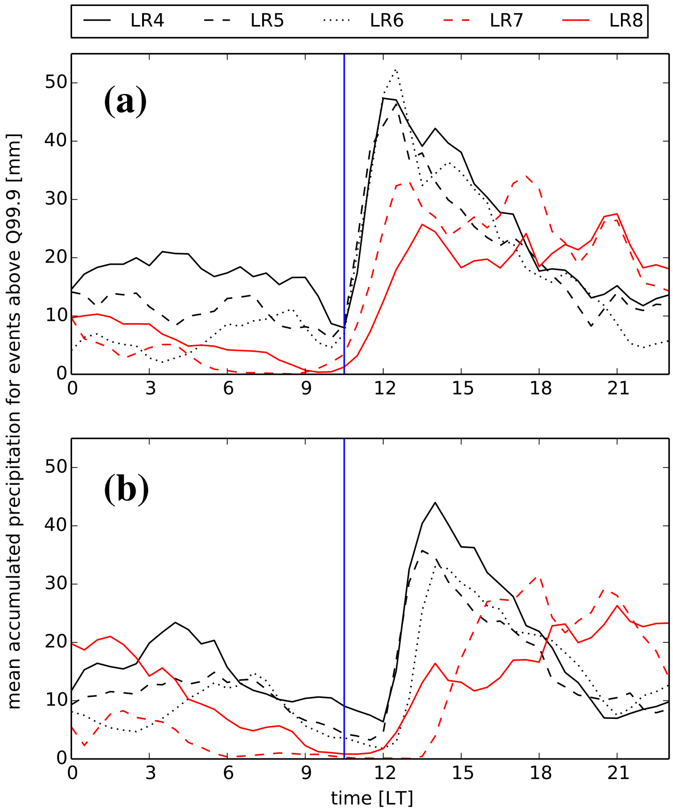

Figure 3.14: As Fig. 3.8, for the LR set.

Not surprisingly, within both simulation sets (SM and LR), some differences are seen for the timing and amount of the extreme precipitation due to the different environmental conditions. To investigate the influence of the presence of the mountain, the precipitation characteristics of the near and far field are compared to each other. It is found that, the dry soils amplify the role of the mountain in producing the extreme precipitation, provided that there is sufficient moisture to trigger the event.

Atmospheric stratification also influences the precipitation characteristics. Two opposing effects are seen in this set of simulations. Weakly stratified cases lead to dry conditions and thereby to efficient evaporation of precipitating water. Therefore, the cold pools are stronger and the mechanisms related to the cold pools produce highly-accumulated precipitation. For strongly stratified cases, the warm and moist atmosphere leads to higher precipitation amounts triggered by lee convergence and boundary layer growth. Altogether, the highest precipitation accumulation occurs in the afternoon for strongly stratified simulations, both over the near and far field. However, these changes are mainly thermodynamical effects of the atmosphere, rather than the influence of the mountain.

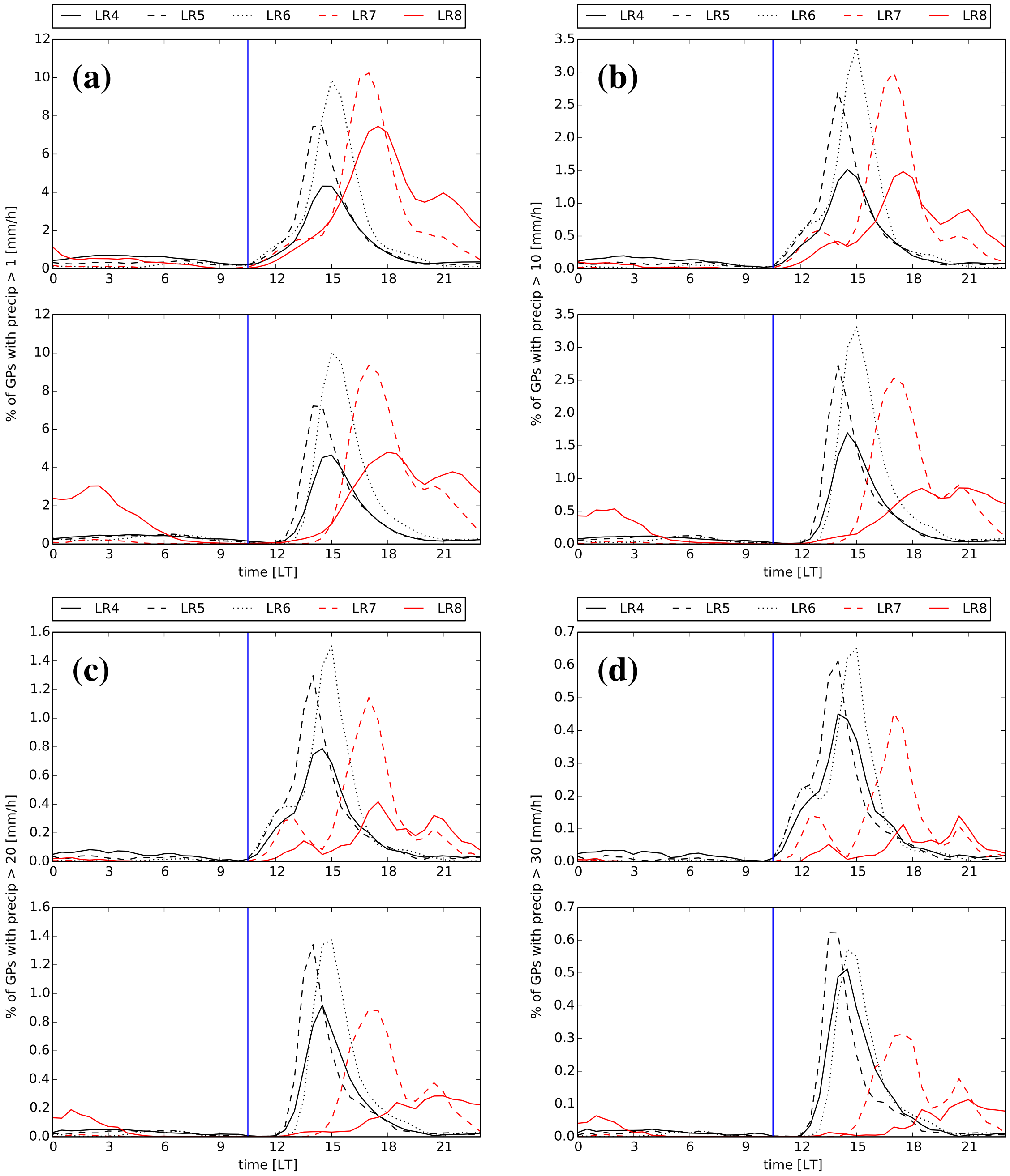

Figure 3.15: As Fig. 3.9, for the LR set.

Chapter 4

Conclusions and outlook

Conclusions and outlook

4.1 Conclusions

This thesis investigates the characteristics of summertime moist convection in the vicinity of isolated mountains and its sensitivity to mountain size and environmental conditions. We used an idealized setup, employed on COSMO-CLM (hereafter, CCLM) to run our simulations. We also benefited from a convection resolving modeling approach by applying a fine grid-resolution of 2 km (instead of parametrizing the deep convection). The simulations are run for 35 days. The large-scale forcing is represented by some relaxation towards an atmospheric profile. The relaxation is significant at upper levels but small near the surface, so that the boundary layer structure is largely determined by the physical processes. The simulations reach their equilibrium state after 15 days. We use the last 20 days as an ensemble of single-day simulations with slightly different initial conditions for each simulation.

The impact of an isolated mountain on summertime moist convection and the spatial distribution of precipitation is investigated in chapter 2. Our reference case includes a Gaussian-shaped mountain of 1000 m height and 20 km half-width. Four different mechanisms leading to the initiation of deep convection were identified over different parts of the domain and at different times of the diurnal cycle. After sunrise, mass convergence from thermal upslope flow and the background wind triggers intensive precipitation over the lee. Later, the cold pool caused by primary precipitation spreads over the mountain vicinity and leaves a dry area behind. Hence, this area gets merely very little precipitation, along the leading edge of the cold pool. In the afternoon, boundary-layer growth leads to convection initiation and some precipitation. The collisions of outflows from previous precipitation events produce more convective cells and precipitation in the evening. These processes lead to a large contrast in mean precipitation as accumulated in different areas of the domain. The mountain lee gets almost 7.5 times more precipitation than the domain average, while the flanking area gets only 0.25 times of domain-average precipitation. The region far away from the mountain shows precipitation activity characteristic of a simulation without topography.

A very strong temporal and spatial sensitivity is found to the mountain size. Comparing different mountain heights, the precipitation onset is earlier for the higher mountains, leading to more frequent precipitation over the lee. For a mountain of given height, the precipitation is more intense in the vicinity of mountains with larger half-width. In addition, for higher mountains, precipitation intensity over the lee has spatially a double maxima, but for lower mountains, it has a single-maximum. These patterns are caused by different flow regimes for different mountain heights. For higher mountains, the flow goes predominantly around the mountain and usually two groups of cells are triggered over the lee, resulting in precipitation double-maxima. However, for lower mountains, the flow goes predominantly over the mountain and usually one group of cells is triggered over the lee. Thus, a single-maxima is produced for the precipitation intensity.

In the third chapter, we investigated the influence of an isolated mountain on producing heavy and extreme precipitation in different environmental conditions. Sensitivity studies are conducted with respect to the soil moisture content and atmospheric stratification. We found that, the mountain presence strongly increases extreme and accumulated precipitation in cases with lower soil moisture content. With dry surfaces, a larger fraction of the surface radiation balance is invested into diurnal circulations, which in turn are crucial for the initiation of convection. For the simulations with different stratifications, two opposing effects on extreme precipitation events are found. In strongly-stratified cases, the boundary-layer moisture is not transferred efficiently to higher levels, hence the boundary layer is moister. The moister boundary layer intensifies the precipitation of the lee-convergence (mountain effect) and the boundary-layer growth mechanisms. However, weakly-stratified cases lead to drier condition and (consequently) an efficient evaporation of the falling-precipitation which results in stronger cold-pools. Hence, for the weakly-stratified cases, the intensified precipitation strongly depends upon the cold-pool related mechanisms; e.g. the primary cold-pool in the afternoon (mountain effect) and colliding cold-pools in the evening.

Overall, lee-convergence and primary cold-pool processes are the two robust convection initiation mechanisms seen over the mountain near-field in all simulations. The precipitation onset is earlier over topography. In addition, very intense and frequent precipitation is subjected to occur over the mountain vicinity that may cause flood risk potential. However, the timing and intensity of the orographic precipitation depends critically on environmental and topographical properties. The current idealized setup is a powerful framework to investigate the features of the summertime deep convection.

4.2 Outlook

Bellow, we summarize some future work, that would help us to understand more of the convection initiation and precipitation processes.

- The lee convergence line appears to be a robust feature in all of the simulations, which triggered the mountain precipitation in the morning. This line is generated due to mass convergence from the thermal upslope flow and the background wind. The timing and location of the early precipitation strongly depends on the strength of these two flows and also on the mountain flow regime. Although we touched this topic briefly in this thesis, a better understanding of the interaction of the background and upslope flow would be of interest. To this end, one could change the strength of the upslope flow by varying the thermal forcing (still in summertime range). For the background flow, the strength can be changed by varying the initial wind profile (which also changes the flow regime).

- The second important process which influences the mountain precipitation is the cold pool generated by the primary convective precipitation. Our investigation showed that the environmental conditions influence the strength of the cold pool, and thereby the extreme precipitation values. In addition, the interaction of the cold-pool with the mountain (whether it can pass the mountain peak towards upstream) is also important. Two factors proposed as the key elements, the slope of the mountain and the wind direction in respect to an (elliptical) mountain axis. We suggest two more detailed investigations on the cold-pool evolution in different environmental and topographical conditions.

    1. Applying different environmental conditions in combination with different mountain sizes. This study may help us to understand whether the slope, the volume or the height of the mountain plays the most important role on pool-mountain interaction in different atmospheric conditions.

    2. The other investigation should be more focused on the impact of wind shear and wind speed on the propagation of the cold-pool leading edges in different directions.

- A key parameter that significantly influences boundary layer processes is the soil moisture impact on the surface fluxes. As discussed before, we did not use an interactive soil moisture in our setup, as the conceptual framework for such a coupling appears challenging. This may influence the dynamics of the upslope flow and cold-pool during and after precipitation events. It would be useful to perform the simulations with an interactive soil moisture for a more accurate boundary layer processes, for instance by using a lateral runoff scheme.

- We can also apply stronger wind shear through initial condition of the wind profile as a favorable environment to develop organized convection types such as squall lines and supercells. It would be of interest to investigate the role of the topographic convection in generationg or further development of such organizations and also the effect of such wind profiles on the precipitation distribution over the domain.

- The idealized framework could be used to investigate the effects of the climate change. The objective would be, to study how deep convection initiation and precipitation processes may change in a warming climate, and how this effects extreme precipitation over mountainous regions. This can be done by applying different initial temperature profiles according to different scenarios of warming climate. The idealized framework is always an asset for easier interpretation of the results for a warming climate.
- Further work to improve numerical presentation of smaller-scale boundary layer processes could include large eddy simulation (LES) approach (available in CCLM5.0). LES captures boundary layer turbulent processes more accurately by resolving larger eddies in the boundary layer. It is very interesting to see the influence of the LES models on the timing of the convective triggering. Consequently, this setup would be more reliable in explicitly resolving clouds through shallow convection and then their transformation to deep convection. However, applying LES is not yet affordable for many applications due to the higher computational cost.

Appendix A

Influence of the size of topography on the diurnal cycle of summertime precipitation over circular mountains

Appendix A

Influence of the size of topography on the diurnal cycle of summertime precipitation over circular mountains

In this Appendix, we investigate the effect of the half-width and height of a circular mountain on the frequency and intensity of the mean and extreme precipitation. Previous analyses indicate that the presence of a mountain influences the triggering of convection and the spatial distribution of precipitation, remarkably. The mountain existence is essential for the early convection initiation and the successive development of the secondary convection along the leading edge of the primary cold-pool. It also changes the diurnal cycle of the moisture and temperature over the mountain near field. Apparently, the same precipitation pattern cannot be seen over a flat terrain. In this regard, it is also expected to have temporal and spatial differences for precipitation over mountains with different sizes. Previously, Barthlott and Kirshbaum (2013) investigated the triggering and evolution of deep convection developing over the islands of Corsica and Sardinia for their actual height and idealized varying heights, including a flat terrain. They showed that the mountain height is an important factor in the timing of the primary precipitation.

To investigate the impact of the mountain geometry on the development of clouds and precipitation, we perform nine simulations with a combination of 3 different mountain heights (500, 1000 and 2000 m) and 3 mountain half-widths (10, 20 and 40 km). Since each mountain is characterized by its half-width A, and height H, the case with a mountain of 40 km half-width and 500 m height is referred to as A40H500, for instance. A flat terrain simulation (Flat) is also performed as a representation for the far field for all the nine simulations. COSMO-CLM 4.28 is used to run the simulations and the model set up and the initial and boundary conditions are identical to the control simulation in chapter 2. The simulations are run for 35 days and the last 20 days are taken as the equilibrium phase (see chapter 2).

A.1 Precipitation frequency and intensity

Fig. A.1 shows the spatial distribution of precipitation in terms of mean frequency and intensity of hourly precipitation. The maximum frequency increases with increasing mountain height (Fig. A.2a), owing to the earlier onset of precipitation over the lee of higher mountains (see section 2.3.5). One also should consider that the precipitation termination time is almost identical for these cases. The area with higher precipitation frequency (>4 h/d) is also enlarged with height. The maximum intensity increases with increasing mountain half-width (Fig. A.2b). The exception is A40H500, for which the slope of the mountain is so small that the primary cold-pool can easily overcome the mountain height and move upstream.

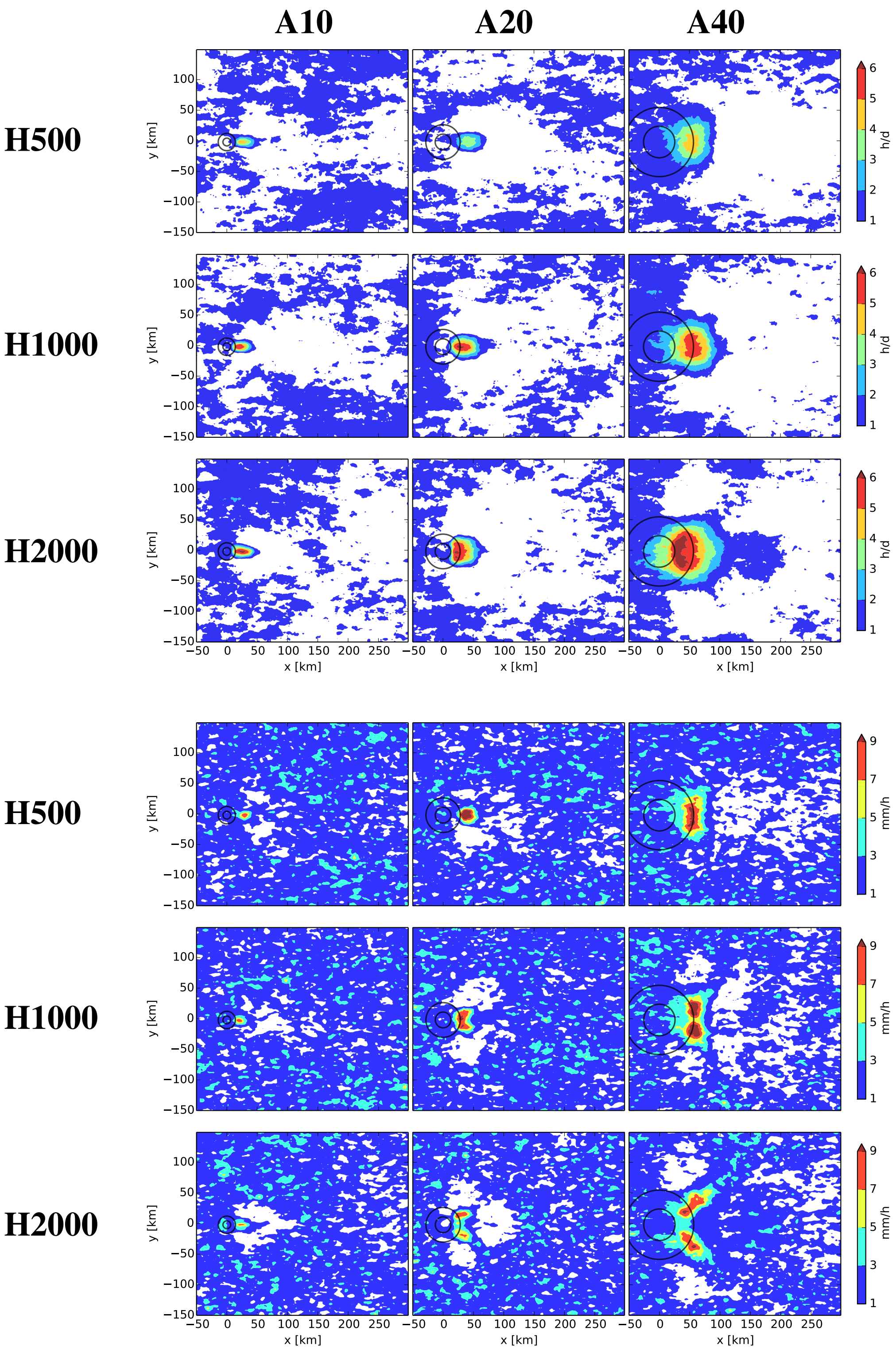

Figure A.1: Mean surface precipitation frequency (upper panel) and intensity (lower panel) for different mountain sizes. Frequency is defined as the number of wet hours (precipitation > 0.1 mm/h) per day, and intensity is the mean precipitation over the wet hours, averaged over equilibrium time. Mountain half-width increases from left to right (10, 20 and 40 km) and mountain height increases from top to bottom (500, 1000 and 2000 m). The black circles are the mountain cross-sections at one- and three-forth of the mountain height from the ground.

Since the convective clouds also move along the leading-edge of the cold-pool and the cells are not continuously produced over the mountain lee, the lee precipitation can not intensify for this case. An almost linear increment is seen for the area covered by the intense precipitation (intensity>5 mm/h).

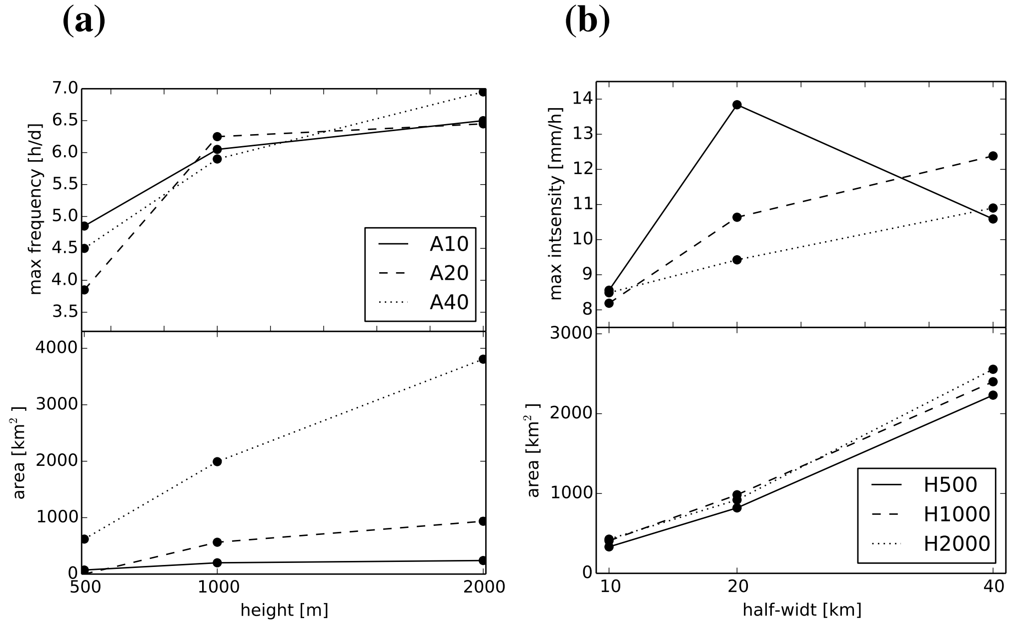

Figure A.2: Variation of maximum averaged precipitation frequency (top left) and maximum averaged precipitation intensity (top right) with mountain height and half-width, respectively, over the 20 days. Lower panels show the variation of the area with frequent (>4 h/d) and intense (>5 mm/h) precipitation with mountain height and half-width, respectively. The statistics are based on the grid point values in Fig. A.1.

Moreover, the shape of the area with intense precipitation depends on the flow regime. The flow regime defines whether the impinging air goes around or over the mountain. For the higher mountain, the flow goes around the mountain and two distinct primary convective cells are generated over the lee (see chapter 2). Therefore, the precipitation intensity has double maxima. For the lower mountains, the flow goes over the mountain and the background flow and lee upslope flow converge over the lee and in most of the days one group of early convection is triggered in the beginning, hence the precipitation intensity has a single maximum. Here, the governing regime is the regime which exist at the time of precipitation onset, since the most intense precipitation occurs in the first hours after the precipitation starts. Precipitation set in around 12, 11 and 10 local time, for cases with H500, H1000 and H2000, respectively (see bellow). Fig. A.3 shows the diurnal cycle of the non-dimensional mountain height ($\hat{h}$) as a representative of the flow regime. For the higher mountains, $\hat{h}$ remains larger than 1 throughout the diurnal cycle. This indicates that the around-the-mountain flow is dominant, which is the reason for the double maxima in the lee. When $\hat{h}$ is less than or equal to 1, the over-the-mountain flow is dominant, resulting in a single maximum.

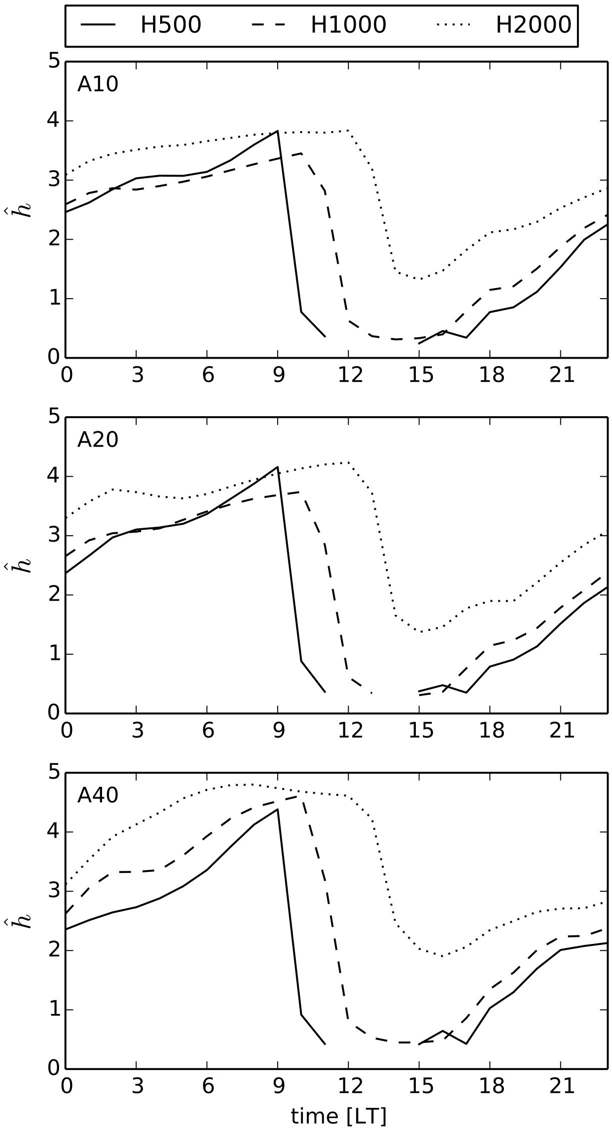

Figure A.3: Mean diurnal cycle of the non-dimensional mountain height ($\hat{h}$ = NH/U), where N is the static stability and U is the zonal wind, both averaged over the far field and at the height H. Values are suppressed for time periods with $N^2 < 0$.

A.2 Extreme precipitation

Here, as a measure of extreme precipitation, we take the 99.99th percentile (Q99.99) of hourly precipitation of all grid points and all 20 days at a specified time of the day. Fig. A.4 shows the diurnal cycle of Q99.99. First of all, it is seen that for each particular height, the maximum diurnal precipitation extreme increases with the half-width increase. One reason could be an increase of the amount of air being lifted by background flow and the amount of upslope flow triggered over larger lee area, for the wider mountains. Secondly, the onset of the precipitation is one hour earlier for each increase in mountain height.

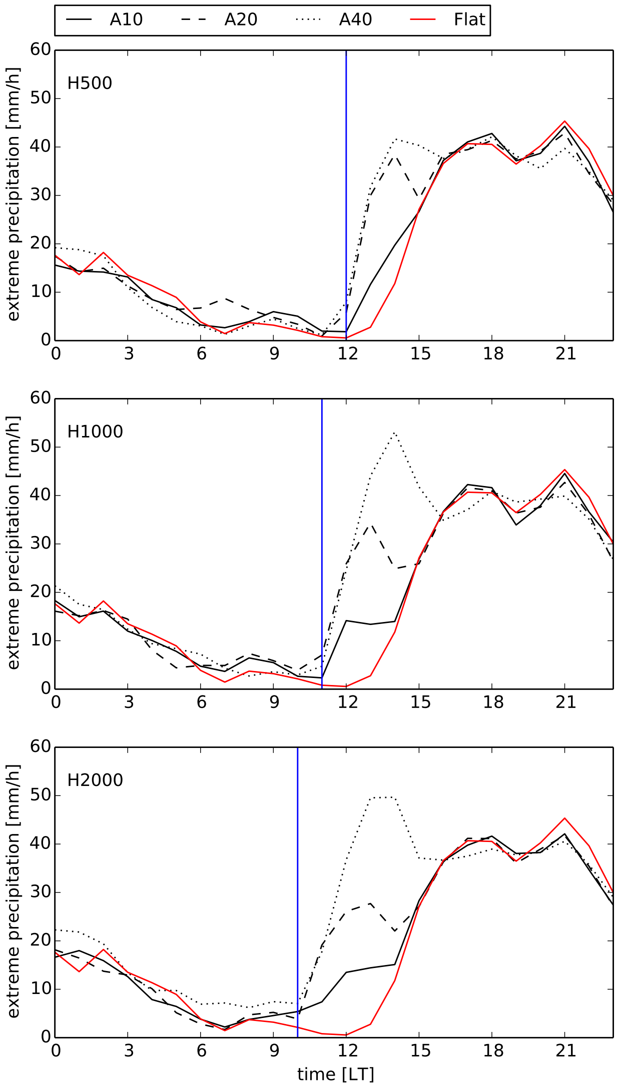

Figure A.4: Diurnal cycle of the 99.99th percentile of the hourly precipitation (Q99.99) over the 20 days and the whole domain. The blue lines roughly indicate the time of precipitation onset.

Fig. A.5 shows the accumulated precipitation of extreme events. This parameter is defined as in Fig. 3.8. The same trend of extreme precipitation amount is seen for extreme precipitation accumulation. It is worth to add that for A40H500, there is small/no increase in the figures due to the upstream movement of the primary cold-pool (as discussed earlier).

For the simulations with topography, the late afternoon and evening precipitation occurs mostly due to the convection from the boundary-layer growth and the collision of the active cold pools which are also active in the Flat simulation. Therefore as seen from the Fig. A.4 and Fig. A.5, the amounts of the extreme precipitation and accumulated precipitation of the extreme values is almost the same after 1600LT for all the simulations including Flat.

A.3 Summary

The mountain size is an important factor in defining the timing and spatial distribution of precipitation. The height and the half-width of the mountain influence the precipitation events in different ways. The mountain height mostly effects the timing of the precipitation. For the higher mountain, the lee precipitation starts earlier. However, the mountain half-width has a strong influence on the amount of the intense and extreme precipitation. The wider the mountain is, the larger the extreme values get. This is valid for the simulations in which the slope of the mountain is large enough to prevent the primary cold-pool from moving upstream.

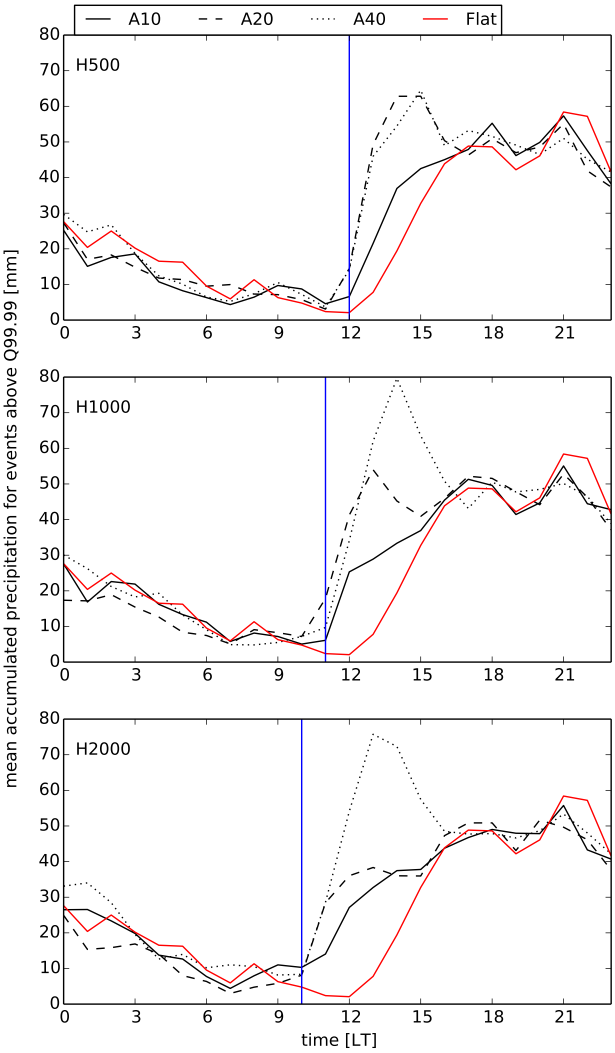

Figure A.5: Diurnal cycle of the mean accumulated precipitation over grid points with precipitation>Q99.99 at that specific time of the diurnal cycle. The blue lines roughly indicate the time of precipitation onset.

Appendix B

Influence of the wind direction on the evolution of convective storms and intense precipitation over an elliptical mountain

Appendix B

Influence of the wind direction on the evolution of convective storms and intense precipitation over an elliptical mountain

In appendix A we studied the influence of the geometry of a circular mountain on intense precipitation. In this appendix, we investigate the influence of an elliptical mountain on convective initiation and resulting precipitation patterns. For an elliptical mountain, two new factors are important: the ratio of the mountain long- to short-half-width ($\beta = A_l/A_s$) and the background wind orientation with respect to the mountain long axis (Galewsky, 2008; Soderholm et al., 2014). Our goal is to study the impact of the wind direction on convective cells evolution and extreme precipitation. Thus, β is kept constant with A_l=40 km and A_s=10 km.

We use the same model and setup as in chapter 2, but with a different specification for the topography:

$$h(x,y) = He^{-(\frac{x}{A_l})^2+(\frac{y}{A_s})^2} \tag{B.1}$$

where H is the height of the mountain which is set to 1000 m in current study. The mountain profile is defined such that the volume of the elliptical mountain is equal to that of the circular mountain using $A = 20$ km and $H = 1000$ m in appendix A. We perform five simulations with the same mountain profile, but different orientations with respect to the zonal wind direction (see Fig. B.1). The background wind flow is always from the left to the right. We denote the angle between the x-axis and long axis of the mountain with α. α is set to 0, 22.5, 45, 67.5 and 90 degree and the cases are named α0, α22.5, α45, α67.5, and α90, respectively. The simulations are run for 35 days and we take the last 20 days as the equilibrium phase. We consider the mean state as well as the whole time series of the 20 days. An extra simulation (FLAT) is also performed with no mountain as a representation for the far field.

B.1 Mean state

The mountain orientation with respect to the background wind changes the flow pattern and the area of lee-side convergence. Hence, the triggering locations of the primary cells are different for different simulations. Fig. B.1 shows the flow and surface precipitation averaged over the 20 days in equilibrium at 1200LT (after the primary cells are triggered) and at 1600LT (after the secondary convection is developed). The cold pool (as seen by the wind field) moves towards mountain upstream for smaller αs. The smaller α is, the faster the cold-pool moves upstream and the slower they move to downstream. For larger α, the speed of the cold pool decreases towards upstream (stagnant for α90) and increases towards downstream.

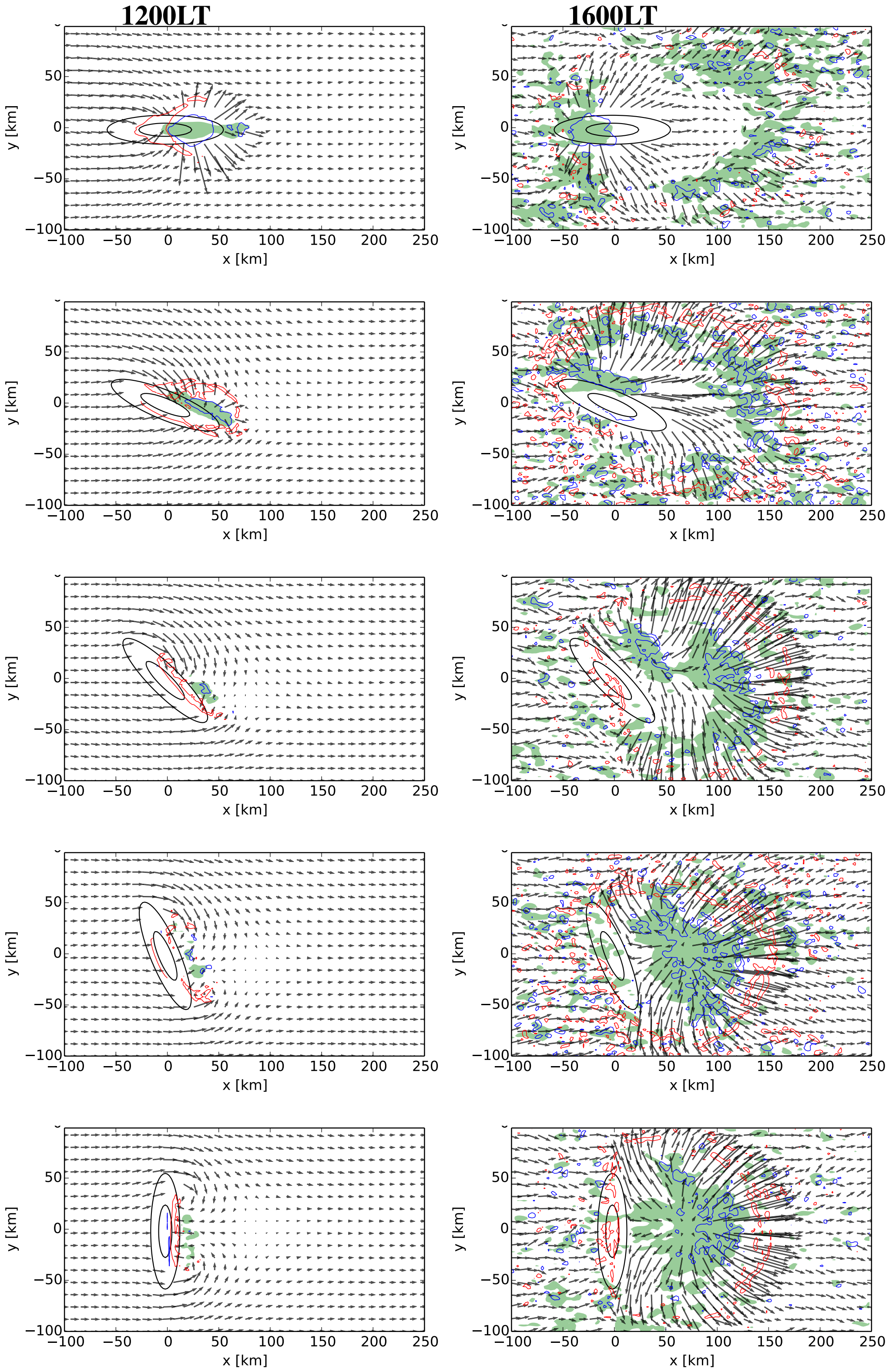

Figure B.1: Mean horizontal cross section of wind vectors at 250 m AGL, topography (black contours in 250 and 750 m AGL), accumulated surface precipitation of the last hour (green shading, 1 mm h^{-1}) and vertical wind at 750 m AGL (upward motion in red and downward motion in blue contours with the amounts of 0.2 and -0.2 m s^{-1}), for α0, α22.5, α45, α67.5, and α90, respectively from top to bottom, of 1200LT (left) and 1600LT (right).

Since, the convective cells move along the leading-edge of the cold pools, they move faster for larger αs and cannot produce higher amount of precipitation intensity and accumulation, compared to smaller αs (Fig. B.2). In addition, the precipitation pattern is more symmetric for $\alpha 0$ and $\alpha 90$, due to the symmetric situation of the mountain profile with respect to the zonal wind that leads to more symmetric convection triggering over the two sides of the mountain.

B.2 Evolution of the convective cells

In the previous section we hypothesized that due to the slope of the mountain towards upstream, the cold pool/secondary cells move downstream slower for smaller α (lower slopes) and faster for larger α. So that we could explain the mean precipitation distribution and amount for different cases.

To validate the hypothesis discussed above, we need to study the behavior of the precipitating cells in terms if their longevity and the distance they travel over the mountain vicinity. This can be done by tracing the individual storm cells from their origin over the mountain. We perform an algorithm to recognize and follow the precipitating cells over time in a region encompassing the mountain within x=[-50, 150] and y=[-50, 50] (see Fig. B.2). The algorithm is similar to Soderholm et al. (2014) and works as follows. A cell is defined as a region of connected points where the column maximum precipitation rate (MPR) exeeds a threshold of 12 mm/h. We consider only patches larger than 8 km^2 (2 grid points). When two consecutive cells overlap, the identification of the former cell is passed to the latter one. A new ID is allotted for a cell which is not overlapping with previous cells, and it is assumed as a new cell. The cell location is equal to the MPR-weighted mean. A minimum height of 4.5 km is considered for deep convection. In the case of cell splitting/merging, the history of the previous cell/s is assigned to the resulting cells; i.e. the track length and duration are traced back to the original event-generating cell(s). Merging is the overlap of two previously-distinct cells and splitting is the opposite. The algorithm is applied for the time interval of 1000-1800LT each day. For each of the five simulations, we considered 5 days (day 21-25) with data frequency of 5 min. The time resolution is found to be enough to trace a typical cell moving in a background flow of 6 m/s (estimated speed at 600-500 hPa height). This implies that if in 5 min a cell moves with a speed of 6 m/s, it travels 1.8 km which is still in the range of grid-cell dimension. Therefore, the continuous movement of a cell can be traced, to a good approximation. Fig. B.3 presents the duration versus track length of each detected cell for the five days of the study. The black lines are linear regression for each individual day. In general for each case, the longer the cells live, the larger the distance they travel. Among different cases, the cell tracks are longer for larger αs. As discussed earlier, the reason could be that, for larger αs, the cold-pool edges travel faster towards downstream (and in longer distances), and so do the cells which are triggered along cold-pools leading-edge. The opposite occurs for smaller αs.

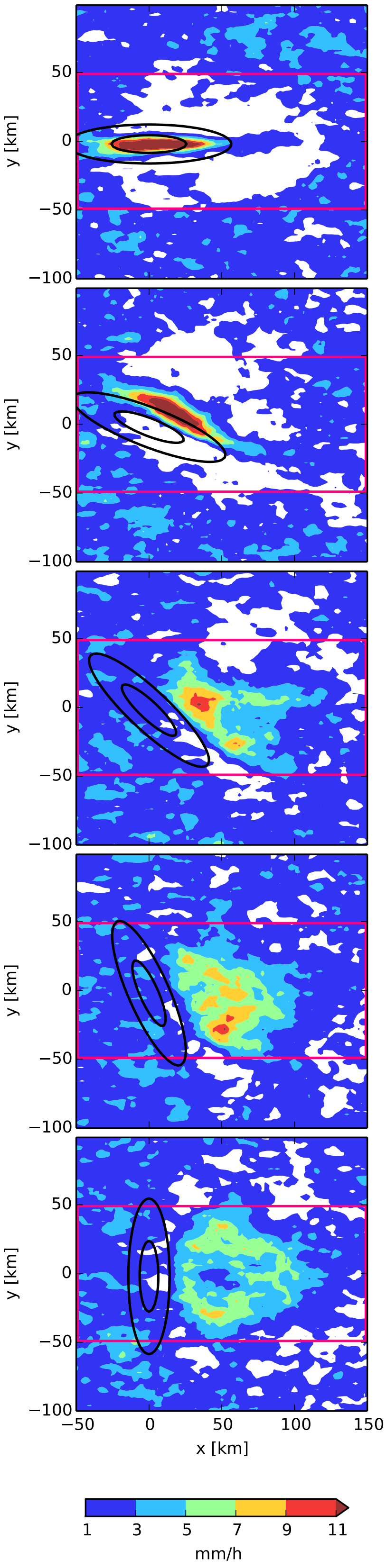

Figure B.2: Mean surface precipitation intensity; top to bottom: $\alpha 0$, $\alpha 22.5$, $\alpha 45$, $\alpha 67.5$, and $\alpha 90$. Intensity is defined as the mean precipitation over the wet-hours (precipitation > 0.1 mm/h). The purple rectangles show the part of the domain, where the cell-tracking algorithm is applied.

Soderholm et al. (2014) applied the same algorithm on a 10-yr climatology data over Black Hills. They found that the vertical wind profile enforces more control over cell evolution than thermodynamic profiles. The quasi-stationary cells which carry flash-flooding potential are the ones with short-track and long-duration traveling (STLD). STLD events are mostly initiated in a low-level wind paralleling the long axis of the ridge and a high-level wind crossing the ridge. Therefore, the convection triggers over the ridge from converging upslope and background flow. This way, cells precipitate over the downwind side, without suppressing a repeated cell generation by the precipitation outflow over the ridge.

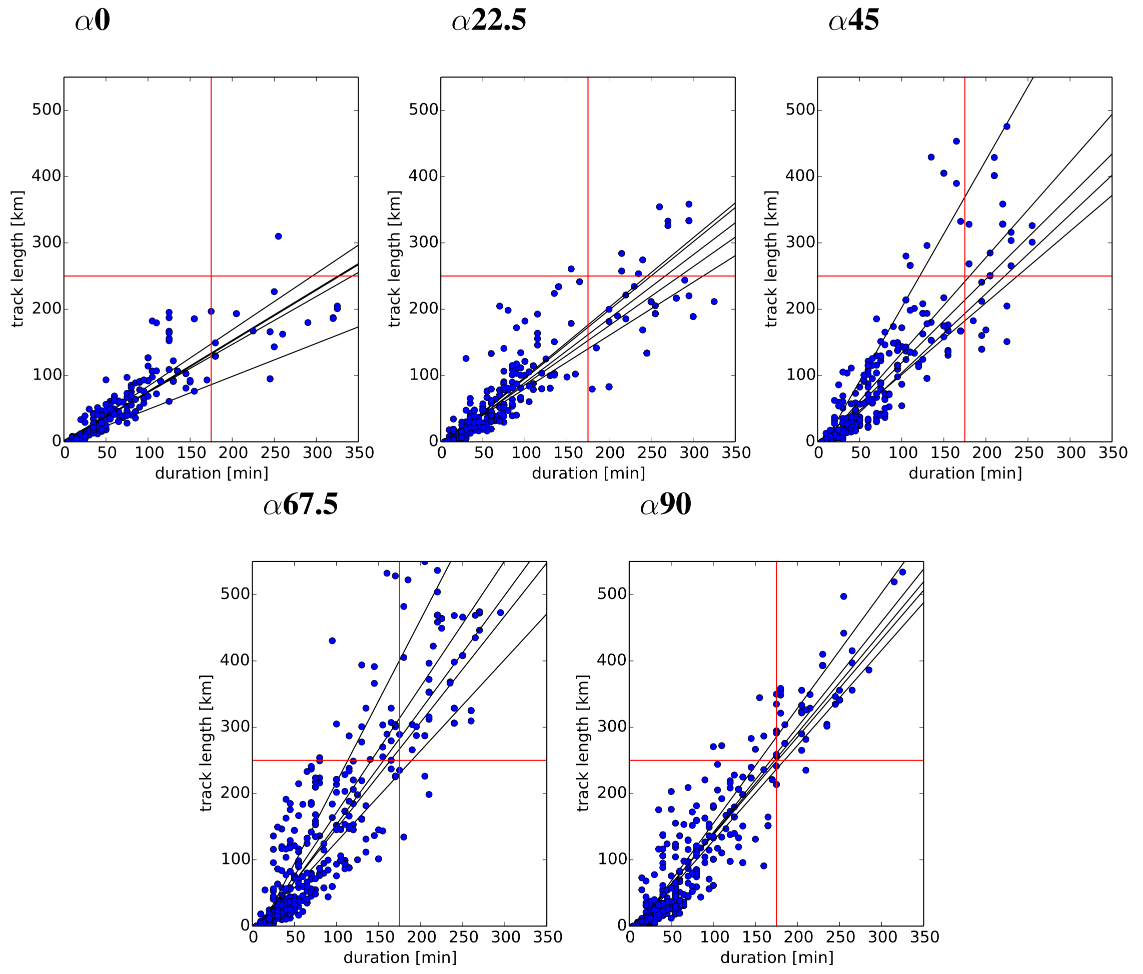

α**0** α**22.5** α**45**

α**67.5** α**90**

Figure B.3: Duration versus track length of each detected cells for all the investigated days. The black lines are linear regressions for each individual day. The red lines are for better visualization and comparison.

B.3 Extreme precipitation

As in appendix A, the 99.99th percentile of precipitation is used as a measure for precipitation extremes. Fig. B.4a shows the diurnal cycle of the 99.99th percentile of precipitation intensity (Q99.99) over the whole domain and at each diurnal hour for the 20 days. The influence of the topography is evident comparing FLAT with the rest of the simulations, for both the onset and the amount of the intense precipitation. Also for the simulations with topography, the onset of extreme precipitation is earlier. For smaller α, the diurnal maximum extreme precipitation is higher. For α67.5 and α90, the profiles remain almost identical. As expected for all the simulations, the afternoon (caused by the boundary-layer growth) and the evening (caused by the cold-pool collision) extreme precipitation are very similar. Almost the same pattern is seen for the mean accumulated precipitation over the grid points with precipitation larger than Q99.99 (Fig. B.4b). The reason for higher precipitation intensity and accumulation was discussed earlier.

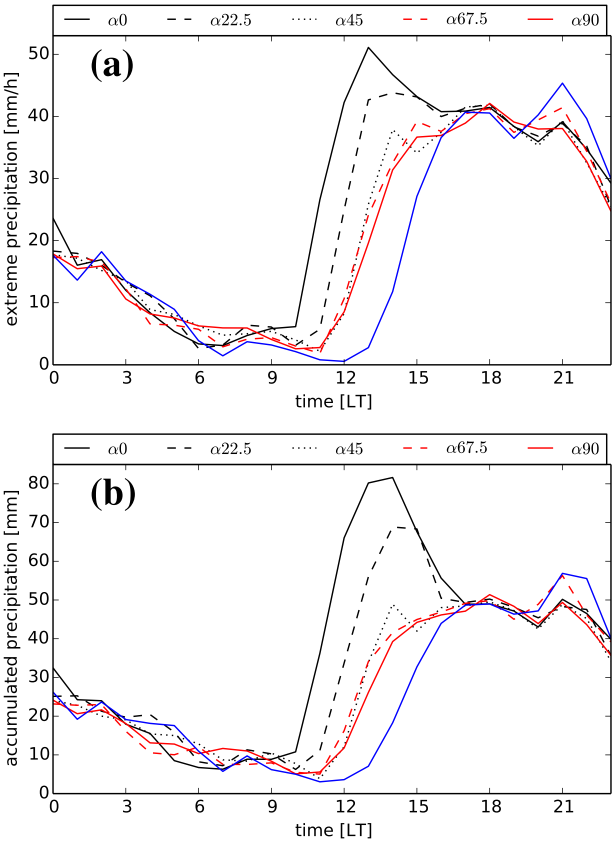

Figure B.4: (a) Diurnal cycle of 99.99th percentile (Q99.99) of hourly precipitation over 20 days and the whole domain. (b) Mean diurnal cycle of accumulated precipitation over the precipitation events on the grid points with precipitation>Q99.99 at that specific diurnal time. The blue lines belong to the FLAT simulation.

B.4 Summary

The effect of the mountain geometry on the development of clouds and precipitation was investigated. It was found that the wind direction relative to the mountain long axis is very important when the mountain does not have a circular shape. The mean and intense precipitation are both higher when the wind flows along the mountain orientation and are lower for the across-flow. Convective cells travel shorter for the along-flow (where the main cold-pool passes the mountain peak towards upstream) and the opposite occurs for the across-flow (where the main cold-pool cannot cross the peak). The other cases in between experience the transition trend from along- to across-flow. In comparison with no-mountain simulation, an earlier onset is seen for the extreme precipitation and an increase, for maximum diurnal extreme precipitation, for FLAT.

It should be noted that the results presented here are very preliminary. A more precise investigation is needed to understand the mountain-cold-pool interaction in convective cells triggering and their evolution. Moreover, the constrains in the cell-track-algorithm either in detecting the cells or defining the right location and time to trace the cells should be revised according to more literature reviews.

Bibliography

Addis, R. P., M. Garstang, and G. D. Emmitt, 1984: Downdrafts from tropical oceanic cumuli. *Boundary-layer Meteo.*, **28**, 23–49.

Amber, U., S. Wang, and A. Sobel, 2014: Response of atmospheric convection to vertical wind shear: cloud-system-resolving simulations with parameterized large-scale circulation. part I: specified radiative cooling. *J. Atmos. Sci.*, **71**, 2976–2993.

Arakawa, A., 2004: The cumulus parameterization problem: past, present, and future. *J. Climate*, **17**, 2493–2525.

Arakawa, A. and W. H. Schubert, 1974: Interaction of a cumulus cloud ensemble with the large-scale environment, Part I. *J. Atmos. Sci.*, **31**, 674–701.

Baldauf, M., A. Seifert, J. Förstner, D. Majewski, M. Raschendorfer, and T. Reinhardt, 2011: Operational convective-scale mumerical weather prediction with the COSMO model: description and sensitivities. *Mon. Wea. Rev.*, **139**, 3887–3905.

Ban, N., J. Schmidli, and C. Schär, 2014: Evaluation of the convection-resolving regional climate modeling approach in decade-long simulations. *J. Geophys. Res.-Atmos.*, **119**, doi:10.1002/2014JD021478.

Banta, R. M., 1984: Daytime boundary-layer evolution over mountainous terrain. Part 1: Observations of the dry circulations. *Mon. Wea. Rev.*, **112**, 340–356.

Banta, R. M., 1986: Daytime boundary-layer evolution over mountainous terrain. Part 2: Numerical studies of upslope flow duration. *Mon. Wea. Rev.*, **114**, 1112–1130.

Banta, R. M., 1990: The role of mountain flows in making clouds. *Atmospheric processes over complex terrain*, Meteor. Monogr., Vol. 23, 229–283.

Bao, X. H. and F. Q. Zhang, 2013: Impacts of the mountain-plains solenoid and cold pool dynamics on the diurnal variation of warm-season precipitation over northern china. *Atmos. Chem. Phys.*, **13 (14)**, 6965–6982.

Barthlott, C. and N. Kalthoff, 2011: A numerical sensitivity study on the impact of soil moisture on convection-related parameters and convective precipitation over complex Terrain. *J. Atmos. Sci.*, **68**, 2971–2987.

Barthlott, C. and D. J. Kirshbaum, 2013: Sensitivity of deep convection to terrain forcing over Mediterranean islands. *Quart. J. Roy. Meteor. Soc.*, **139**, 1762–1779.

Barthlott, C., et al., 2011: Initiation of deep convection at marginal instability in an ensemble of mesoscale models: a case-study from COPS. *Quart. J. Roy. Meteor. Soc.*, **137**, 118–136.

Bauer, M. H., G. J. Mayr, I. Vergeiner, and H. Pichler, 2000: Strongly nonlinear flow over and around a three-dimensional mountain as a function of the horizontal aspect ratio. *J. Atmos. Sci.*, **57 (24)**, 3971–3991.

Bennett, L. J., et al., 2011: Initiation of convection over the Black Forest mountains during COPS IOP15a. *Quart. J. Roy. Meteor. Soc.*, **137**, 176–189.

Bertram, I. and G. Mayr, 2004: Lightning in the eastern Alps 1993-1999, Part I: thunderstorm tracks. *Natural Hazards and Earth System Sciences*, **4**, 501–511.

Betts, A. K., 1986: A new convective adjustment scheme. Part I: Observational and theoretical basis. *Q. J. R. Meteorol. Soc.*, **112**, 677–691.

Betts, A. K., 2000: Idealized model for equilibrium boundary layer over land. *J. Hydromet.*, **1**, 507–523.

Bott, A., 1989: A positive definite advection scheme obtained by nonlinear renormalization of the advective fluxes. *Mon. Wea. Rev.*, **117**, 1006–1016.

Bouët, M., 1972: *Climat et météorologie de la Suisse romande*. Payot, 171 pp.

Bougeault, P., R. A. Houze, R. Rotunno, and H. Volkert, 2003: MAP SOP special issue. *Quart. J. Roy. Meteor. Soc.*, **129**, 341–899.

Brockhaus, P., D. Lüthi, and C. Schär, 2008: Aspects of the diurnal cycle in a regional climate model. *Meteorol. Z.*, **17**, 433–443.

Browning, K. A., et al., 2007: The Convective Storm Initiation Project. *Bull. Amer. Meteor.*, **88**, 1939–1955.

Carbone, R. E. and J. D. Tuttle, 2008: Rainfall occurrence in the us warm season: The diurnal cycle. *J. Clim.*, **21**, 4132–4146.

Chien, F. C. and C. F. Mass, 1997: Interaction of a warm-season frontal system with the coastal mountains of the western United States. Part II. Evolution of a Puget Sound convergence zone. *Mon. Wea. Rev.*, **125**, 1730–1752.

Christensen, J. and O. Christensen, 2003: Climate modelling: Severe summertime flooding in europe. *Nature*, **421**, 805–806.

Cotton, W. R., G. Bryan, and S. van den Heever, 2011: *Storm and cloud dynamics*. Academic Press, 809 pp.

Crook, N. A. and D. F. Tucker, 2005: Flow over heated terrain. Part I: Linear theory and idealized numerical simulations. *Mon. Wea. Rev.*, **133**, 2552–2564.

Demko, J. C. and B. Geerts, 2010a: A numerical study of the evolving convective boundary layer and orographic circulation around the Santa Catalina mountains in Arizona. Part I: Circulation without deep convectin. *Mon. Wea. Rev.*, **138**, 1902–1922.

Demko, J. C. and B. Geerts, 2010b: A numerical study of the evolving convective boundary layer and orographic circulation around the Santa Catalina mountains in Arizona. Part II: Interaction with deep convection. *Mon. Wea. Rev.*, **138**, 3603–3622.

Doms, G. and J. Förstner, 2004: Development of a kilometer-scale NWP System: LMK. *COSMO Newsletter*, **4**, 159–167, URL `http://www.cosmo-model.org`.

Doswell, C. A., H. E. Brooks, and R. A. Maddox, 1996: Flash flood forecasting: An ingredients-based methodology. *Weather and Forecasting*, **11 (45)**, 560–581.

Durran, D. R., 1990: Mountain waves and downslope winds. *Atmospheric processes over complex terrain*, Meteor. Monogr., Vol. 23, 59–81.

Durran, D. R. and J. B. Klemp, 1982: On the effects of moisture on the brunt-väisälä frequency. *J. Atmos. Sci.*, **39 (10)**, 2152–2158.

Easterling, D., J. Evans, P. Groisman, T. Karl, K. Kunkel, and P. Ambenje, 2000: Observed variability and trends in extreme climate events: A brief review. *Bull. Amer. Meteorol. Soc.*, **81**, 417–425.

Egger, J., 1990: The role of mountain flows in making clouds. *Thermally forced flows*, Meteor. Monogr., Vol. 23, 43–58.

Eigenmann, R., et al., 2011: Surface energy balance and turbulence network during the Convective and Orographically-induced Precipitation Study (COPS). *Quart. J. Roy. Meteor. Soc.*, **137**, 57–69.

Emanuel, K. A., 1994: *Atmospheric convection*. Oxford University Press, 580 pp.

Förstner, J. and G. Doms, 2004: Runge-Kutta time integration and high-order spatial discretization of advection. A new dynamical core for the LMK. *COSMO Newsletter*, **4**, 168–176, URL `http://www.cosmo-model.org`.

Frei, C. and C. Schär, 1998: A precipitation climatology of the Alps from high-resolution rain-gauge observations. *Int. J. Climatol.*, **18**, 873–900.

Frich, P., L. Alexander, P. Della-Marta, B. Gleason, M. Haylock, A. Tank, and T. Peterson, 2002: Observed coherent changes in climatic extremes during the second half of the twentieth century. *Clim. Res.*, **19**, 193–212.

Fuhrer, O. and C. Schär, 2005: Embedded cellular convection in moist flow past topography. *J. Atmos. Sci.*, **62**, 2810–2828.

Galewsky, J., 2008: Orographic clouds in terrain-blocked flows: An idealized modeling study. *J. Atm. Sci.*, **65**, 3460–3478.

Hagen, M., J. van Baelen, and E. Richard, 2011: Influence of the wind profile on the initiation of convection in mountainous terrain. *Quart. J. Roy. Meteor. Soc.*, **137**, 224–235.

Hassanzadeh, H., J. Schmidli, W. Langhans, L. Schlemmer, and C. Schär, 2015: Impact of topography on diurnal cycle of summertime moist convection in idealized simulations. *Meteorol. Z.*, doi:10.112/metz/2015/0653.

Hauck, C., C. Barthlott, L. Krauss, and N. Kalthoff, 2011: Soil moisture variability and its influence on convective precipitation over complex terrain. *Quart. J. Roy. Meteor. Soc.*, **137**, 42–56.

Heise, E., M. Lange, B. Ritter, and R. Schrodin, 2003: Improvement and validation of the multi-layer soil model. *COSMO Newsletter*, **3**, 198–203, URL `http://www.cosmo-model.org`.

Heus, T. and A. Seifert, 2013: Automated tracking of shallow cumulus clouds in large domain, long duration large eddy simulations. *Geosci. Model Dev.*, **6**, 1261–1273.

Hohenegger, C., P. Brockhaus, C. S. Bretherton, and C. Schär, 2009: The soil moisture-precipitation feedback in simulations with explicit and parameterized convection. *J. Climate*, **22 (11)**, 5003–5020.

Hohenegger, C., P. Brockhaus, and C. Schär, 2008: Towards climate simulations at cloud-resolving scales. *Meteorol. Z.*, **17 (4)**, 383–394.

Houze, R. A., 2012: Orographic effects on precipitating clouds. *Rev. Geophys.*, **50**, RG1001.

Khairoutdinov, M. F., S. K. Krueger, C.-H. Moeng, P. A. Bogenschutz, and D. A. Randall, 2009: Large-eddy simulation of maritime deep tropical convection. *J. Adv. Model. Earth Syst.*, **1**, doi:10.3894/JAMES.2009.1.15.

Kirshbaum, D. J. and D. R. Durran, 2004: Factors governing cellular convection in orographic precipitation. *J. Atmos. Sci.*, **61**, 682–698.

Kirshbaum, D. J. and R. B. Smith, 2008: Temperature and moist-stability effects on midlatitude orographic precipitation. *Quart. J. Roy. Meteor. Soc.*, **134 (33)**, 1183–1199.

Klemp, J. B. and R. B. Wilhelmson, 1978: Simulations of right-moving and left-moving storms produced through storm splitting. *J. Atmos. Sci.*, **35**, 1097–1110.

Kottmeier, C., et al., 2008: Mechanisms initiating deep convection over complex terrain during COPS. *Meteorol. Z.*, **17 (6)**, 931–948.

Levizzani, V., F. Pinelli, M. Pasqui, S. Melani, A. G. Laing, and R. E. Carbone, 2010: A 10-year climatology of warm-season cloud patterns over europe and the mediterranean from meteosat ir observations. *Atmospheric Research*, **97**, 555–576.

Lin, Y. L., R. L. Deal, and M. S. Kulie, 1998: Mechanisms of cell regeneration, development, and propagation within a two-dimensional multicell storm. *J. Atmos. Sci.*, **55**, 1867–1886.

Lin, Y. L. and L. E. Joyce, 2001: A further study of the mechanisms of cell regeneration, development, and propagation within a two-dimensional multicell storm. *J. Atmos. Sci.*, **58**, 2957–2988.

Manabe, S. and R. Stricker, 1964: Thermal equilibrium of the atmosphere with a convective adjustment. *J. Atm. Sci.*, **21**, 361–385.

Mass, C. F., 1981: Topographically forced convergence in western Washington state. *Mon. Wea. Rev.*, **109**, 1335–1347.

Mayr, G. J. and L. Armi, 2010: The influence of downstream diurnal heating on the descent of flow across the Sierras. *J. Appl. Meteor. Climatol.*, **49 (10)**, 1906–1912.

Miglietta, M. M. and A. Buzzi, 2001: A numerical study of moist stratified flows over isolated topography. *Tellus Ser. A-Dyn. Met. Oce.*, **53**, 481–499.

Miglietta, M. M. and A. Buzzi, 2004: A numerical study of moist stratified flow regimes over isolated topography. *Quart. J. Roy. Meteor. Soc.*, **130**, 1749–1770.

Miglietta, M. M. and R. Rotunno, 2005: Simulations of moist nearly neutral flow over a ridge. *J. Atmos. Sci.*, **62**, 1410–1427.

Miglietta, M. M. and R. Rotunno, 2006: Further results on moist nearly neutral flow over a ridge. *J. Atmos. Sci.*, **63**, 2881–2897.

Miglietta, M. M. and R. Rotunno, 2009: Numerical simulations of conditionally unstable flows over a mountain ridge. *J. Atmos. Sci.*, **66**, 1865–1885.

Miglietta, M. M. and R. Rotunno, 2010: Numerical simulations of low-CAPE flows over a mountain ridge. *J. Atmos. Sci.*, **67**, 2391–2401.

Miglietta, M. M. and R. Rotunno, 2014: Numerical simulations of sheared conditionally unstable flows over a mountain ridge. *J. Atmos. Sci.*, **71**, 1747–1762.

Mironov, D. and M. Raschendorfer, 2001: Evaluation of empirical parameters of the new LM surface-layer parameterization scheme. *COSMO technical report*.

Orlanski, I., 1975: A rational subdivision of scales for atmospheric processes. *Bull. Amer. Meteorol. Soc.*, **56**, 527–530.

Parker, D. J., 1996: Cold pools in shear. *Quart. J. Roy. Meteor. Soc.*, **112**, 1655–1674.

Peixoto, J. P. and A. H. Oort, 1996: The climatology of relative humidity in the atmosphere. *J. Climate*, **9**, 3443–3463.

Prudhomme, C. and D. Reed, 1998: Relationships between extreme daily precipitation and topography in a mountainous region: A case study in Scotland. *Int. J. Climatol.*, **18**, 1439–1453.

Queney, P., 1948: The problem of air flow over mountains: A summary of theoretical results. *Bull. Amer. Meteor. Soc.*, **29**, 16–26.

Raschendorfer, M., 2001: The new turbulence parameterization of LM. *COSMO Newsletter*, **1**, 90–98, URL `http://www.cosmo-model.org`.

Reinhardt, T. and A. Seifert, 2006: A three-category ice scheme for LMK. *COSMO Newsletter*, **6**, 115–120, URL `http://www.cosmo-model.org`.

Ritter, B. and J. F. Geleyn, 1992: A comprehensive radiation scheme for numerical weather prediction models with potential applications in climate simulations. *Mon. Wea. Rev.*, **120**, 303–325.

Roe, G. H., 2005: Orographic precipitation. *Annual Review of Earth and Planetary Sciences*, **33**, 645–671.

Rotunno, R. and J. Klemp, 1985: On the rotation and propagation of simulated supercell thunderstorms. *J. Atmos. Sci.*, **42**, 271–292.

Rotunno, R., J. B. Klemp, and M. L. Weisman, 1988: A theory for strong, long-lived squall lines. *J. Atmos. Sci.*, **45**, 463–485.

Schär, C., 2001: Mesoscale mountains and the synoptic-scale atmospheric dynamics: A review. *Meteorology at the Millennium: 150th Anniversary Conference of the Royal Meteorological Society*, Academic Press, Vol. 23, 29–42.

Schär, C. and D. R. Durran, 1997: Vortex formation and vortex shedding in continuously stratified flows past isolated topography. *J. Atmos. Sci.*, **54**, 534–554.

Schlemmer, L. and C. Hohenegger, 2014: The formation of wider and deeper clouds as a result of cold-pool dynamics. *J. Atmos. Sci.*, **71 (49)**, 2842–2858.

Schlemmer, L., C. Hohenegger, J. Schmidli, C. S. Bretherton, and C. Schär, 2011: An idealized cloud-resolving framework for the study of midlatitude diurnal convection over land. *J. Atmos. Sci.*, **68 (5)**, 1041–1057.

Schlemmer, L., C. Hohenegger, J. Schmidli, and C. Schär, 2012: Diurnal equilibrium convection and land surface-atmosphere interactions in an idealized cloud-resolving model. *Quart. J. Roy. Meteor. Soc.*, **138 (667, B)**, 1526–1539.

Schneidereit, M. and C. Schär, 2000: Idealised numerical experiments of Alpine flow regimes and southside precipitation events. *Meteorol. Atmos. Phys.*, **72**, 233–250.

Simpson, J., 1980: Downdrafts as linkages in dynamic cumulus seeding effects. *Amer. Meteor. Soc.*, **19**, 471–487.

Smith, R. B., 1979: The Influence of mountains on the atmosphere. *Adv. in Geophysics*, **21**, 87–230.

Smith, R. B. and I. Barstad, 2004: A linear theory of orographic precipitation. *J. Atmos. Sci.*, **61**, 1377–1391.

Smith, R. B. and S. Gronas, 1993: Stagnation points and bifurcation in 3-D mountain airflow. *Tellus Ser. A-Dyn. Met. Oce.*, **45**, 28–43.

Smith, R. B., et al., 2012: Orographic precipitation in the tropics: The Dominica Experiment. *Bull. Amer. Meteor. Soc.*, **93**, 1567–1579.

Soderholm, B., B. Ronalds, and D. J. Kirshbaum, 2014: The evolution of convective storms initiated by an isolated mountain ridge. *Mon. Wea. Rev.*, **142**, 1430–1451.

Stensrud, D. J., 2007: *Parameterization schemes: Keys to understanding numerical weather prediction models*. Cambridge University Press, 459 pp.

Steppeler, J., G. Doms, U. Schättler, H. W. Bitzer, A. Gassmann, U. Damrath, and G. Gregoric, 2003: Meso-gamma scale forecasts using the nonhydrostatic model LM. *Meteor. Atmos. Phys.*, **82**, 75–96.

Tiedtke, M., 1989: A comprehensive mass flux scheme for cumulus parameterization in large-scale models. *Mon. Wea. Rev.*, **117**, 1779–1800.

Tompkins, A. M., 2001: Organization of tropical convection in low vertical wind shears: The role of cold pools. *J. Atmos. Sci.*, **58 (59)**, 1650–1672.

Trenberth, K., A. Dai, R. Rasmussen, and D. Parsons, 2003: The changing character of precipitation. *Bull. Amer. Meteorol. Soc.*, **84**, 1205–1217.

Van Baelen, J., M. Reverdy, F. Tridon, L. Labbouz, G. Dick, M. Bender, and M. Hagen, 2011: On the relationship between water vapour field evolution and the life cycle of precipitation systems. *Quart. J. Roy. Meteor. Soc.*, **137**, 204–223.

Vergeiner, I. and E. Dreiseitl, 1987: Valley winds and slope winds - observations and elementary thoughts. *Meteorol. Atmos. Phys.*, **36**, 264–286.

Viviroli, D., H. H. Durr, B. Messerli, M. Meybeck, and R. Weingartner, 2007: Mountains of the world, water towers for humanity: Typology, mapping, and global significance. *Water Resour. Res.*, **43**, W07 447.

Wastl, C. and G. Zaengl, 2007: Analysis of the climatological precipitation gradient between the alpine foreland and the northern alps. *Meteorol. Z.*, **16**, 541–552.

Weaver, J. F. and S. P. Nelson, 1982: Multiscale aspects of thunderstorm gust fronts and their effects on subsequent storm development. *Mon. Weather Rev.*, **110**, 707–718.

Weckwerth, T. M. and D. B. Parsons, 2006: A review of convection initiation and motivation for IHOP_2002. *Mon. Wea. Rev.*, **134**, 5–22.

Wicker, L. J. and W. C. Skamarock, 2002: Time splitting methods for elastic models using forward time schemes. *Mon. Wea. Rev.*, **130**, 2088–2097.

Wilhelmson, R. and J. Klemp, 1978: A numerical study of storm splitting that leads to long-lived storms. *J. Atmos. Sci.*, **35**, 1974–1986.

Wulfmeyer, V., et al., 2011: Advances in the understanding of convective processes and precipitation over low-mountain regions through the Convective and Orographically-induced Precipitation Study (COPS). *Quart. J. Roy. Meteor. Soc.*, **137 (1)**, 1–2.

Young, G. S., S. M. Perugini, and C. W. Fairall, 1995: Convective wakes in the equatorial western Pacific during TOGA. *Mon. Wea. Rev.*, **123**, 110–123.

Acknowledgments

Now that I am standing at this point looking back, I see many people who supported me, helped me and encouraged me to continue the path which took me here.

First of all, I would like to thank my supervisor, Christoph, for giving me the opportunity to do my PhD in his group. He fully supported me in some occasions, which seemed completely dead-end. But, I survived by the wise steps he took to solve the problem. Second, I do thank Jürg as my co-supervisor, who gave me some good advises when I had to take turns in my project. He was also very quick in communicating with me in the last month of my PhD, that made the writing process of my thesis very smooth. Third, I am thankful to Georg, who accepted to be in my exam committee and gave me some nice comments to improve my thesis.

I also acknowledge Wolfgang for his insightful comments on my first paper. He was very supportive even from Berkley and even with the time zone difference, he had always time for skyping on any scientific issue. Sincere thanks go to Linda for being very patient during our long-distance scientific discussions from Hamburg. And, now that she is next door, I learn a lot from her in every chat we have. I also appreciate Steef's kind and helpful manner. His office door was always open for any question that I had. Anne and Dani are the people without whom I could never do any simulations. Not only that I got a full technical support from them, but also they were very efficient in knowledge transformation and connecting me with the right people who could be a help when I had a big issue with the computational infrastructure. I also like to thank all the L-floorians for spending those happy hours together.

During my stay in Switzerland, I had some awesome friends who made the life even more pleasant for me. I will never forget my ”In Hasht Nafar” friends, Iranian friends, Italian friends, and LTNT friends. Hanging out with these gals and guys with such diverse backgrounds provided me with almost whatever I needed to feel at home.

My dearest thanks go to my family. They always encouraged me to peruse my dreams and provided me with helpful advises and comport throughout my life. And, my special thanks go to Farhad who supported me and was with me during all the ups and downs, no matter what.

Curriculum Vitae

Hanieh Hassanzadeh
Institute for Atmospheric and Climate Science
ETH Zurich
Universitätstrasse 16
8092 Zurich, Switzerland
hanieh.hassanzadeh@alumni.ethz.ch
Born on 27 July, 1982 in Iran

Education

Jan 2015-present,	Post-Doc, Institute for Atmospheric and Climate Science ETHz university, Zurich, Switzerland
Dec 2010-Jan 2015,	PhD, Institute for Atmospheric and Climate Science ETHz university, Zurich, Switzerland
Sep 2004-Jan 2007,	Master of Science, Aerospace Engineering Department Sharif University of Technology, Tehran, Iran
Sep 2000-Sep 2004,	Bachelor of Science, Aerospace Engineering Department Amir Kabir University of Technology, Tehran, Iran

Award

Best oral presentation in the 32th International conference on Alpine meteorology, Slovenia, 2013.

Publications

- Hassanzadeh, H., J. Schmidli, W. Langhans, L. Schlemmer, C. Schär, 2015: Influence of the topography on the diurnal cycle of summertime moist convection, Meteorologische Zeitschrift, doi: 10.112/metz/2015/0653.

- Hassanzadeh, H., J. Schmidli, L. Schlemmer, C. Schär: Impact of topography on summertime extreme precipitation events in different environmental conditions, in preparation.

International conferences

- 16th Conference on American Mountain Meteorology, USA, 2014
- 32th International conference on Alpine meteorology (ICAM), Slovenia, 2013
- 7th CLM-Community Assembly, Belgium, 2012
- 10th Swiss Geoscience Meeting, Switzerland, 2012
- European Geoscience Union General Assembly 2012 (EGU2012), Austria, 2012